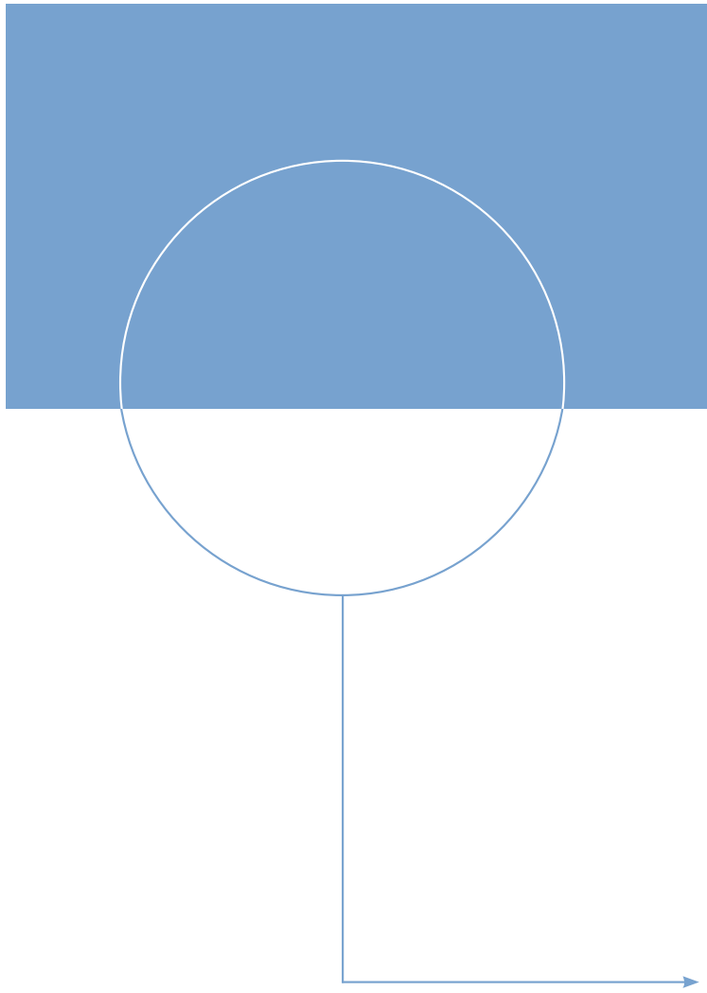

Master's thesis

2019

Anders Kjellevoll

NTNU
Norwegian University of
Science and Technology
Faculty of Information Technology and Electrical
Engineering
Department of Engineering Cybernetics

Anders Kjellevoll

Analysis and control of inductive power transfer systems for wireless battery charging in subsea applications

June 2019

NTNU
Norwegian University of
Science and Technology

NTNU
Norwegian University of
Science and Technology

NTNU

Norwegian University of
Science and Technology

Analysis and control of inductive power transfer systems for wireless battery charging in subsea applications

Anders Kjellevoll

Industrial Cybernetics
Submission date: June 2019
Supervisor: Jon Are Wold Suul
Co-supervisor: Giuseppe Guidi

Norwegian University of Science and Technology
Department of Engineering Cybernetics

Preface

This thesis concludes my two years Master's degree within Industrial Cybernetics at the Norwegian University of Science and Technology (NTNU) and represents the work that has been laid down in the course of the spring 2019.

The main objective of this work has been to evaluate the applicability, design and operation of inductive power transfer with respect to requirements and possible use for autonomous underwater vehicles (AUVs). The specialization project consisted of a literature search on the same subject, with focus on current practice offshore. Sensitive information related to the operation of a specific rig was therefore included, leading to the thesis being classified as confidential. This thesis will therefore not have any direct overlap with the preliminary project, although some parts will be based on the knowledge that was acquired.

Some of the work done in this project is based on the article on minimizing converter requirements of inductive power transfer systems [1], which was given as a base for the problem. However, the results presented in this thesis are acquired independently, where some meaningful discussions with my supervisor have lead me to obtain quite a comprehensive understanding of the systems dynamics. The work done consists mostly of theoretical analysis and simulations, where the model was created in *MATLABs* well known simulation-environment Simulink. This model has also been crucial to understand the different parameters affects on the system-response. Simulations that includes the effects of the separating medium on the power transfer could not be performed since tools for performing finite element method (FEM)-analysis has not been available. Some especially demanding calculations has been performed in Maple, and Visio has been an important tool for creating illustrations. The provided office space equipped with a powerful computer has also been a decisive factor for success.

I would like to thank my supervisor Jon Are Suul for an interesting project, and for providing great guidance throughout the semester. His inputs have been paramount, and the enthusiasm he shows for the field has been a great boost for my motivation. I would also like to thank Dr. Guiseppe Guidi for his guidance regarding equation-solving in Maple. In addition, I need to thank my fellow graduates for great discussions, inputs and moral boosters along the way.

Abstract

In many years, AUVs have primarily been used as tools for ocean-exploration. Today, they are in the development of becoming multi-purpose tools. This comes as a result of the progress that is seen within artificial intelligence, machine vision and big data. Multi-purpose AUVs can be used to more sophisticated purposes, as for instance tasks directly related to operation of subsea oil fields. Such tasks are today performed by remotely operated vehicles (ROVs) that are deployed on demand. Having permanently stationed AUVs on the seabed yields many benefits that leads to both increased safety and reduced costs. AUVs can also be completely tetherless with the advantage of them becoming more agile. The power will then be delivered from a battery. Retracting the AUV for charging is obviously time consuming and not practical, especially at the deepest subsea installations at ~3000 meters below sea level (mbsl). Wireless charging subsea can cope with this, and make AUVs more independent on surface-vessels in general. This will also enable AUVs intended for exploration and mapping to embark in longer and more extensive missions, which will result in an increased data-retrieval.

Wireless power transfer (WPT) is becoming a mature technology, and has seen a rapid development through consumer electronics, but also later; electric vehicles (EVs). Transferring power wirelessly subsea has also been proved to be feasible by many researchers, where resonant inductive power transfer (RIPT) is shown to be the most promising approach. The biggest problem with seawater as the separating medium is that it is more conductive than air, which leads to power loss due to eddy currents. This thesis presents a design of an inductive charger that suits the ratings of a multi-purpose AUV, while following design guidelines to reduce eddy current loss. The system is designed so that it operates at the bifurcation limit. The bifurcation-characteristics is then utilized to control the output-power for variable coupling coefficients (k). This is done by allowing off-resonant operation of the input voltage. Controlling the output power in such a manner ensures that the volt ampere (VA) requirements of the converters are minimized. This is in contrast to more conventional fixed frequency control, where operation at the resonance frequency is assured for all changes in coupling, while the amplitude of the voltage on the sending side will vary, thus demanding varying VA requirements to the converters.

The characteristics of the system is also affected by how the battery is modelled. A battery will appear as a constant voltage load (CVL), while it is often found that authors prefer viewing the battery as a constant resistance load (CRL) for simplicity. It is shown that the range

of couplings where the power output can be controlled by adjusting the systems operating frequency is theoretically bigger for a CVL than what a CRL-equivalent indicates. This range can also be extended by unbalancing the ratio between the supply-voltage and the output-voltage, and detuning the resonant part of the sending side, thereby having different resonance-frequencies on both sides of the circuit.

Based on the frequency characteristics of the system, a PI-controller has been implemented in Simulink that successfully controls the output power of the inductive charger for the maximum expected coupling and down to a minimum coupling k_{min} that is decided as part of the design. The controller faces no problems with stability or degraded performance when the coupling changes. As a result of the design, the efficiency of the proposed system has a constant efficiency of approximately 96,7 % over this range of couplings. Even though the losses in an implemented system would be larger due to eddy-current losses, thermal constants and non-ideal components, it is still expected that the efficiency will have small or slow changes when the coupling changes. This property can be utilized to control the variables on the receiving side based on the variables on the sending side, thus eliminating the need for a feedback that requires fast communication from the receiving side. However, based on the assumption that the efficiency will change slowly, a wireless feedback from the secondary side that adjusts the primary side reference will ensure that the power output remains nominal for a varying efficiency.

Sammendrag

I mange år har AUVer hovedsakelig blitt brukt som verktøy for å utforske havet. I dag er de i ferd med å utvikles til å bli flerbruks-verktøy. Dette kommer som et resultat av progresjonen som har skjedd innenfor kunstig intelligens, maskinsyn, og stordata. Flerbruks AUVer kan brukes til mer sofistikerte oppgaver, som for eksempel oppgaver som er direkte relatert til operasjonen av undervannsinstallasjoner. Slike oppgaver blir i dag utført av ROVer som blir sendt ut ved behov. Å ha permanente stasjonerte AUVer på sjøbunnen gir mange fordeler som igjen fører til økt sikkerhet og reduserte kostnader. AUVer kan også operere uten en tilkoblet kabel, noe som vil gjøre den mer agil. Effekten vil da istedenfor bli levert fra et batteri. Å hente opp igjen AUVen fra sjøen for lading er både tids-konsumerende og upraktisk, spesielt for de dypeste undervannsinstallasjonene lokalisert ~ 3000 meter under havet. Trådløs lading under vann kan få bukt med dette, og gjøre AUVer mer uavhengig av fartøy. Det vil også gjøre det mulig for AUVene å legge ut på lengre og mer omfattende oppdrag, som vil føre til en økt datainnhenting.

Trådløs oppladning har blitt en moden teknologi, og utvikling har skutt fart gjennom forbruker-elektronikk men også seinere; elektriske kjøretøy. Mange forskere har bevist at det er mulig å overføre effekt trådløst under vann, hvor resonant induktiv effekt overføring er blitt vist til å være den mest lovende fremgangsmetoden. Det største problemet med sjøvann som separerende medium er at det har høyere konduktivitet enn luft, som fører til høyere virvelstrømmer. Denne oppgaven presenterer et design av en induktiv lader som passer kriteriene til en flerburks AUV, samtidig som retningslinjene for å minimere virvelstrømmer er tatt hensyn til. Systemet er designet slik at det opererer på bifurkasjons-grensen. Bifurkasjons-karakteristikkene blir videre utnyttet for kontroll av effekten levert til batteriet for varierende magnetiske koblinger. Dette blir gjort ved å tillate operasjon utenfor resonans-frekvensen. Å kontrollere den leverte effekten på en slik måte gjør at volt ampere kravene til omformerne er minimert. Dette står i kontrast til mer konvensjonell kontroll, hvor systemet opererer på resonansfrekvensen for alle variasjoner i magnetisk kobling. Amplituden på spenningen vil da variere, som igjen krever varierende VA krav til omformerne avhengig av den magnetiske koblingen.

Karakteristikkene til systemet blir også påvirket av hvordan batteriet er modellert. Et batteri vil fremstå som en konstant spenningslast (CVL) in en elektrikst krets, men forskere foretrekker ofte å se på batteriet som en konstant resistiv last (CRL) for simplisitet. Det er vist at området av

koblinger hvor levert effekt kan bli kontrollert ved å justere frekvensen er teoretisk høyere for en CVL enn en CRL. Dette området kan også bli forlenget ved å ubalansere forholdet mellom inngangs- og utgangsspenning, og å detune den resonante delen av sende-siden. Dette gir en ulik resonans-frekvens på begge sider av kretsen.

Basert på frekvens-karakteristikkene til systemet, har en PI-kontroller blitt implementert i Simulink som suksessfullt kontrollerer utgangseffekten til den induktive laderen fra den maksimale forventede koblingen og helt ned til den minimale koblingen som blir bestemt som en del av designet. Kontrolleren møter ingen problemer hva gjelder stabilitet eller degradert ytelse når koblingen endres. Som et resultat av designet, er effektiviteten til det foreslåtte systemet ca. 96,7 % over hele det forventede koblingsspekteret. Selv om tapene i det implementerte system ville være høyere på grunn av virvelstrømmer, termiske konstanter, og ikke-ideelle komponenter, er det fremdeles forventet at effekten vil ha små eller treige endringer når koblingen endres. Denne egenskapen kan bli utnyttet for å designe en kontroller som utnytter sende-sidens variabler for å opprettholde den ønskede utgangseffekten. Dette vil forsikre at en tilbakekobling som er avhengig av rask kommunikasjon med den mottakende siden ikke er nødvendig. Basert på antagelsen om at effekten vil endre seg tregt, vil det være nødvendig med en trådløs tilbakekobling fra mottaker-siden som justerer sende-sidens referanse slik at effekten ut vil være nominell.

Contents

List of Figures

List of Tables

List of abbreviations

AC	alternating current
AUV	autonomous operated vehicle
CRL	constant resistance load
CVL	constant voltage load
DC	direct current
EV	electric vehicle
FEM	finite element method
FOM	figure of merit
HISC	hydrogen induced stress cracking
IGBT	insulated gate bipolar transistor
IoT	Internet of Things
IPT	inductive power transfer
LCT	loosely coupled transformer
LIB	lithium-ion battery
mbsl	meters below sea level
MOSFET	metal–oxide–semiconductor field-effect transistor
NRPT	non radiative power transfer
pf	power factor
PP	parallel-parallel
PS	parallel-series
PWM	pulse width modulation
RIPT	resonant inductive power transfer
RMS	root mean square
ROV	remotely operated Vehicle
RPT	radiative power transfer
SOC	state of charge
SP	series-parallel
SS	series-series
UUV	unmanned underwater vehicle
VA	volt Ampere
WPT	wireless power transfer
XT	Christmas three [1]
ZCS	zero current switching
ZPA	zero phase angle
ZVS	zero voltage switching

[1] Ventilation three that is amongst other things used to control the flow from the well.

List of symbols

k	Coupling coefficiency
λ	Flux linkage
ϕ	Flux
N	Number of turns in coil
$\mathcal{P}$	Permeance
μ	Permeability
A	Cross-sectional area of the coil
l	Length of the fluxpath
$\mathcal{R}$	Reluctance
L	Self inductance
M	Mutual inductance
C	Capacitance
X	Reactance
Z	Impedance
R	Resistance
S	Apparent power
P	Real power [2]
θ	Phase angle
ω	Angular frequency [3]
Q	Quality factor [4]
f	Frequency [5]
η	Efficiency
σ	Conductivity
x_u	Unbalancing factor
x_c	Detuning factor
ρ	Measurement inductor hollowness
d	diameter of inductor [6]
s	Spacing between the turns of the inductor
w	Width of the coils wire
e	Error
k_p	Proportional gain
k_I	Integral gain
n	Number of samplings

[2] P_0 implies nominal power, P_1 implies power in the sending side, P_2 implies power on the receiving side.
[3] ω_0 implies resonance angular frequency
[4] Will also be used as reactive power, but in a lesser extent.
[5] f_0 implies resonance frequency.
[6] d_{avg} indicates the average diameter, d_{in} indicates the inner diameter, d_{out} indicates the outer diameter.

Chapter 1

Introduction

1.1 Motivation

There is no doubt that wireless charging has come to stay. In recent years, an increased interest within the field has emerged through consumer electronics. After the first realization of a wireless charging smartphone in 2012 that complied with the Qi standards [2], the development within the field has been tremendous. Wireless power systems delivering a few kWs intended for EVs [3–5], to systems delivering MWs intended for ferries via. an air gap has been created successfully [6]. Wireless power transfer leads to higher durability because there is no cables that are exposed to wear. The usability and flexibility is higher since manual plugging will not be necessary and because wireless charging can be operated automatically, the reliability is also higher. These factors has lead to an increased interest from a business-perspective, and according to a market research done by MarketsandMarkets on wireless power transmission, the total revenue was valued at $2.50 billion USD in 2016 and is expected to reach $11.27 billion USD by 2022 [7].

Although this technology is becoming quite advanced through air, transferring power wirelessly subsea is still very much in the research portion of its development, and there is today not many practical systems that are actively used in business. Autonomous underwater vehicles (AUVs) are unmanned and software-controlled, and has traditionally been used for exploration and mapping of the environments in the sea. However, the battery-life of the AUV has severely affected its working range. The progressions done within machine learning, artificial intelligence and big data have enabled the AUVs to become more advanced, and prototypes that are meant to function as both observing and working tools are under development. Such AUVs are often called multi-purpose tools, and they are expected to be increasingly used at subsea layouts in the future. Since AUVs do not rely on high-speed data transmission such as the ROVs, they are more likely to be made tetherless. However, to prevent the time-consuming process of regularly retracting the AUVs for recharging, it is beneficial to introduce wireless charging subsea. The idea is to charge the AUVs in hubs near the layouts, enabling the AUVs to stay permanently underwater. This will in turn result in higher safety, reduced costs and lower emissions. Progression within wireless power transfer in the form of docking-stations

has been seen [8–11]. Most of the proposed dockings are however shaped to fit a specific type of AUV, so the use is very limited to one particular size. This is done to cope with the problems regarding the hydrodynamics in the sea that affects the magnetic coupling between the sending and receiving side of the charger. A more universal design is presented by Blue logic, that has in collaboration with Equinor and Eelume very recently started testing of an inductive charger in the fjords of Trondheim [12]. Considering that Equinor is the biggest operator on the Norwegian continental shape, it is very likely that wireless charging subsea will have a place in the future.

1.2 Background

The idea of transferring power wirelessly has been existent since the 1800s. André-Marie Ampere, Michael Faraday and Carl F. Gauss laid down a solid theoretical foundation that was later reworked by James C. Maxwell. He is today well known for a set of four equations that is called Maxwell's equations that describes how electric and magnetic fields propagate and interact [13]. Since then, the technological progress within the field has varied over the centuries with various success. The Tesla coils made by Nikola Tesla is one of these inventions, that unfortunately did not become a commercial success for WPT at least, because of its dependency on the surroundings [14]. A lot of work has also been done on radiative power transfer in the form of microwaves. Although this technology is perfectly suitable for transferring information, it poses some difficulties regarding power transfer. Omnidirectional radiation has a very low power transfer efficiency and is thereby limited to low power consuming sensors. This technology has therefore been advertised for powering Internet of Things (IoT) sensors [15]. Directional radiative power transfer requires an uninterrupted line of sight and relays therefore on sophisticate tracking mechanisms [16]. The biggest progress within WPT has however happened in the 21st century. Kurs et al. released an article in 2007 [16] where they were able to transfer 60 watts with $\sim$ 40 % efficiency over a distance in excess of two metes by utilizing a resonant inductive coupling. This showed the potential for non radiative power transfer as a method to enable power transfer over larger gaps. The commercialization of inductive power transfer happened shortly after, and as a result, wireless power consortium was founded i 2008 in order to set standards to ensure a safe and reliable WPT [2].

Resonant inductive power transfer has been proposed by multiple articles to be the most suitable topology for wireless power transfer in seawater [8–11]. The technology of resonant coupling was first introduced by Kurs et al. [16], and builds on the principle that two coils tuned in on the same resonance-frequency will have a stronger magnetic coupling than normal inductive charging. A popular analogy of resonance is to imagine a child pumping his legs at the right frequency in order to create momentum. In the world of inductive charging, resonance means adding a capacitor that cancels the reactance of the coil at the resonance-frequency.

How this capacitor is placed with respect to the coil will affect the characteristics of the system. The effects of the most basic compensation-topologies, i.e., series-series (SS), series-parallel(SP), parallel-series (PS), parallel-parallel (PP) is well documented in literature. More advanced compensating topologies has later been introduced, where multiple capacitors/coils is used. Such design will however increase costs, complexity and size of the total system, and is hence often limited to special cases and therefore also less investigated in literature. The SS-topology is found to be best suited for variations in the coupling coefficient since the resonant-frequency is not affected [17]. Because of the rough dynamics that an AUV may face during charging, it is more likely that the coupling coefficient will vary compared to for instance stationary inductive charging of an EV for a fixed length between the sending and receiving side of the system. Since the AUV are likely to face a time-varying magnetic coupling, off-resonant frequency control is recommended to keep the nominal output-power without having to increase the ratings of the converters [1, 18, 19]. This is in favor to a type of control where the power flow is maintained by adjusting the input voltage to ensure resonant operation at all coupling coefficients. This type of control is called fixed-frequency control and if the change in coupling is large enough, the converters need a higher VA rating for the same power transfer [20–22]. The frequency-response and the dynamics are also affected by how the load is modelled. The major part of literature tends to model the battery as an equivalent constant resistance load based on the nominal output voltage and power. However, it is more accurate to model the battery as a constant voltage load [1, 23, 24]. The biggest difference between power transfer in air and seawater is the losses due to eddy-currents. This problem can however be minimized by avoiding high resonance frequencies [11, 25, 26]. Many articles proves the feasibility of RIPT in seawater. The most similar system in terms of power-ratings as the one presented in this thesis is the design presented by Cheng et al. that was able to transfer 10 kW with 91% maximal transmission efficiency and over a 25mm gap [25].

1.3 Problem description

Wireless inductive power transfer across a non-negligible air gap is becoming an established technology for wireless battery charging in a wide range of applications. The main objective of this thesis is to evaluate the application of loosely coupled inductive power transfer (IPT) systems for subsea battery charging of autonomous underwater vehicles. Thus, an assessment of a potential application scenario for AUVs should be conducted and the benefits and challenges of utilizing IPT technology for subsea battery charging, including the challenges associated with the presence of saltwater as the separating medium between the sending and receiving coils, should be identified and discussed. The specific characteristics of a simple RIPT system configuration with a series-series-compensated topology and an uncontrolled diode rectifier as interface with the battery should be studied in detail, and a generic design suitable for AUV

applications should be identified. Especially, the differences in frequency-characteristics of an IPT system interfaced directly to a battery, appearing as a constant voltage load in the system, compared to a system with a constant resistive load should be identified and evaluated by theoretical analysis supported by time-domain simulations. A design approach for utilizing off-resonant operation for enabling constant power transfer over a wide range of coupling conditions without requiring over-rating of the passive components and the power electronic converters in the system should be assumed and investigated for the application. On the basis of this design approach, a simple control-system for maintaining the desired output power in response to variations in the distance between the sending and receiving side should be designed and evaluated.

1.4 Contributions

The contributions of this thesis can be summarized as:

- An actualization of wireless power transfer for subsea-applications based on current practice where related benefits and challenges are addressed (Chpt. 2, Sec. 3.4).
- A thorough analysis of the magnetic principles that enables wireless power transfer through inductive coupling has been performed (Chpt.3).
- A theoretical approach on how to model a RIPT-system with an inverter and an uncontrolled rectifier is presented. A power loss analysis of the resulting circuit is conducted, leading to the equations of the total efficiency of the system (Sec. 4-4.3).
- An approach on how to design a system that outputs the nominal power and voltage over the battery while operating at the bifurcation-limit for a defined minimum magnetic coupling both in case of a CVL and a CRL is shown. This design-approach enables the system to be controlled so that the output power remains nominal with varying distance between the sending and receiving side without setting additional requirements to the converters (Sec. 4.5-4.7).
- A working simulation-model of RIPT is implemented in Simulink. This model has been verified with theoretical analysis for both a CRL and a CVL, both with and without ideal coils (Sec. 4.5-4.7).
- An investigation of the difference between modelling the load as a CRL and a CVL is conducted. The main focus is the systems frequency response for variations in the coupling coefficient (Sec. 4.8).
- A control-system is implemented in the Simulink-model in order to show the feasibility of a simple control-system that maintains the nominal outputs when the distance between the sending and receiving side varies. The controller adjusts the frequency of the input AC-wave, leading to off-resonant operation that does not set any additional requirements

to the converters for a system that is designed as proposed (Chpt. 5).
- A suggestion on how to control the receiving side based on the sending side variables is presented, thus coping with the limitations related to fast wireless data-communication subsea.
- The key-findings from this thesis is planned to be written as a contribution to a conference during the course of the summer 2019.

1.5 Outline

The outline of the thesis after this introductory chapter is as follows:

- Chapter 2 presents some background on the use of AUVs today, and some predictions for their future based on the advancements within the field. In addition, typical power consumptions of some well known state of the art AUVs in investigated, leading to the requirements of the system that is to be designed in chpt.4.
- Chapter 3 is meant to provide a short introduction to WPT, before going into the details of some important properties related to RIPT. The benefits and challenges related to RIPT in seawater is addressed with this in mind. Solutions to these challenges are addressed, leading to some additional requirements to the system to be designed in chpt.4
- In chapter 4 the modelling of a RIPT-system that is SS-compensated is presented. The design is generic so that the results are comparable, and can be used to design systems with similar characteristics independent of the separating medium. The parameters of the system however, is set to suit AUVs with seawater as the separating medium as given by the study done in chpt. 2 and 3.
- In chapter 5, a control system is implemented and tested for different changes in coupling that an AUV might face during charging.
- Chapter 6 draws conclusions and presents suggestions for further work.

Chapter 2

Autonomous underwater vehicles

Autonomous underwater vehicles are smart unmanned underwater vehicles (UUVs) that are able to steer themselves and make decisions based on data-processing or pre-programmed paths. Quite generalized; all unmanned underwater vehicles that is not remotely operated falls under this category. Remotely operated vehicles are a separate category because they are remotely operated by sending real-time footage from cameras that are mounted on the ROV to the operators. They come in many shapes and sizes, but common for them all is that they are dependant on a theater in order to enable video-communication with the operator. This theater is also often used to supply power and if necessary hydraulics to the ROV. Wireless charging is therefore not that relevant for ROVs. They are however important to mention because they are by far the most commonly used UUV to this date, especially as a working tool. A vision for the future is that AUVs should to a bigger extent be able to replace ROVs as a working tool. Figure 2.1 presents an overview of how UUVs are used today, and predictions for the future. This figure is made with inspiration from [27], and is a reworked version from a figure made for the project thesis [28].

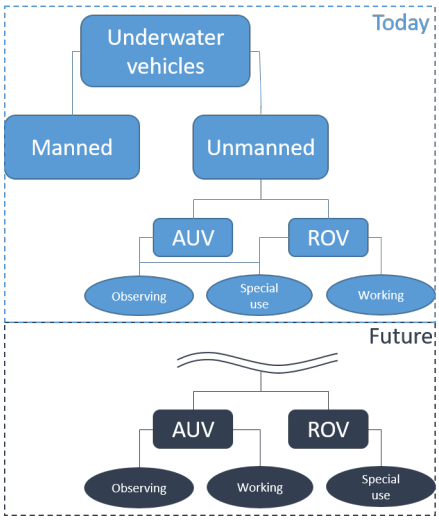

Figure 2.1: How UUVs is used today, and predictions for the future.

2.1 The use of AUVs

In decades, AUVs have mostly been used as a tool for exploring and mapping the ocean. The technology within this use of AUVs has also become more sophisticated with the years. Better sensors, high power density batteries and advanced software has resulted in an increased ability to obtain important information about marine environments. According to the national ocean service, more than **eighty percent** of the ocean was in 2018 unmapped, unobserved and unexplored [29]. There is no doubt that this percent would be higher if it was not for these AUVs. Kongsberg maritime are well known for their AUVs Hugin (fig. 2.2a) and Munin that can operate at water depths of up to 6000 meters mbsl and provide high resolution images of the seabed, while extracting geophysical information. These types of AUVs are normally shaped as torpedoes to better withstand hydrodynamic drag. This shape ensures minimal power consumption when moving, and they can therefore operate independent on human interaction for multiple days [30]. However, when they are about to run out of power, they ascend to the surface, and is retracted to a surface vessel for charging and exchange of data. To minimize this dependancy, gliders can be used. Underwater gliders utilize the high density in water, and by changing its density it transforms vertical energy into horizontal energy by descending and ascending in the water. These AUVs will move much slower, but has the advantage that they are much less power consuming, enabling them to stay subsea and collect data for months at time [31]. For an extended period of operation, a solution where the glider is connected to a floating solar panel through a tether can be used. The floater is also equipped with a GPS unit and Iridium communications system, to exchange data from the glider wirelessly [32] over far distances to be independent of surface vessels. Still, the major part of AUVs will need to ascend to the surface for data extraction and charging.

In the past years, a lot has happened within artificial intelligence, machine learning and big data processing. In addition, because of IoT, less power-consuming advanced hardware are more accessible. This development paves the way for more advanced AUVs. Perhaps the most exiting ongoing project is the snake-robot Eelume. This AUV is meant to be used as both an observing and working tool, and is therefore often referred to as a multi-purpose tool. With its agile shape, it can reach places that are inaccessible for the more common cube-formed ROVs. In addition, it can form its shape around pipelines, so that a thorough scan of wear can be performed regularly (fig. 2.2b). Eelume is meant to be able to operate valves on the subsea ventilation three, commonly refereed to as christmas trees (XTs) and to clean installed equipment. It can be used as both an ROV and an AUV, where the latter one is independent on a tether. Since this AUV is supposed to be highly maneuverable, it needs more thrusters than the observing AUVs. In addition, it needs to be able to deliver enough force to turn valves on XTs, therefore, this AUV will be more power-consuming. As a result, a tether-less Eelume would need to be taken out of water regularly for charging and data-extraction, which is not practical

in the long run. This is where wireless charging of AUVs on the seabed becomes relevant. The largest operators on the Norwegian continental shelf; Equinor, is in cooperation with Blue Logic and Eelume currently testing a rig (fig. 2.2d) made for inductive charging of AUVs in the fjords of Trondheim [12]. Equinor predicts this technology to replace the traditional ways of operating an oil field, and it is highly relevant where there are subsea layouts. The idea is to have hubs on the seabed that will serve as a home for the AUVs. This hub will have a permanently connected tether from a rig or to shore, through which data and power is transmitted. This allows for these AUVs to stay permanently underwater and thereby perform maintenance tasks regularly, while also being available to perform tasks directly related to operation. If such charging-hubs are placed around on the seabed, the observing AUVs such as the Hugin could also utilize it in order to recharge and empty data, enabling them to be more independent of surface vessels. This would however require a more universal design of the charging-hubs than what is often referred to in literature [8–11], where the docking is formed to fit the AUV that the use is intended for (fig. 2.2c). This design will however make the charging less exposed for misalignment because it is more protected from the hydrodynamics in the sea. The prototype docking-station that has been developed as a cooperation between Blue logic and Equinor as depicted in Figure 2.2c is a more universal design, since the induction-plate is flat, thereby fitting AUVs in different shapes. AruCo codes sits on the induction-plate enabling the AUV to navigate precisely and calibrate the camera.

(a)

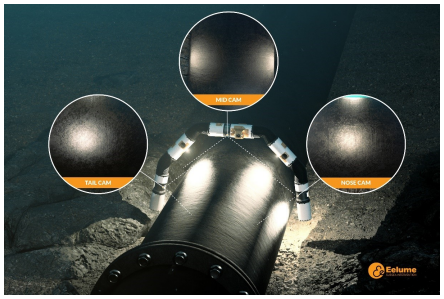

(b)

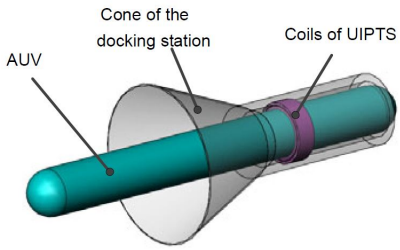

(c)

(d)

Figure 2.2: (a) Hugin in the stinger before being deployed from the vessel [33]. (b) Eelume uses its agile shape to perform a thorough scan of the pipeline on the seabed [34]. (c) Conventional docking-station presented in literature [10] (d) Wireless docking station made for the Eelume in cooperation between Equinor and Bluelogic [35].

2.1.1 Power consumption and battery characteristics of AUVs

Since AUVs are found in many forms and sizes, their demand for power will be varying. As a result, the size of the battery in the biggest working class AUVs might have hundred times the capacity of the ones in the smallest observer-class AUVs. Since the field of wireless power transfer subsea is relatively new, no official standards has yet been made. This is quite different from the development that is seen within wireless charging of electric vehicles (EVs), which is becoming quite standardized through standards like SAE J2954 [36]. This standardization is enabled because of the similar demands with regards to the application, power demands, size, purpose etc. It will therefore be necessary to specify which type of AUV the inductive power transfer is to be designed for.

The exploring AUVs, like the Hugin, are also found in various forms. Hugin 1000 is a smaller and less complex AUV than the state of the art Hugin Superior. These AUVs are respectively rated to operate 1000 and 6000 mbsl. From the datasheets it is found that Hugin 1000 has a capacity of 18 kWh[30] while Hugin superior has 62,5 kWh [37] in capacity. Their charge-time is respectively 8 hours and 5-8 hours, resulting in that their power-rate when charging is ranging from approx. 2-12 kW. In the article about Eelume [38] it is stated that the AUV has a maximum power consumption of 2 kW. Based on these cases, it is decided that the system that is to be designed should be designed to deliver approx. 10 kW. This is also not to far away from the power rates that are very often seen for EVs, i.e., 3.2, 7 and 11 kW. The reason for choosing a power rate of such size instead of Eelumes maximum power consumption is because today's trends shows that fast charging is in focus [39]. The main driver for this is that producers of EVs want to compete with cars that uses traditional fuel with regards to energy refill. This will lower the bar for use of EVs at long range trips, because one would not need to wait hours for the car to recharge in the middle of the trip. It is therefore natural to think that the development within this field will be taken advantage of when designing as system for WPT subsea. Fast charging demands high power, for this reason 10 kW is more suitable than 2 kW.

Another important part of the design is to decide the nominal voltage of the AUV. From the same datasheets it can be found that Hugin 1000s nominal voltage is around 40 V, while the Eelume has a nominal voltage of 300 V. The reason for this is that the Hugins are designed to be as low power-consuming AUVs as possible in order for it to track longer distances each dive. This means that the nominal voltage can be low because its functions does not demand high power. Eelume on the other hand is designed to be a working ROV, meaning that it should be able to shift valves on subsea valve trees among other things. This makes its power-consumption more unpredictable as it is decided for each individual task that is to be performed. The main focus of this thesis is the AUVs that are meant to operate on subsea fields. Based on this, the system that will be designed in this thesis will be designed for fast charging of working class AUVs. The focus will not solely be on optimal design, but also how

the different system parameters affects the system when changed. In order to do this, it is important to understand the characteristics of the batteries in a typical AUV.

Considering the high pressure ratings and the cold water that the AUV may face during operation, it is important with a battery that works well in such conditions. Bradley et al. [40] did a careful review of the different available battery systems in order to find the most suitable for use in AUVs. They concluded that Lithium-ion (Li-ion) batteries was most appropriate because of their long cycle life, and attractive energy density. Li-ion batteries (LIB) was first commercially available in 1991, and since then, they have grown to be the most dominant power storage solution for portable IT devices [41]. The four major components of the LIB are the cathode, anode, electrolyte and separator. Each separate cell voltage will on average output around 3.7 V. Design of batteries for higher voltage ratings is normally designed by connecting multiple cells in series to obtain the wanted voltage. Adjusting power is obtained by connecting cells in parallel. For high-voltage applications, LIBs are normally built in modules with a voltage-rating of approx. 30-40 V. Battery systems are then designed to the nominal power and voltage by series and parallel connecting these modules.

A lot of research has been done on different types of anode and cathode materials for best performance, but the most common material in the cathode is lithium cobalt oxide ($LiCoO_2$). In the anode there will normally be some form of carbon [41]. When the battery is completely discharged, Li atoms are only contained as part of the cathode. When the battery is charged, the Li atoms are released from the cathode, and migrate through the electrolyte into the anode. This creates an unstable state. The Li ions want to go back to its stable state, as part of the lithium cobalt oxide. Since the electrolyte is preventing the electrons from passing through, the electrons will pass through the external load as current, and thereby the battery is being discharged while delivering power to the load. The separator works as a safety mechanism in case of the liquid electrolyte being dried up because of too high temperatures. The nominal voltage of the battery will vary with the state of charge (SOC). This can be shown in the form om discharge-curves. These curves depends on the anode- and cathode material. Figure 2.3 (a) shows the discharge curve of a 3.7 nominal voltage Li-ion cell with a hard carbon anode. This curve shows that the cell voltage is approx 4.2 V (113.5 % from nominal) when fully charged, and 2.5 V (67 % from nominal) when discharged. Figure 2.3 (b) shows a typical charging process of a LIB. At the initial stage, the battery can be pre-charged at a low, constant current if the cell is not pre-charged before. Then, it is switched to charge the battery with constant current at a higher value. When the battery voltage (or SOC) reaches a certain threshold point, the charging is changed to constant voltage charge. Constant voltage charge can be used to maintain the battery voltage afterward if the direct current (DC) charging supply is still available [42].

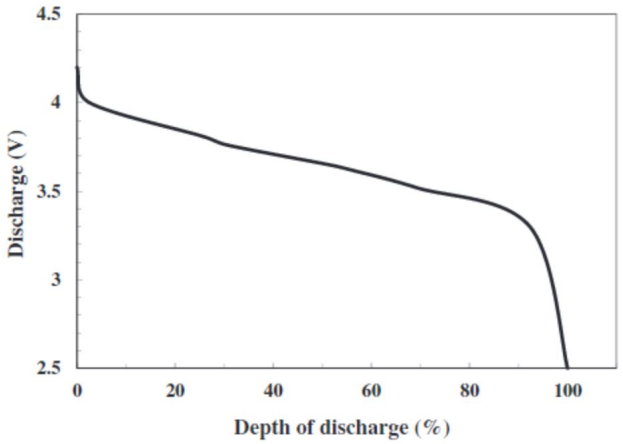

(a)

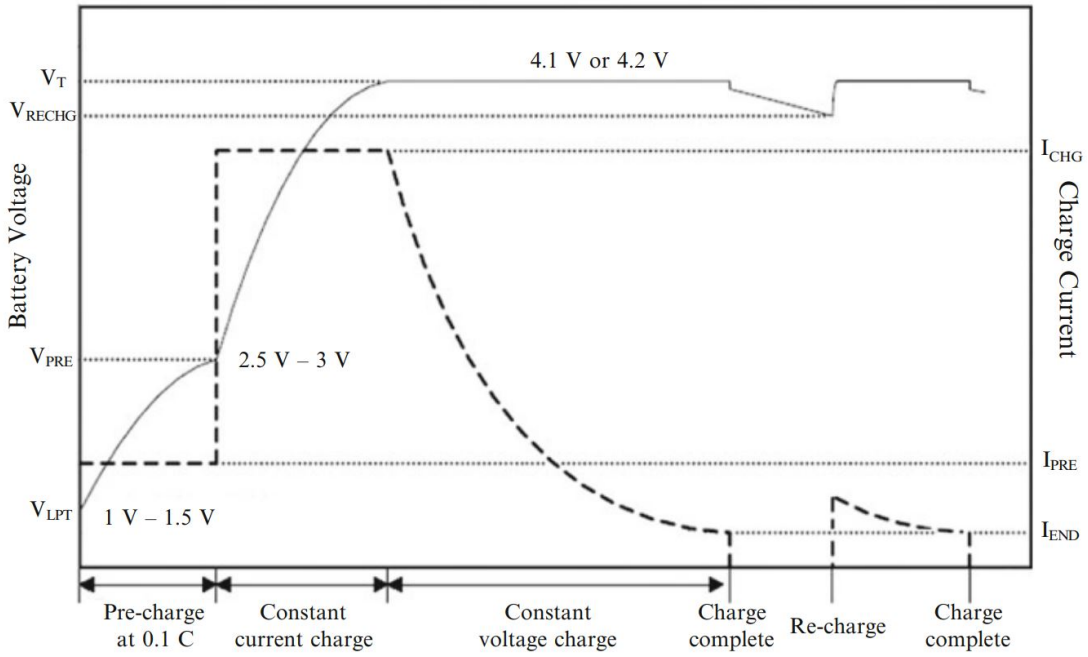

I_{CHG}: Charge current. 0.5C-1C can be considered as fast charge.
I_{PRE}: Pre-charge current, e.g. 0.1 C.
I_{END}: Ending charge current, e.g. 0.02 C.
V_T: Battery terminal voltage.
V_{RECHG}: Threshold voltage to start recharge.
V_{PRE}: Voltage when pre-charge finished.
V_{LPT}: Low protection threshold voltage.

(b)

Figure 2.3: (a) Discharge curve with hard carbon anode [41]. (b) Typical Li-ion cell charge profile [42].

Chapter 3

Inductive power transfer

This chapter aims to provide some short information about different ways to realize wireless power transfer, and to present some history. Further, theoretical background of some key-properties related to RIPT is presented. These properties are fundamental in order to understand the system that is to be designed in chapter 4. Lastly, the benefits and the challenges that comes with realizing RIPT with seawater as the separating medium are addressed.

3.1 Wireless power transfer in general - history and development

Wireless power transfer is the ability to transmit energy from a source to a load via. a gap without interconnecting cords. Its application ranges from low-power devices such as toothbrushes, to beaming power towards a solar-powered unmanned aircraft [43]. In recent years, wireless charging has increasingly been introduced to our daily life, mainly in the form of charging smart-phones and tablets, but also in later years; electric vehicles. Wireless charging ensures an increased flexibility, better usability and a higher durability [14]. It is normal that wireless power transfer is divided into radiative power transfer (RPT) and non-radiative power transfer (NRPT). Radiative power transfer is more dependant on the environment because it is based on radiation. RPT is usually meant for long-range applications, and is rarely seen in civil use as the intended applications are quite narrow. NRPT however is less dependant on the environment because of the characteristics of a magnetic field as described by Maxwells second law [13], that states that the divergence of a magnetic field is independent on the environment. In theory, it is dependant on magnetically charged particles, but this phenomena has not yet been proved to be existent. Table 3.1 provides an overview over the different ways to realize wireless power transfer [44].

Table 3.1: Overview of wireless transfer technologies [44].

WPT technologies		Strengths	Weaknesses	Example applications
Inductive Coupling		Simple, high power transfer efficiency in centimeter range	Short charging distance, requiring accurate alignment in charging direction	Electric toothbrush, charging pad for cell phones and laptops
EM radiation	Omnidirectional	Tiny receiver size	Rapid drop of power transfer efficiency over distance, ultra low-power reception	Charging a WSN for environmental monitoring (temperature, moisture, light, etc.)
	Unidirectional (microwave/ laser)	Effective power transmission over long distance (kilometer-range)	Requiring LOS and complicated tracking mechanisms, inherently large scale of devices	SHARP unmanned plane
Magnetic resonant coupling		High efficiency over several meters under omni-direction, not requiring LOS, and insensitive to weather conditions	High efficiency only within several-meter range	Charging mobile devices, electric vehicles, implantable devices and WSNs

Inductive coupling and magnetic resonant coupling builds on the same principle, and that is to exchange power between to coils by inducing a variable magnetic field in one coil that affects the nearby coil. The resonant inductive coupling was discovered later by Kurs et al. [16] where they were able to transfer 60 watts with ~ 40 % efficiency over a distance in excess of two metes. This discovery showed the great potential of RIPT as a way to realize mid-range power transfer by having two coils tuned into resonance. This discovery lead them to launch a start-up company called Witricity. This way of transferring power is the method that is done most research on in recent years, and it is foreseen as the most promising method for wireless power transfer. Commercial chargers is also to a big extent built on this principle. Therefore, the further focus in this thesis will be on resonant inductive power transfer. The history and development of WPT can be traced back to the 19th century, where equations that could describe the world of electromagnetism was found. It was Hans C. Ørsted that was first to discover the relationship between electricity and magnetism. André-Marie Ampere, Michael Faraday and Carl F. Gauss laid down a solid foundation of the mathematical relationships. Their work was further reworked by James C. Maxwell, who is well known for the Maxwell equations which is a set of four equations that together describes how electric and magnetic fields propagate and interact, and how they are influenced by objects[13]. Since then, the technological progress within the field has varied over the centuries. However, the main drivers for the progress can be split into three different periods [14]:

- Late 1800s - Curiosity because of the theoretical foundation.
- Mid 1900s - Military projects and medical research.
- Late 1900s to this date - Consumer electronics and IoT. Charging of electric vehicles.

The work done by the MIT physics team (Kurs et al.)[16] in 2007 were a real accelerator for the development within NRPT that previously had only been used for very short distances, often with strict criteria regarding alignment. Ever since, there has been an enormous development

withing this field, and as a result, wireless power consortium was founded in 2008 in order to set standards to ensure safe and reliable WPT [2].

3.2 Some important properties

3.2.1 Self- and mutual inductance

In this section, a careful review of the phenomena of inductance will be presented in order to understand how mutual inductance enables inductive power transfer. How the separating medium affect the coupling will also be presented. Intuitively, it is easy to assume that the magnetic coupling is worse in seawater than in air. However, it can be seen that the material-properties that affects the magnetic coupling between two coils is not that different for air and seawater. Under certain assumptions regarding the parameters of operation, the coupling coefficient can in fact be the same in air as in seawater as will be further investigated in chapter 5. The following derivation is done with inspiration from [45].

Self inductance - The idea of the coil as an alternating voltage-source can be traced back to Michael Faraday. He found that when current passed trough a coil, it created a flux linkage that was proportional to the turns of the coil. When the current changed, the flux linkage collapsed and induced a voltage in the circuit. This relationship can be denoted as Faraday's law;

$$V(t) = \frac{d\lambda}{dt}, \tag{3.1}$$

where λ represents the flux linkage. This flux leakage can be denoted as the the flux (ϕ) generated by the current passing through the coil times the number of turns (N) in the coil:

$$\lambda = N\phi. \tag{3.2}$$

Flux on the other hand is also dependant on the number of turns (N) in the coil. In addition, it is dependant of the current going through the coil and the coils permeance ($\mathcal{P}$):

$$\phi = \mathcal{P}Ni. \tag{3.3}$$

Permeance ($\mathcal{P}$) is a material property that describes the relationship between the permeability of the material (μ), the cross-sectional area (A) normal to the direction of the flux and the length of the fluxpath(l):

$$\mathcal{P} = \frac{\mu A}{l}. \tag{3.4}$$

Permeance is often rewritten as reluctance ($\mathcal{R}$) because they have an inverse relationship

given as

$$\mathcal{R} = \frac{1}{\mathcal{P}} = \frac{l}{\mu A}. \tag{3.5}$$

The reason for why reluctance is more used is because it can be seen as the resistance that the flux faces when traveling through different materials. An analogy for reluctance is the resistance that the current faces when traveling through circuits. It is for instance well known that flux travels much easier through iron than air. This is because of the difference in permeability where iron has 5000 times the permeability compared to air [46], and therefore lower reluctance. The difference between permeability, and hence reluctance of air and seawater is however very small as Table 3.2 shows, meaning that the magnetic coupling will not be much affected with seawater as the separating medium [25].

Table 3.2: Comparison of relevant properties of air, freshwater and seawater.

Medium	Relative permittivity	Conductivity (S/m)	Relative permeability
Air	1.006	0	1.000004
Freshwater	81	0.01	0.999991
Seawater	81	4	0.999991

By combining Equation 3.4, 3.3, 3.2 and 3.1 the formula for a coils self-inductance can be obtained as

$$V(t) = L\frac{di}{dt}, \quad L = N^2 \cdot \frac{\mu A}{l}. \tag{3.6}$$

Equation 3.6 is the formula for self-inductance in its most general form. In reality, coils can be found in many different shapes. As a result, there exists more accurate ways of calculating self-inductance for specific shapes. Frederick Grover did extensive work in order to publish a book in 1946 [47] containing formulas and tables making it easy to calculate the self-inductance of virtually every type of inductor. This book is highly recognized within its field, and later publications tend to refer to the methods presented in this workbook when finding alternate ways of calculating self-inductance [48].

In literature related to inductive wireless power transfer some prefer to analyze the circuit in terms of leakage inductance. This terms should not be confused with self inductance as self inductance is constant while the leakage inductance will vary with the link between the coils. In Figure 3.1 the result of the leakage inductance can be found in the form of a leakage flux denoted ϕ_{11}. It is clear that the voltage induced by this leakage-inductance will not affect the receiving coil. Because of this, some authors prefer to analyze the circuits using for instance

the T-model or cantilever-model where they separate the sending and receiving coils into three coils where one coil represents the coupling, while the two others represent their individual leakage inductance [49]. The inductance of the equivalent coil that links the primary and secondary coil is called mutual inductance.

Mutual inductance and coupling coefficient - Mutual inductance is tightly related to self-inductance, and is a measurement of how much the flux created by one coil, affects a nearby coil. The whole idea of inductive power transfer builds on this phenomena. It has been shown that flux is generated when current is passing trough a coil. It has also been shown that flux travels through materials, preferably with a high permeability. Figure 3.1 aims to show how this linkage takes form. In this figure, the flux travels through an unknown material, but in case of an inductive charging subsea, it would be seawater. The flux will then generate a current in the secondary coil, thus creating a voltage potential V_2.

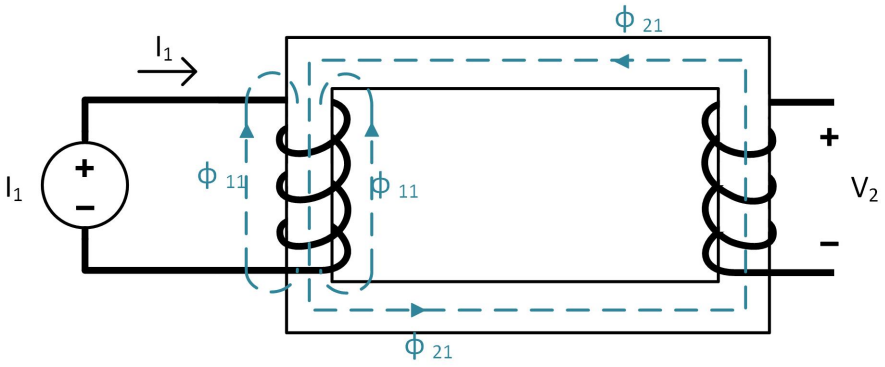

Figure 3.1: Two magnetically coupled coils through a material.

The total flux linkage for coil number one is the sum of ϕ_{11} and ϕ_{21}:

$$\phi_1 = \phi_{11} + \phi_{21}. \tag{3.7}$$

Where these fluxes are coupled to the current i_1 as follows

$$\phi_1 = \mathcal{P}_1 N_1 i_1, \tag{3.8}$$

$$\phi_{11} = \mathcal{P}_{11} N_1 i_1, \tag{3.9}$$

$$\phi_{21} = \mathcal{P}_{21} N_1 i_1. \tag{3.10}$$

Where $\mathcal{P}_{11}$ is the space occupied by the flux ϕ_{11} and $\mathcal{P}_{21}$ is the space occupied by the flux ϕ_{21}, i.e., the conducting medium. The total permeance $\mathcal{P}_1$ is the the sum of these. To derive the expressions for V_1 and V_2 Faradays law (eq. 3.1) can be used,

$$V_1 = \frac{d\lambda_1}{dt} = \frac{d(N_1\phi_1)}{dt} = N_1\frac{d}{dt}(\phi_{11} + \phi_{21})$$
$$= N_1^2(\mathcal{P}_{11} + \mathcal{P}_{21})\frac{di_1}{dt} = N_1^2\mathcal{P}_1\frac{di_1}{dt} = L_1\frac{di_1}{dt}, \tag{3.11}$$

and V_2 is thus,

$$V_2 = \frac{d\lambda_2}{dt} = \frac{d(N_2\phi_{21})}{dt} = N_2\frac{d}{dt}(\mathcal{P}_{21}N_1i_1)$$
$$= N_2N_1\mathcal{P}_{21}\frac{di_1}{dt}. \tag{3.12}$$

From this equation, the mutual inductance (M) from the primary coil to the secondary coil can be defined as,

$$M_{21} = N_2N_1\mathcal{P}_{21}. \tag{3.13}$$

And thereby, the total magnetic relationship from coil number one to coil number two with two equations can be defined as:

$$V_1 = L_1\frac{di_1}{dt}, \quad \text{and} \quad V_2 = M_{21}\frac{di_1}{dt}. \tag{3.14}$$

The same procedure yields if the current-source is placed on the right side of the conducting material in Figure 3.1, then the total relationship can be written as

$$V_2 = L_2\frac{di_2}{dt}, \quad \text{and} \quad V_1 = M_{12}\frac{di_2}{dt}. \tag{3.15}$$

In addition it is found that [45]:

$$M_{12} = M_{21} = M. \tag{3.16}$$

This means that for a system that will charge a battery V_2 with a power-source V_1, the mutual inductance link of such a system can be written as

$$\begin{aligned} V_1 &= L_1 \frac{di_1}{dt} + M \frac{di_2}{dt}, \\ V_2 &= L_2 \frac{di_2}{dt} + M \frac{di_1}{dt}. \end{aligned} \tag{3.17}$$

Which is an important set of equations that will be used later. It is very common to view the size of the mutual inductance in terms of the coupling coefficient. The neat property of the coupling coefficient is that it gives a fast and comprehensive indication of how well the coupling between the two coils are. The formula for the coupling coefficient is:

$$k = \frac{M}{\sqrt{L_1 L_2}}. \tag{3.18}$$

The value of k will always be in the range,

$$0 \leq k \leq 1. \tag{3.19}$$

A value of k=0 implies that the two coils have no common flux, i.e., $\phi_{12} = \phi_{21} = 0$. The mutual inductance will then similarly be M=0. When the coefficient of coupling is k=1, $\phi_{11} = \phi_{22} = 0$. Thus, all the flux that links coil one also links coil two. In reality, obtaining a k=1 is physically impossible [45]. However, magnetic materials (such as alloys of iron, cobalt and nickel) creates a space with high permeance and are used to establish a coefficient of coupling that approach unity. Similar to the case for calculation of a coils self-inductance, the general formula for the mutual inductance M as given by Equation 3.12 is not precise enough in many cases. For this reason, some articles tend to perform heavy calculations for their specific cases, like the mutual inductance between two tightly wound thin circular coils that is co-axial located to each other [50] by using the Grover's formula [47]. Some articles uses Neumanns's formula instead [51]. While others recommend the later work done by Babic et al [48] where the Grover's formulas is reworked. Common for these methods is that they are quite advanced - e.g. involving elliptic integrals of first and second kind. Therefore, some articles find equivalent expressions for these elliptic integrals that works under some assumptions regarding the relationship between the radii of the coils and their distance in between [52]. However, the most robust way of getting an accurate representation is as recommended in [10] by using FEM-software like the FEM software package ANSOFT Maxwell. Ideally, a FEM analysis on the magnetic coupling between the coils would be conducted in order to estimate how the coupling coefficient would be affected by a change in position for the design presented in this thesis with seawater as the separating medium. Due to restrictions regarding access

to software, this could not be done. In chapter 5, an approximate relationship between the coupling coefficiency and the distance between the coils for the designed system in chapter 4 will however be presented by utilizing simplifications presented in literature.

3.2.2 Resonance

When inductors and capacitors are introduced to a circuit, a resulting reactance will also appear. The formula for an inductor and a capacitor is respectively

$$V_L(t) = L\frac{di}{dt}, \quad \text{and} \quad i_c(t) = C\frac{dV}{dt}. \tag{3.20}$$

By performing the Laplace-transform [53] and solving the equations for the voltages, the expressions can be written in the Laplace-domain as

$$V_L(s) = Lsi(s), \quad \text{and} \quad V(s) = \frac{i_c(s)}{sC}. \tag{3.21}$$

Inserting $s = j\omega$ in order to get the frequency-response [53], yields

$$V_L(s) = j\omega L \cdot i(s), \quad \text{and} \quad V(s) = -\frac{j}{\omega C} \cdot i_c(s). \tag{3.22}$$

Since Equation 3.22 presents the relationship between the current and the voltage, the reactance of the coil and the capacitor is respectively

$$X_L = \omega L \quad \text{, and} \quad X_c = -\frac{1}{\omega L}. \tag{3.23}$$

However, it is normal that an inductor and a capacitor has some resistance R, so the total impedance in both cases are commonly denoted

$$Z_L = R_L + jX_L, \quad \text{and} \quad Z_c = R_c + jX_c. \tag{3.24}$$

So, a coil in series with a resistance, R, will result in a total impedance of

$$Z = R + R_L + j\omega L. \tag{3.25}$$

Thereby, circuits containing impedances that are not perfectly matched will have a real and imaginary part. If that is the case, the circuit will have a complex power that can be calculated as

$$S = VI^* = P + jQ = |S|\angle\theta, \tag{3.26}$$

where θ indicates the size of the active power (real) and the reactive power (imaginary) as can be seen in Figure 3.2 that shows the well-known power triangle.

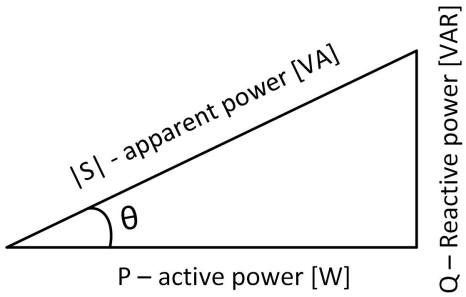

Figure 3.2: Power triangle.

Assuming that the inductor and the capacitor are in series and that they are operated at the resonance-frequency that is calculated based on the initial reactance of the coil and capacitor, the following relationship are true: An angle that is: $0 < \theta < 90$, means that the coil has been made larger than its initial reactance, and thereby, the circuit will have an inductive characteristic. The opposite is the case if $-90 < \theta < 0$, and the circuit will therefore have a capacitive characteristic. The biggest problem with having too much inductance/capacitance in the circuit is that for a fixed voltage-source, V, the current, I, needs to increase in order to deliver the same amount of power. As a result, if the reactive part is big enough, it will result in bigger losses in the circuit. In addition, to minimize VA ratings, the circuits are normally operated at a resonant state, also called zero phase angle (ZPA) - operation. The resonant state implies that the frequency is such that:

$$j\omega L + \frac{1}{j\omega C} = 0.$$

Thus giving,

$$\omega_0 = \frac{1}{\sqrt{LC}}. \tag{3.27}$$

Operating exactly at this frequency will although cause more switching loss in the inverter

when using the hard-switching technique. Therefore, the primary side can be slightly shifted away from the resonant frequency in order to make the switches operate with zero voltage switching (ZVS) and zero current switching (ZCS) [1, 54, 55]. This will also be done for the design that are to be designed in chapter 4.

3.2.3 Q-factor

The quality-factor of a coil is given as,

$$Q = \frac{\omega_0 L}{R}, \tag{3.28}$$

where ω_0 is the resonance-frequency (eq. 3.27), and R represents the resistance of the coil. It has been shown that the impedance of a coil is:

$$Z_L = R_L + jX_L = R_L + j\omega L.$$

The quality-factor of a coil is therefore simply the relationship between the reactance and the resistance of the coil. For an ideal coil, Q will approach infinity. In IPT, the losses that are in series with the coil, such as the resistances in the capacitor, the wire and the equivalent resistance of the rectifying bridge can sometimes be included in this measurement. Since such losses are in general quite small, it will still work as an indication of the coils quality. Sometimes, the reactance of the coil is measured against the equivalent resistance of the battery. A reason for this is because many researchers prefers to analyse a lossless system. This case is still referred to as the quality-factor of the coil, but in reality it serves as a measurement of the quality of the system. This can act as a source of confusion. However, measuring the quality factor in such a way serves its own purpose, e.g. as a guidance for designing the system in order to avoid bifurcation [56] as will be shown in subsection 3.3.1.

Having coils with a high quality is of great interest for an IPT system. The overall efficiency is in fact under certain assumptions only dependant on a high quality Q and a great magnetic coupling k, as will be presented later. Since Q is decided in the design, it is best to ensure a coil with a high Q is used. For brevity, the total quality of the coils in an IPT system is sometimes written as,

$$Q = \sqrt{Q_1 \cdot Q_2} = \sqrt{\frac{\omega_0 L_1}{R_1} \cdot \frac{\omega_0 L_2}{R_2}}. \tag{3.29}$$

3.3 Brief overview of different compensating topologies

The compensating capacitor that is meant to cancel the reactance of the coil can be placed in series or parallel on both sides of the circuit. This gives rise to four different compensating topologies, denoted:

- Series - Series (SS).
- Series - Parallel (SP).
- Parallel - Series (PS).
- Parallel - Parallel (PP).

The first letter of the abbreviation denotes the placement of the capacitor with respect to the sending side coil, while the second letter gives the location of the capacitor with respect to the receiving side coil. The system characteristics will be different for all these topologies, and there is a lot of analysis done on each of them in literature. It is found that how the compensating capacitor is placed will among other things affect: Power transfer capability, constant voltage or current output, efficiency, bifurcation and misalignment-tolerance [54, 57, 58]. This is not an exhaustive list, but it shows how much the characteristics can be affected by the placement. In later years, other compensation topologies where there is used multiple capacitors or coils for cancelling the reactance (SS LCC, PP LCC, PP LCL) has been developed and aims to improve system performance [54], and it is found that some shows promising results in terms of reduced stress on power converters. These compensation topologies will however increase the costs, weight and volume. In addition, they lead to more advanced system equations, and is often used for multi-load WPT. Such compensation will therefore not be further discussed.

A comparison of the different compensating topologies with respect to the intended use was done in the project thesis [28]. It concluded that the SS topology is the most suitable topology since it provides a robust system that is less dependant on the variables in the system. This yields for instance when the system is exposed for variable coupling-conditions, since the SS-topology results in small variations in resonance frequency [17]. In addition, it has been shown that the SS topology is suitable for high-power applications, while the SP topology are more suitable to obtain a higher efficiency [59]. The main differences in the characteristics can however be summed up by Table 3.3 as given in [54].

Table 3.3: Comparison of different compensation topologies [54]

Topology	Features	Topology	Features
SS	• High tolerance of system parameters • No reflected reactance • Most popular topology for practical applications • Preferred at $\omega^2 M^2/R_L < M^2 R_L/L_S^2$	SP	• Reflected reactance relating to operating frequency • Be able to supply a stable current
PS	• No reflected reactance • Be able to supply a stable voltage	PP	• Reflected reactance relating to operating frequency • Preferred at $\omega^2 M^2/R_L < M^2 R_L/L_S^2$

3.3.1 Bifurcation

Bifurcation is simply the phenomena when the system goes from having one singular resonant frequency, to having multiple. As a result, bifurcation is also often termed pole splitting [60]. The advantage of bifurcation is that when the system operates at the exact limit, the range of operation where the system has zero reactive power increases. This property has lead to some proposed design-rules to ensure that the system that is designed will operate at the bifurcation-limit [60]. Designing a system that operates at the bifurcation limit is for this reason of great benefit when controlling output power by changing the switching frequency of the inverter. In this thesis, such control will be further discussed and implemented in Simulink in chapter 5. Wang et al. [56] provides a thorough analysis of the phenomena of bifurcation and what requirements it sets for the design of inductive power transfer for all compensation-topologies. Since it is decided that the focus of this thesis will be on the SS-topology, the reader is referred to [56] for the requirements to the other topologies. For a SS-topology, they found that to avoid bifurcation, the quality-factor of the coils need to follow the following relationship:

$$Q_1 > \frac{4Q_2^3}{4Q_2^2 - 1}. \tag{3.30}$$

The inductive transfer is designed as an ideal lossless case, hence the only resistance present

in the circuit is the load-resistance that represents the battery. For this reason, Equation 3.28 cannot be used since that equation relates to the resistance in the coil, resulting in an infinite quality factor. The quality of the coils are instead measured relative to the size of the load resistance. Since the coil in the secondary part of the circuit is in series with this load, Q_2 is simply calculated as

$$Q_2 = \frac{\omega_0 L_2}{R_L}. \tag{3.31}$$

The coil on the primary side however is not in series with the load-resistance, therefore, the load resistance needs to be reflected to the primary part resulting in Q_1 to be calculated as

$$Q_1 = \frac{L_1 R_L}{\omega_0 M^2}. \tag{3.32}$$

A typical design-choice is to pick Q_2=5 [56]. The best way to explain the bifurcation-limit is by a simple plot based on this typical design-choice. If Q_2 is chosen to be this value, then the right side of Equation 3.31 will be

$$\frac{4Q_2^3}{4Q_2^2 - 1} = 5.051 \approx 5. \tag{3.33}$$

This means that if the coil on the primary side has a quality-factor of Q_1=5, the system operates at the bifurcation-limit. A higher value ensures no bifurcation, while a lower value allows bifurcation. The frequency response for different values around the bifurcation-limit can be seen in Figure 3.3.

The phase-angle between the current and the voltage on the primary side is an indication of the size of the reactive part of the impedance that represents the whole circuit as will be discussed in subsection 4.3.3. The important part is to keep this phase-angle to zero in order to avoid reactive power in the circuit. It is clear from Figure 3.3 that the system for all quality-factors of the coil will deliver the wanted power at the common resonance-frequency ($f/f_0 = 1$). A low Q_1=3 has three resonant frequencies at approx. $0.935 \cdot f_0$ and $1.107 \cdot f_0$, while a high Q_1=7 has only one resonant frequency at f_0. However, when the system is designed for operation at the bifurcation-limit, it can be observed that the circuit has very close to ZPA for all frequencies between $0.995 \cdot f_0$ to $1.02 \cdot f_0$ which enables a wider range of operation for which the system can operate with unity power factor. This property becomes even more visible when modelling the circuit with a constant voltage battery, than a constant resistance that represents the battery. This will be shown and taken advantage of in chapter 5.

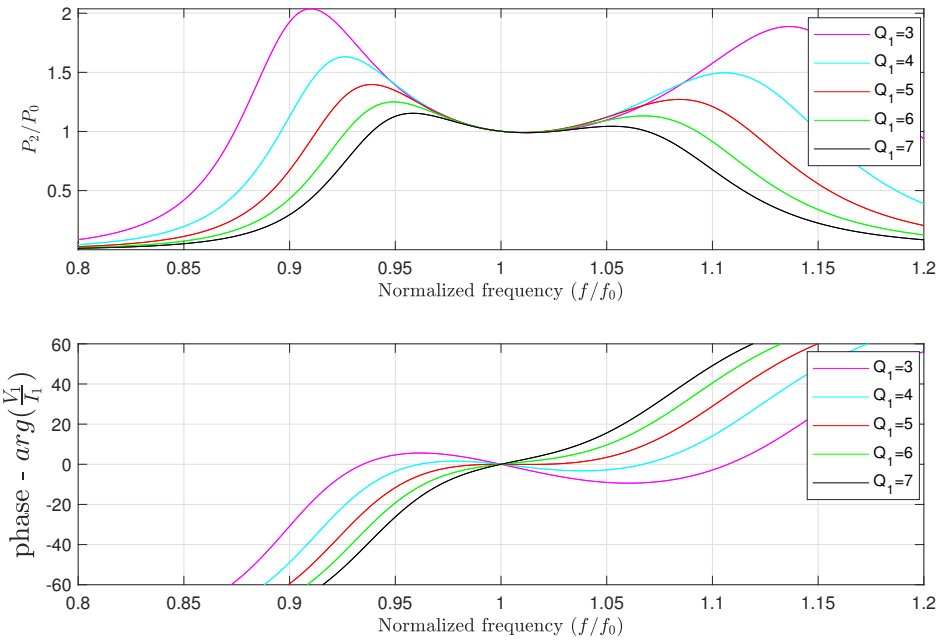

Figure 3.3: Normalized output power and the phase angle of the primary side for different quality-factors of Q_1.

3.4 Benefits and challenges with inductive power transfer subsea

3.4.1 Benefits

As discussed in section 2.1, AUVs used for exploration are today quite dependant on surface vessels. In addition, even though the biggest operators within the petroleum sector has started to see the potential for permanently stationed AUVs on the seabed, the operations today are still quite far away from such a solution. Today, it is normal to have ROV operators on the rig, who will deploy one or multiple ROVs (depending on the operation) on demand. For ROVs, the normal configuration is direct power-supply through a tether, where the end of the tether is either a male wet-mate connector (fig. 3.4 (b)) or directly integrated to the design of the UV for robustness. As a result, charging subsea is still rarely seen in commercial applications. It is clear that the biggest users of UVs in their business are faced with solutions where the operation is very dependant of manual labor. This dependency will in turn result in higher operational costs and higher emissions.

A clear benefit of having inductive charging on the seabed is that the AUVs can stay permanently underwater, performing maintenance-tasks regularly and tasks directly related to operation with a significant decrease in response-time. This will in turn lead to an increased safety, as it is more likely that damages or wear are detected before they become crucial. In

addition, advanced AUVs like Eelume can become completely tether-less, making them even more agile. It is also thinkable that the exploring AUVs could use spare dockings to charge and exchange data, enabling them to embark in longer and more extensive missions, thereby increasing the rate of data-retrieval. These AUVs will then also become less dependant on surface vessels, thereby reducing costs and emissions. In addition to AUVs being charged, a thinkable application is for the AUVs to charge sensors and other battery-powered equipment that is permanently stationed subsea. These sensors are low power consuming electronics, but their battery packages needs to be replaced regularly, which is most commonly done by ROV operators. This is time-consuming, and could be done much more effective by integrating a system for low-power wireless transfer from the AUVs.

Figure 3.4a shows a possible design of a loosely coupled transformer (LCT) for an underwater high power transfer system. Comparing that design to the wet-mate connector depicted in Figure 3.4b, another clear advantage of wireless power transfer is observed. First of all, the LCT has rotational freedom which makes them less prone to failure due to the dynamics in the sea. Cyclic stress due to waves and changing currents combined with high pressure ratings are hostile environments for metal, and can lead to hydrogen induced stress cracking (HISC) for connections like the wet-mate connector. It is also clear that a female contact that is stationed unprotected in the sea will be very exposed for dirt and algae growth, and for this reason it will be hard to reconnect it with a male contact. This leads to wet-mate connectors being very limited to be used as a charging topology subsea and is coherently always connected to a male contact.

(a) (b)

Figure 3.4: (a)Design of (left) semiclosed and (right) nonclosed LCT [25]. (b) Wet-mate connector [61].

The overall benefits can be summarized as:

1. Less dependant on surface vessels - lower operational costs and reduced emissions.
2. AUVs can embark in longer and more extensive missions - increased data retrieval.
3. Regular maintenance work and fast response time - increased safety.
4. Small wear on contacts - increased life cycle - reduced costs.

3.4.2 Challenges

The challenges related to wireless charging subsea can be split into two categories. The first one is how the properties of the water directly affects the power transfer, and the second is how marine environments affects installed equipment.

Challenges related to power transfer - Inductive power transfer in seawater compared to air is in fact surprisingly similar, and multiple articles points out that it is eddy current loss that is the main difference between transmitting power in seawater, compared to air and freshwater [9–11, 25, 26, 50]. In fact, the efficiency for inductive power transfer in seawater can be written as [11],

$$\eta_{seawater} = \frac{P_{load}}{P_{air} + P_{eddy}}, \tag{3.34}$$

which shows that it is the eddy-current that is of most concern. To understand why eddy-currents is a problem in seawater, and not for freshwater and air, a further look into the phenomena of eddy currents is necessary. The origin of eddy currents comes from Faraday's Law of induction (Maxwell's third law), which states that an emf is induced with a time-varying flux as

$$emf = -\frac{d\phi}{dt}. \tag{3.35}$$

This emf will in turn create circulating currents, called eddy currents in the connecting medium. Since this current does not serve any purpose, they are considered loss in the rate of $P = I^2/R$. Eddy currents is a well known problem for transformers, as they are made out of conducting materials. This problem is coped with by laminating the core, and between these plates are thin layers of insulation that stops these current from swirling around. Since the material between the two coils in inductive power transfer will be seawater, solutions like that is not possible. Therefore, the design needs to take into consideration that the seperating material is seawater. Deriving the mathematical expressions for the eddy currents are quite complicated. In [11], they derived the expression for the eddy current loss in the cylindrical coordinate (r-z) for operation in seawater from the Maxwell equations as:

$$P_{\text{aec}} = \frac{2\pi N}{\sigma_2} \int_0^{\infty} \int_0^{D} |\sigma_2 E(r,z)|^2 dr dz, \tag{3.36}$$

where E(r,z) denotes the electric field intensity in seawater,

$$E(r,z) = j2\pi f_\omega \mu_2 r_0 I_1 \int_0^{+\infty} J_p(\gamma r_0) \times J_p(\gamma r)(\tau_1 e^{\lambda z} + \tau_2 e^{-\lambda z}) d\gamma. \tag{3.37}$$

This is a quite comprehensive equation, but it is possible to extract essential relations as it stands. In Equation 3.36, the term $E(r,z)$ is squared, meaning that the eddy current will have a quadratic relationship to both the primary current I_1 and the operating frequency f_ω. The latter will be dominating in terms of magnitude, so this explains why it is best to avoid operating a system for IPT in seawater at high frequencies. The reason for why eddy currents is a problem in seawater and not in freshwater can also be explained by Equation 3.36. From Table 3.2, there is a significant difference in the conductivity (σ) of the three mediums. According to Equation 3.36, the size of the eddy current losses is linear to the conductivity of the material. A newer and more accurate - however more complicated expression for the eddy current loss in seawater was found in [54]. To summarize, Cheng et al. [25] did a thorough analysis of all loss in the system, and found that as long as the frequency is f<36 kHz for a system transferring 10 kW, the losses due to eddy currents is not that significant. Niu et al. [26] found that there is little difference in power transfer in air, seawater and freshwater for frequencies in the range 40-140 kHz for a system delivering 1 kW. Zhou et al [11] did extensive research on the relationship between the frequency and the equivalent load resistance and how it affects eddy current loss. They also found that as the resonant frequency increases, the system will get a shift in the resonant frequency when operated in seawater compared to air. They conclude that this shift is possibly caused by the increase in the eddy current as a result of the high frequency. Based on this, it is decided that the system in this thesis should be designed to operate at $f_\omega = 20kHz$, and thereby the guidelines set in literature is followed.

Challenges related to how marine environments affects installed equipment

First off, marine environments has to be defined. The UUVs that can utilize wireless charging are ranging from charging at sea-level as part of a vessel, and all the way down to the deepest subsea-installations at approx 3000 mbsl. Based on this, the marine environments that the equipment can face is:

- Corrosive.
- Exposed for algae growth.
- Hydrodynamics like waves and currents.
- High pressure.

Equipment installed subsea used by the industry is tested for such conditions, so they are common challenges to overcome. Corrosion is normally prevented by using galvanic anodes. Algae growth is harder to actively prevent from growing, but can easily be removed by using the

washing-tools that are installed on ROVs. Such a task would fall under the regular maintenance that the permanently stationed AUVs would perform, so programming the AUV to wash its own hub regularly would cope with this problem. The rotational and to some extent alignment freedom of a wireless charging would reduce the damaging effects of the cyclic stress that comes from waves and current, but it will be shown in chapter 5 how these hydrodynamics are likely to affect the characteristics of the power transfer. Regarding the high pressure, the normal solution found today is pressurized systems in which the power circuits are assembled in their entirety in steel vessels at atmospheric pressure. As operational water depths and converter power rating increase, pressure vessels become increasingly heavy and unwieldy due to the need of an increased wall thickness. SINTEF is therefore working on creating pressure-tolerant power circuits through projects in collaboration with the industry [62].

Chapter 4

Designing a SS-compensated inductive charger

In this chapter, the same system will be designed twice under two different assumptions. These assumptions leads to two different ways of analyzing the systems, that will from here on after be denoted:

- System 1 - Constant resistance load.
- System 2 - Constant voltage load.

For the first system, the battery will be represented as an equivalent constant resistance, while for the other system, the battery will be modelled as a DC voltage source with a constant voltage. A Simulink-model will be built for both cases, in order to verify the calculations done for the respective systems. Lastly, the differences in the frequency-response between system 1 and system 2 will be compared. Figure 4.1 shows the overall picture of a battery-charging resonant inductive coupled circuit that is SS-compensated.

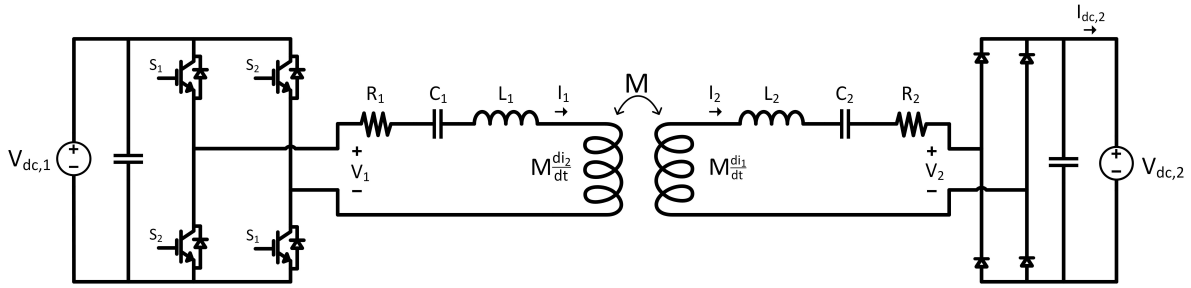

Figure 4.1: A series-series compensated resonant circuit for inductive charging of the battery $V_{dc,2}$.

The most normal approach presented in literature is to view the battery to be charged as an equivalent resistance. However, due to the characteristics of battery charging, and its demands to the dynamics of the system-parameters this is generally not applicable in all scenarios, especially when the point of operation is moving far away from the nominal point of operation as will be discussed in section 4.8. This issue was raised in [1], where they addressed the major assumption of modelling the battery as an equivalent resistance with respect to the frequency response. Although the frequency-response of the system is accurate at and near

the resonance-frequency, the dynamic response will in fact be different for the two systems, in the way that a constant resistance load will always have a more damped response as discussed in [63]. There are fewer articles that models the battery as a constant voltage load. However, some articles uses a CVL for modelling and system analysis [23, 24], without discussing much the differences. This thesis will further investigate the two different ways of analyzing the circuit, and try to highlight the main differences by comparing the frequency response of the two systems in section 4.8.

Even though the systems behavior in the two cases are quite different, the calculations on both systems is identical until inserting the value for the load-resistance. This is because the only thing that separates them equation-wise is for system 1: A constant R_L, and for system 2: A R_L that varies with the system parameters to ensure a constant voltage over the battery at all operating frequencies. This means that the equations for the overall system can be derived similar for both systems. For now, the load in both cases will be denoted R_L on the DC-side of the rectifier. For easier analysis of the circuit that is depicted in Figure 4.1, equivalent expressions for the inverter and the rectifier needs to be found.

4.1 Modelling the rectifier

The load is on the rectified side of the circuit, and thus it is convenient to express the load as an equivalent resistance R_{eq} in series with the rest of the circuit as shown in Figure 4.2. This equivalent resistance is equal to

$$R_{eq} = \frac{V_2}{I_2}. \tag{4.1}$$

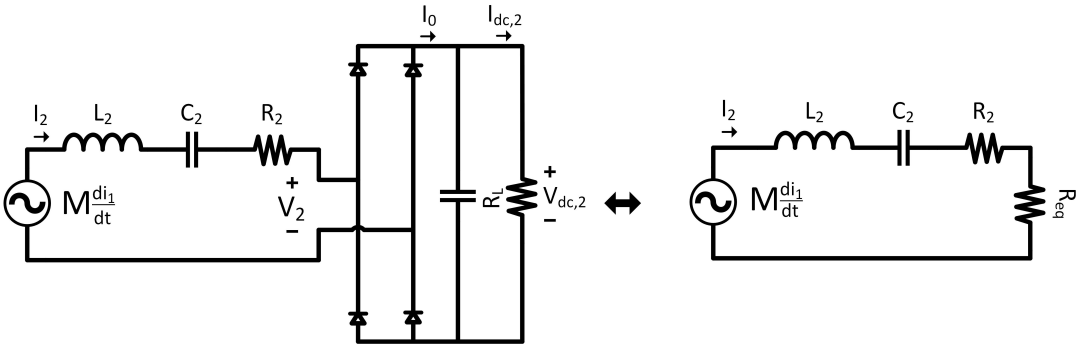

Figure 4.2: Rectifier modeled as an equivalent resistance.

The characteristics of a rectifier with smoothing capacitor, is that the voltage V_2 is a square wave on the input to the rectifier, while the current I_0 is a rectified sinusoidal with an amplitude I_2 on the output as depicted in Figure 4.3.

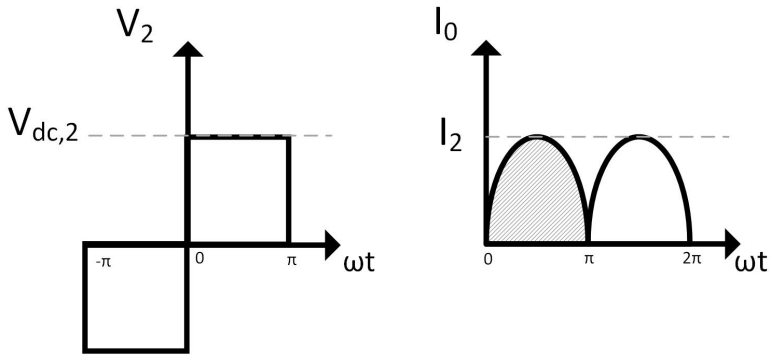

Figure 4.3: Voltage and current characteristics related to the rectifier.

Knowing this, Fourier-analysis can be utilized in order to find an expression for V_2 as a function of $V_{dc,2}$.

Recalling Fourier:

$$f(x) = a_0 + \sum_{n=1}^{N} \left[a_n cos\left(\frac{n\pi}{L}x\right) + b_n sin\left(\frac{n\pi}{L}x\right) \right], \tag{4.2a}$$

$$a_0 = \frac{1}{2L}\int_{-L}^{L} f(x)dx, \tag{4.2b}$$

$$a_n = \frac{1}{L}\int_{-L}^{L} f(x)cos\left(\frac{n\pi x}{L}dx\right), \tag{4.2c}$$

$$b_n = \frac{1}{L}\int_{-L}^{L} f(x)sin\left(\frac{n\pi x}{L}dx\right). \tag{4.2d}$$

where the period is described by,

$$T = 2L. \tag{4.2e}$$

The square-wave depicted in Figure 4.3 is an odd-function, hence a_0 and a_n is zero. The square-waves characteristics resembles a sine-wave, and is therefore easiest described using b_n. The square-wave can be described by the following function,

$$f(\omega t) = \begin{cases} -V_{dc,2} & -\pi \leq \omega t \leq 0 \\ V_{dc,2} & 0 \leq \omega t \leq \pi \end{cases} \tag{4.3}$$

The first harmonic of this square-wave is (Eq. 4.2d),

$$b_1 = \frac{1}{\pi}\left[\int_{-\pi}^{0} -V_{dc,2}sin(\omega t)dt + \int_{0}^{\pi} V_{dc,2}sin(\omega t)dt\right] = \frac{4}{\pi}V_{dc,2}. \tag{4.4}$$

By using Equation 4.2a, an expression for the first harmonic Fourier expansion of the square-wave representing the voltage on the input to the rectifier is given as,

$$V_2 = \frac{4}{\pi}V_{dc,2}. \tag{4.5}$$

The average of the current exiting the rectifier can because of its symmetry easily be obtained by averaging its value over a period. The expression for the current is therefore,

$$\begin{aligned} I_{dc,2} &= \int_{0}^{\pi} \frac{I_2 sin(\omega t)}{\pi} d(\omega t), \\ I_{dc,2} &= \frac{2}{\pi}I_2. \end{aligned} \tag{4.6}$$

This gives a new expression for the load given by

$$R_{eq} = \frac{V_2}{I_2} = \frac{\frac{4}{\pi}V_{dc}}{\frac{\pi}{2}I_{dc}} = \frac{8}{\pi^2}R_L. \tag{4.7}$$

This expression is equivalent to the one obtained in [64].

4.2 Modelling the inverter

It is also convenient to model the inverter as an equivalent AC voltage source for easier analysis of the circuit as Figure 4.4 shows.

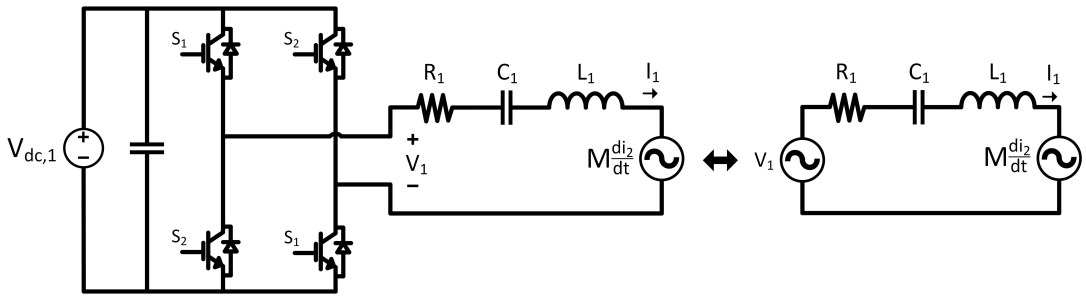

Figure 4.4: Simplifying the inverter into an alternating voltage source that outputs a square wave.

The easiest way to set up an inverter is for it to output a square wave where the amplitude of the output is equal to $V_{dc,1}$. This is obtained by opening S_1 when S_2 is closed and vice versa at the rate of the frequency that is wanted on the output. In RIPT this frequency is normally above 1 kHz, and therefore it is normal to use IGBTs or MOSFETs with applied PWM signals. In the case of an ideal inverter with no losses, this gives the same relationship between the input ($V_{dc,1}$) and the output (V_1) voltage, as was analyzed over the rectifier. This means that the relationship between $V_{dc,1}$ and V_1 can be obtained by Equation 4.5 as

$$V_1 = \frac{4}{\pi} V_{dc,1}. \tag{4.8}$$

Converting it to RMS-value gives,

$$V_1 = \frac{4}{\sqrt{2}\pi} V_{dc,1} = \frac{2\sqrt{2}}{\pi} V_{dc,1}. \tag{4.9}$$

Summarizing the analysis done, the new, equivalent circuit to be analyzed is shown in Figure 4.5.

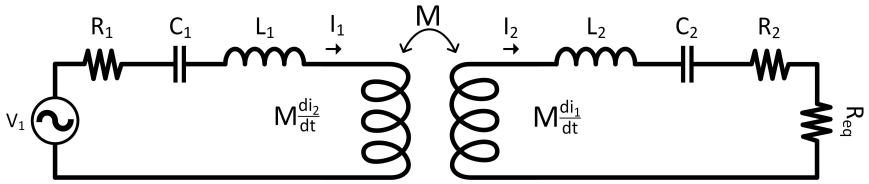

Figure 4.5: Simplified representation of a SS-compensated circuit for IPT where the battery is represented with an equivalent resistance R_{eq}.

Where,

$$V_1 = \frac{2\sqrt{2}}{\pi} V_{dc,1}, \quad R_{eq} = \frac{8}{\pi^2} R_L.$$

This equivalent circuit is valid for both cases, keeping in mind that for system 1 R_{eq} will be a constant, while for system 2 R_{eq} will vary with the parameters of the system.

4.3 Analyzing the equivalent circuit

Since the battery can mathematically be modelled as an equivalent resistance (R_{eq}) in both systems, the overall circuit equations is in fact identical for both cases until finally inserting the value for the load resistance. These system equations will be derived in this section.

There is many ways to analyze this system, and it is found that authors tend to differ in which way that is the best approach. The reason for this is mainly because of two things. The first one is the many different equivalent ways of representing the circuit. Each of these representations results in different system equations. However, the root to the different circuits is typically how the link between the primary and the secondary side of the circuit is modelled. Many articles prefer using the T-model or the cantilever-model as they can make it easier to analyze the circuit in terms of the transformers characteristics and performance [49]. In the following analysis, the traditional equations for mutual coupling between two coils as derived in subsection 3.2.1 (eq. 3.17), which are the same as given by *MATLAB* [65] will be used.

The second reason is the use of system-properties to simplify or rewrite equations. There are a lot of different ways to rewrite the system-equations in terms of what properties that are interesting. For instance, in literature the most common rewrites is introduced by the following relations, and also their relations in-between:

$$M = k\sqrt{L_1 L_2}, \tag{4.10}$$

$$\omega_n = \frac{1}{\sqrt{L_n C_n}}, \quad n = 1, 2, \tag{4.11}$$

$$Q_n = \frac{\omega_0 L_n}{R_n}, \quad n = 1, 2, \tag{4.12}$$

$$X_n = \omega L_n - \frac{1}{\omega C_n}, \quad n = 1, 2. \tag{4.13}$$

In addition, literature differs between analyzing the circuit in the Laplace-domain and the frequency-domain. Also, by only analyzing the response at the resonant frequency a lot of simplifications can be done. For consistency, the further analysis will be done with respect to simplicity while keeping all the information about the circuit at all frequencies. From here on after, the load-resistance on the AC-side of the rectifier will be denoted R_L instead of R_{eq}, because it is better suited to describe the load resistance. This is also the normal syntax used in literature. It is however very important to remember the relationship over the rectifier, ensuring that the resistance (now R_L) is multiplied with $\pi^2/8$ when moved to the DC-side of the rectifier.

It is convenient to find an expression for the currents in both sides of the circuit. These can be found by analyzing the system equations as given by Figure 4.5 as

$$\begin{aligned} V_1 &= (R_1 + \frac{1}{sC_1} + sL_1)I_1 + MsI_2, \\ V_2 &= (R_2 + \frac{1}{sC_2} + sL_2)I_2 + MsI_1. \end{aligned} \tag{4.14}$$

This is two equations with three unknowns (I_1, I_2 and V_2) so this set of equations is underdetermined as it stands. However, the relationship between V_2 and I_2 can simply be obtained by ohms law. This relationship makes these equations easily solvable for I_1 and I_2 by defining,

$$\begin{aligned} Z_1 &= R_1 + \frac{1}{sC_1} + sL_1, \\ Z_2 &= R_L + R_2 + \frac{1}{sC_2} + sL_2. \end{aligned} \tag{4.15}$$

Now, the system-equations can be rewritten as,

$$\begin{aligned} V_1 &= Z_1 I_1 + MsI_2, \\ 0 &= Z_2 I_2 + MsI_1. \end{aligned} \tag{4.16}$$

Sorting the equations to represent them on matrix-form and solving for the currents gives the expressions for the currents in the primary and the secondary circuit:

$$\begin{bmatrix} V_1 \\ 0 \end{bmatrix} = \begin{bmatrix} Z_1 & Ms \\ Ms & Z_2 \end{bmatrix} \begin{bmatrix} I_1 \\ I_2 \end{bmatrix} \tag{4.17}$$

$$\begin{bmatrix} I_1 \\ I_2 \end{bmatrix} = \frac{1}{Z_1 Z_2 - M^2 s^2} \begin{bmatrix} Z_2 V_1 \\ -MsV_1 \end{bmatrix} \tag{4.18}$$

With these equations, the most important information about the system is obtained. Z_2 will because of R_L be different for the two systems. Therefore, the load resistance will be derived for each case in the next sections.

4.3.1 Constant resistance load

When designing a system for wireless charging of a given battery, the load resistance is normally calculated by looking at the relationship between the power that the battery is able to receive ($P_{dc,2}$) and its nominal voltage ($V_{dc,2}$). This is simply calculated using the following equation [66]:

$$\begin{aligned} R_L &= \frac{V_{dc,2}}{I_{dc,2}}, \\ &= \frac{V_{dc,2}^2}{P_{dc,2}}. \end{aligned} \tag{4.19}$$

Some articles however focuses on finding the optimal load resistance R_L in order to obtain maximum efficiency or maximum power output by setting their differentiated expressions to zero and solving for R_L [67–69]. The size of R_L will also affect the phenomena of bifurcation as shown in subsection 3.3.1. However, having a constant resistance load creates a linear relationship between the current (I_2) and the voltage (V_2) decided by the size of the resistance R_L. This means that the voltage over the battery will change when the current changes. This is however not correct in a practical implication, thereby creating an error between the model and the real life system when moving away from the operating point. However, modelling the battery as a constant resistance load simplifies the calculations extensively and provides correct results near the nominal power (P_0) which is in most cases is the only interesting point of operation. This might be one of the reasons for why the inconsistencies between the two ways of modelling the battery has not yet been extensively addressed in literature.

4.3.2 Constant voltage load

From Figure 4.6 it is trivial to see that the system equations as given by Equation 4.14 is still valid. However, V_2 is now constant, meaning that it will not have a linear relationship with the current as decided by R_L in the same way as for system 1. Still, if it is wanted to model this system with an equivalent resistance (R_L) that should represent the battery, an equation that varies with the parameters in the system in order to have a constant DC-voltage over the battery $V_{dc,2}$ when the current is varying needs to be found. In addition, since the relationship over the rectifier is just a constant, the current I_2 and the voltage V_2 needs to be in phase in order to only deliver active power to the battery.

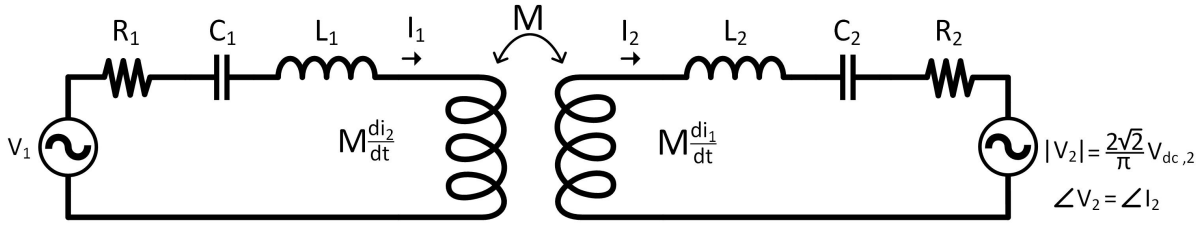

Figure 4.6: Simplified circuit of a SS-compensated circuit using harmonic approximation and CVL resulting from diode-bridge rectification [1].

From these constraints, the following relationship can be denoted:

$$|V_2| = \frac{2\sqrt{2}}{\pi} V_{dc,2},$$
$$|i_2|\,|R_L| = \frac{2\sqrt{2}}{\pi} V_{dc,2}.$$

Because $V_{dc,2}$ is always positive and the equivalent resistance R_L needs to be resistive for V_2 and I_2 to be in phase the following yields,

$$V_2 = |I_2|\,R_L.$$

This equation is solvable for R_L when taking the absolute value of I_2 as given by Equation 4.18. Doing this by hand proved to be quite intricate and not very effective when available programs for computations are available. Maple was chosen to be well suited for such a problem. The problem was solved in document-mode to make it possible to add comments to the calculations. The code for deriving the equivalent resistance in case of a constant voltage load can be found in appendix A.1. The script also shows the equations for the total impedance in the circuit. The equivalent resistance in the case of coils with loss is quite large, and hence not suited to be included as an equation in this thesis, other than in the appendix. However, in the ideal case of lossless coils, the expression for the equivalent resistance can in its most basic form be written as:

$$R_L = \frac{V_2\left|-(\omega^2(-L_1L_2+M^2)C_2+L_1)\omega^2C_1 - L_2C_2\omega^2 + 1\right|}{\sqrt{-(L_1C_1\omega^2-1)^2V_2^2 + C_1^2M^2V_1^2\omega^4C_2\omega}}. \tag{4.20}$$

Since most of the variables of this equation are constant as a part of the system (V_1,V_2,L_1,L_2,C_1,C_2) the resistance can be viewed as a variable dependant on $R_L(\omega, M)$.

It is evident that the expression under the square-root sign in Equation 4.20 needs to be positive for the resistance to be real. This expression can be factorized as

$$-(C_1L_1V_2\omega^2 - C_1MV_1\omega^2 - V_2)(C_1L_1V_2\omega^2 + C_1MV_1\omega^2 - V_2) > 0, \tag{4.21}$$

$$\sqrt{\frac{V_2}{C_1(L_1V_2+MV_1)}} \leq \omega \leq \sqrt{\frac{V_2}{C_1(L_1V_2-MV_1)}}, \tag{4.22}$$
$$\omega_L \leq \omega \leq \omega_U.$$

Equation 4.22 represents the range of operation for the system. Dropping below ω_L or going over ω_U will give zero power transfer to the load. An interesting observation from Equation 4.22 is that the range of operation is highly affected by the coupling coefficient (eq. 3.18). An increased k results in a lower ω_L and a higher ω_U, thereby creating a bigger range of operation. This relation is a property that will be utilized when controlling the power transfer in chapter 5. Another interesting observation in case of a CVL is the dynamic relationship between the voltages and the currents at the sending and receiving side of the circuit in case of operation at the resonance frequency. The resulting system equations for such a case can in the frequency domain be written as:

$$\begin{bmatrix} V_1 \\ V_2 \end{bmatrix} = \begin{bmatrix} R_1 & j\omega_0 M \\ j\omega_0 M & R_2 \end{bmatrix} \begin{bmatrix} I_1 \\ I_2 \end{bmatrix} \tag{4.23}$$

The resistances in the circuit (R_1, R_2) will have a much lower value than the product of the resonance-frequency and the mutual inductance ($\omega_0 M$) for all magnetic couplings that do not approach zero. From Equation 4.23, it can therefore be seen that a small change in I_2 will result in a big change of V_1, and a small change of I_1 will result in a big change of V_2. The following derivation aims to simplify the equations that shows this relationship: Solving this system of equations for the currents yields,

$$\begin{aligned} \begin{bmatrix} I_1 \\ I_2 \end{bmatrix} &= \frac{1}{R_1 R_2 + \omega_0^2 M^2} \begin{bmatrix} R_2 & -j\omega_0 M \\ -j\omega_0 M & R_1 \end{bmatrix} \begin{bmatrix} V_1 \\ V_2 \end{bmatrix} \\ &= \frac{1}{R_1 R_2 + \omega_0^2 M^2} \begin{bmatrix} R_2 V_1 - j\omega_0 M V_2 \\ R_1 V_2 - j\omega_0 M V_1 \end{bmatrix} \end{aligned}$$

$$I_1 = \frac{R_2 V_1 - j\omega_0 M V_2}{R_1 R_2 + \omega_0^2 M^2}, \tag{4.24}$$

$$I_2 = \frac{R_1 V_2 - V_1 j\omega_0 M}{R_1 R_2 + \omega_0^2 M^2}. \tag{4.25}$$

According to Equation 4.18, the phase of the current and voltage in the secondary circuit is phase shifted a negative 90 deg (which corresponds to -j), relative to the voltage and current in the primary circuit. In order to obtain the magnitude of the currents independent of the phase, V_2 in Equation 4.24 needs to be phase shifted into the primary-circuit by multiplying it with j and similarly, V_1 in Equation 4.25 would need to be phase shifted into the secondary circuit by multiplying it with -j. This gives the current to voltage relationship independent on phase as

[70],

$$I_1 = \frac{R_2 V_1 + \omega_0 M V_2}{R_1 R_2 + \omega_0^2 M^2}, \quad I_2 = \frac{R_1 V_2 - V_1 \omega_0 M}{R_1 R_2 + \omega_0^2 M^2}, \tag{4.26}$$

where the sign of the current in the secondary circuit depends on the direction of the coil-winding with respect to the winding of the primary coil. Assuming a completely ideal system with no losses an interesting relationship will be revealed as,

$$I_1 = \frac{V_2}{\omega_0 M}, \quad I_2 = \frac{V_1}{\omega_0 M}. \tag{4.27}$$

As can be seen, for a completely lossless RIPT-system that operates at perfect resonance, a linear relationship between I_1 and V_2, and, I_2 and V_1 appears. The size of the linear contribution is defined by the size of $\omega_0 \cdot M$, where M will under operation vary with the magnetic coupling as given by Equation 3.18. The relationship presented in Equation 4.27 is quite counter-intuitive, but it is an easy relationship to remember equation-wise, and it is thereby an easy way to better understand the dynamics of the system. The equation for I_2 as given by Equation 4.27 can also be used to obtain relationship between the power-output and the supply and battery-voltage as,

$$P_2 = \frac{V_1 V_2}{\omega_0 M}. \tag{4.28}$$

Which is a commonly used equation in literature [1, 60]. This equation is also great to show which variables that can be changed to remain the wanted power output for a change in the magnetic coupling. If the magnetic coupling increases, the output power will decrease. This effect can be counteracted by increasing the voltages V_1 and/or V_2 [20–22]. This control-method will however result in a varying current for changes in the magnetic coupling, setting strict requirements to the VA ratings of the converters in the system, which can lead to increased costs, especially for high-power systems. The system will however be operated at the resonance-frequency for all variations. This control-method is therefore often referred to as fixed-frequency control. A different approach to counteract the increased magnetic coupling is to decrease the frequency of operation. This will lead to off-resonant operation, but the currents in the system will remain fairly constant, meaning that the efficiency is less affected [1, 18, 19], and the VA requirements to the converters are minimized. This control-method is therefore deemed particularly suitable for systems that are expected to be exposed for time-varying couplings throughout the charging. This is the case for an AUV, and as a result, this form of

control will be the main focus of this thesis.

4.3.3 Power loss analysis

It is of great interest to get an overview over the sections in the system where power dissipates. This is crucial for understanding the efficiency of the system.

Total power in the system

When the entire circuit is modelled as an equivalent circuit as shown in Figure 4.7 it is trivial that all the apparent power in the circuit lays over the impedance Z_t. Since this is the impedance that represents the entire circuit, it is this phase-angle that gives an indication of how well matched the circuit is. Ideally, the phase angle of the total impedance is equal to, or close to zero. Some articles prefer a slightly inductive characteristic [1, 18, 54] which makes the switches operate in ZVS or ZCS, and thereby the VA ratings of the converters are minimized. However, a unity power factor is obtained when the capacitors is correctly matched with the coils.

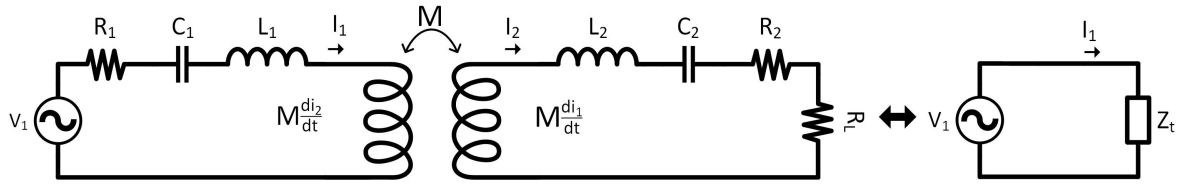

Figure 4.7: The total circuit represented with the impedance Z_t.

This impedance can be found as

$$Z_t = \frac{V_1}{I_1}. \tag{4.29}$$

The current has already been found and is given in Equation 4.18, but it is more trivial to insert the expression for V_1 given by Equation 4.16 into Equation 4.29. Doing this gives:

$$Z_t = \frac{Z_1 I_P + MsI_2}{I_1}, \tag{4.30}$$

$$= Z_1 + Ms\frac{I_2}{I_1}. \tag{4.31}$$

Further, since the total impedance splits nicely between the impedance in the primary circuit and the transfer function between the two currents, it is normal to divide the total impedance into two parts, i.e., the impedance in the primary circuit (Z_1) and the impedance that represents the secondary circuit reflected into the primary circuit, commonly denoted as Z_R as can be seen from Figure 4.8. This gives the equation for Z_t as

$$Z_t = Z_1 + Z_R, \qquad Z_R = Ms\frac{I_2}{I_1}. \tag{4.32}$$

The total apparent power in the circuit is hence given by

$$S_t = V_1 I_1^* = |I_1|^2 Z_t. \tag{4.33}$$

Power transferred to the secondary circuit

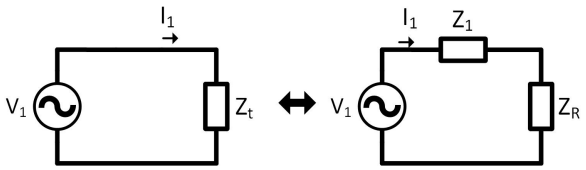

Figure 4.8: The total circuit represented with the impedance Z_1 and Z_R.

The advantage of analyzing the circuit in terms of Z_1 and Z_R is that it is easy to analyze how much power that is lost in the primary circuit, which in an ideal case is zero because it is wanted to transfer all the power created in the primary circuit to the load. In order to find an expression for the reflected impedance Z_R, the expression found for I_1 and I_2 as given by Equation 4.18 can be utilized.

$$H_i(s) = \frac{i_2(s)}{i_1(s)} = -\frac{Ms}{Z_2}. \tag{4.34}$$

By inserting the transfer function between i_2 and i_1 ($H_i(s)$) into the expression for Z_R (eq. 4.32) the final expression for the impedance representing the secondary circuit reflected into the primary circuit is found as

$$Z_R = -\frac{M^2 s^2}{Z_2}. \tag{4.35}$$

Hence, the total apparent power transferred to the secondary circuit is given as

$$S_R = V_R I_1^* = |i_1|^2 Z_R. \tag{4.36}$$

Power delivered to the load

The apparent power delivered over the load can simply be obtained from Figure 4.5 as

$$S_2 = V_2 I_2^*,$$
$$S_2 = |I_2|^2 Z_{R_L} = \frac{|V_2|^2}{Z_{R_L}^*}.$$

When the system is operated within its limits of operation as given by Equation 4.22, the characteristics of the load is purely resistive. This implies that the current will always be in phase with the voltage, meaning that the power will always be active. For this reason, the power over the battery can in fact be calculated as,

$$P_2 = V_2 I_2, \tag{4.37}$$
$$P_2 = I_2^2 R_L = \frac{V_2^2}{R_L}.$$

This is also the same equation used for finding the right load-resistance when designing a system for WPT based on the wanted output power and nominal voltage of the battery.

As discussed in subsection 4.3.2, the power over the battery can also be written as (eq. 4.28),

$$P_2 = \frac{8}{\pi^2} \frac{V_{dc,1} V_{dc,2}}{\omega_0 M}. \tag{4.38}$$

The term $8/\pi^2$ comes from the voltage-relationships over the inverter and rectifier respectively since Equation 4.38 represents the DC-side of the converters, while Equation 4.28 represents the AC-side of the converters.

Using this equation simplifies the design because one can by defining a k_{min} easily design the system to deliver the wanted power over the battery. An interesting result that this equation presents is the fact that with a higher k, the system will deliver less power. This is illustrated in Figure 4.9 for a system where $k_{min} = 0.2$.

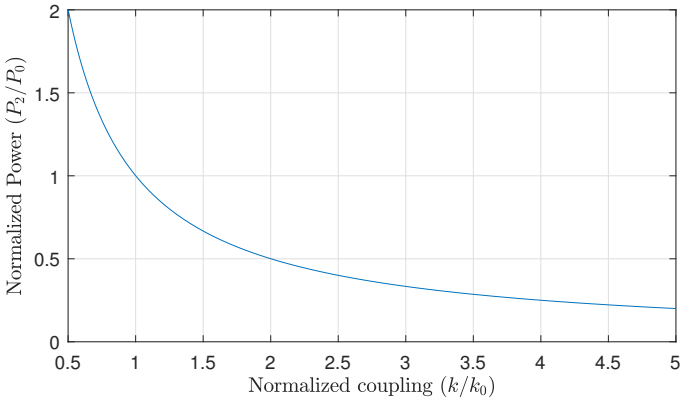

Figure 4.9: The normalized power out as a function of the normalized coupling when $k_0 = 0.2$.

This property is quite counter-intuitive, because it is easy to assume that the better the coupling, the better the transfer. Even though this does not correlate with the amount of power, a better coupling will yield a higher efficiency as will be shown in the following section.

4.3.4 Efficiency

If the efficiency of the entire system as given by Figure 4.1 were to be calculated, there is mainly four places where power is lost in a real implementation of the system.

1. Loss over inverter.
2. Loss over rectifier.
3. Loss in wires, capacitor and coil - tightly related to Q-factor.
4. Loss to the separating medium.

To simplify matters, losses over the inverter and the rectifier will not be included in any calculations done in this thesis. To reduce the third source of loss, it is normal to use Litz-wires since they are known for their low AC-resistance. The length of additional wiring needed for a real implementation is varying dependant on the application. However, the inductance of the coils is known, and typical quality-factors. Therefore, these quality-factors will serve as an indication of the total resistance on both sides of the circuit. The losses to the separating medium was addressed in section 3.4 and is best to analyze by performin FEM-analysis. To keep the design in this chapter generic as the problem description suggests, it will not be further included in the calculations.

The expression for the efficiency of a system that is SS compensated for inductive power transfer finds many forms in literature. The reason for this is again because of the very common rewrites presented earlier. Most articles assume that the system is operating at the resonance frequency before deriving the expression. The reason for this is mostly because the major part is only interested at the efficiency at the resonance-frequency. In addition, this simplification makes it a lot easier to do the derivations. However, the resulting equation is then limited to

this specific frequency. The efficiency will theoretically be highest at this frequency, thereby giving a decent indication of the total efficiency of the system nonetheless.

The focus on a system with a high efficiency is often found in literature. Showing that wireless power transfer can happen with small losses makes it easier to argue that it could replace wires without a high power-dissipation as a trade-off. Assuming resonant operation, the efficiency of the power transfer can be found from Figure 4.5 and in its most basic form it can be written as

$$\eta = \frac{\text{Power delivered to load}}{\text{Total power dissipation}} = \frac{I_2^2 R_L}{I_1^2 R_1 + I_2^2 R_2 + I_2^2 R_L} = \frac{R_L}{\left(\frac{I_1}{I_2}\right)^2 R_1 + R_2 + R_L}. \tag{4.39}$$

The transfer-function of the currents are given by Equation 4.34. Rewriting this expression when assuming operation at resonance frequency in order to fit it into Equation 4.39 gives,

$$\left(\frac{I_1}{I_2}\right)^2 = \frac{(R_L + R_2)^2}{M^2 \omega_0^2}. \tag{4.40}$$

By inserting this into Equation 4.39, the equation for the efficiency can simply be rewritten as

$$\eta = \frac{R_L}{(R_L + R_2)\left(1 + R_1 \dfrac{(R_2 + R_L)}{\omega_0^2 M^2}\right)}. \tag{4.41}$$

The great advantage by writing the efficiency in this way, is that if the resonance frequency ω_0 is

$$\omega_0^2 \gg \frac{R_1(R_2 + R_L)}{M^2}.$$

then a new expression for the efficiency can be written as

$$\eta_{\omega_0} = \frac{R_L}{R_L + R_2}. \tag{4.42}$$

This expression is again used to highlight the concepts of maximum power transfer and maximum efficiency. This is actually a quite interesting trade-off. Since R_L is representing the battery, it needs to be a certain value. However, R_2 is a system parameter that is decided by the

coils. In [71], they show that the maximum power transfer happens at impedance-matching, i.e., R_2=R_L. Operating at the point of maximum power transfer happens on the expense of the efficiency as can be seen by Equation 4.42 where this impedance-matching would lead to an unacceptable efficiency of 50 %. Many articles aims to find optimal matching of the impedances as a result, but the heavy analysis of this trade-off falls out of the scope of this thesis, as the focus will mostly be on a lossless-system or having as little resistance as possible, and to view the battery as a constant voltage load.

A different approach to efficiency-analysis is done in [4]. By taking Equation 4.41 and expressing the function in terms of the coils respective quality-factors, the function can be rewritten in terms of $a = R_L/R_2$. By differentiating this expression with respect to a, the maximum achievable efficiency η_{max} is found as,

$$\eta_{max} = \left(\frac{kQ}{1 + \sqrt{1 + (kQ)^2}} \right)^2, \tag{4.43}$$

which gives a fast indication of the efficiency with basic information about the system. Since the maximum efficiency is limited to the product of the magnetic coupling k and the inductor quality Q, this relationship is seen being denoted a figure of merit of the IPT system [60] given as

$$FOM = kQ. \tag{4.44}$$

This equation do however require that the load resistance is perfectly matched with the reflected impedance as given by

$$\begin{aligned} a &= \sqrt{1 + k^2 Q^2}, \\ R_L &= R_2 \sqrt{1 + k^2 Q^2}, \\ &= \frac{\omega_0 L_2}{Q_2} \sqrt{1 + (kQ)^2}. \end{aligned} \tag{4.45}$$

Or in terms of lossless coils ($Q_1 = Q_2 = inf$),

$$R_L = \omega_0 L_2 k. \tag{4.46}$$

Which is a design-rule that will be followed when designing the system in this thesis. The maximum efficiency for different quality-factors and coupling is shown in Figure 4.10 when k_0

is chosen to be k=0.2.

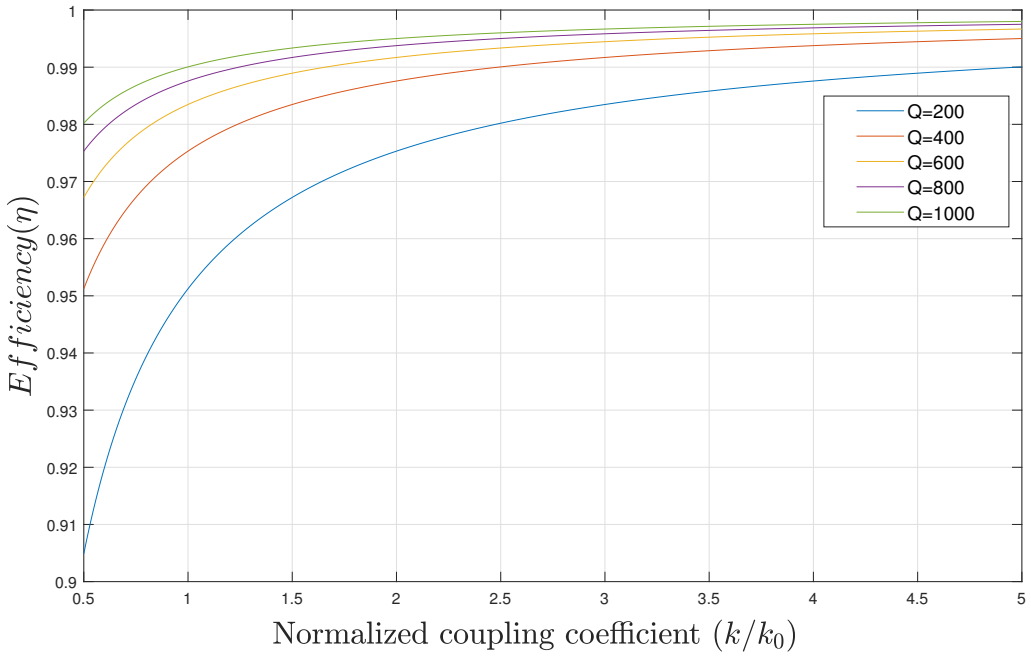

Figure 4.10: The efficiency as a function of normalized coupling for different quality-factors.

Compared to Figure 4.9 it is clear that even though the power out decreases as the coupling decreases, the efficiency of the total system will increase with a higher coupling. The reason for this increase in efficiency correlates with the power-decrease, because the current will be smaller, and thereby the losses will be smaller.

4.4 State space model of the magnetic coupling

When creating a Simulink-model for inductive power transfer, the most important part of the system is the link between the primary and the secondary side. It is found that the integrated blocks in Simulink is not sufficient in this case. Therefore, a state-space representation is derived, in order to create a subsystem that represents the link between the coils. The link between the two sides are (eq. 3.17):

$$V_1(t) = L_1\frac{di_1}{dt} + M\frac{di_2}{dt},$$
$$V_2(t) = L_2\frac{di_2}{dt} + M\frac{di_1}{dt}.$$

Performing the Laplace transform gives

$$\begin{aligned} V_1(s) &= si_1(s)L_1 + si_2(s)M, \\ V_2(s) &= si_2(s)L_2 + si_1(s)M. \end{aligned} \tag{4.47}$$

Rearranging for the currents

$$i_1(s) = \frac{V_1(s)}{sL_1} - \frac{Mi_2(s)}{L_1}, \tag{4.48}$$

$$i_2(s) = \frac{V_2(s)}{sL_2} - \frac{Mi_1(s)}{L_2}. \tag{4.49}$$

It is wanted to express i_1 and i_2 in terms of V_1 and V_2. This can be done by inserting Equation 4.49 into Equation 4.48 and thereby obtain,

$$\begin{aligned} i_1(s)\left(1 - \frac{M^2}{L_1L_2}\right) &= \frac{1}{sL_1}\left(V_1(s) - \frac{MV_2(s)}{L_2}\right), \\ i_1(s) &= \frac{1}{s} \cdot \frac{1}{L_1L_2 - M^2}\left(L_2V_1(s) - MV_2(s)\right). \end{aligned}$$

Rearranging and doing the same for $i_2(s)$ leaves us with two expressions for the current in the primary and the secondary circuit which is given as

$$i_1(s) = \frac{1}{sA}\left(L_2V_1(s) - MV_2(s)\right), \tag{4.50}$$

$$i_2(s) = \frac{1}{sA}\left(L_1V_2(s) - MV_1(s)\right). \tag{4.51}$$

With

$$A = L_1L_2 - M^2 = L_1L_2(1 - k^2). \tag{4.52}$$

4.5 Creating and verifying a Simulink model for both systems

The state space model that was derived in the previous section will make it possible to build a block diagram in Simulink using the normal signal-processing part integrated with the *powerlib*-library. Going from signal-processing to *powerlib* is done by using *Controlled current/voltage sources* and going the opposite way is done by using *Voltage/current measurements*. The block-

diagram shown in Figure 4.11 shows Equation 4.50, 4.51 and 4.52 represented as a block-diagram.

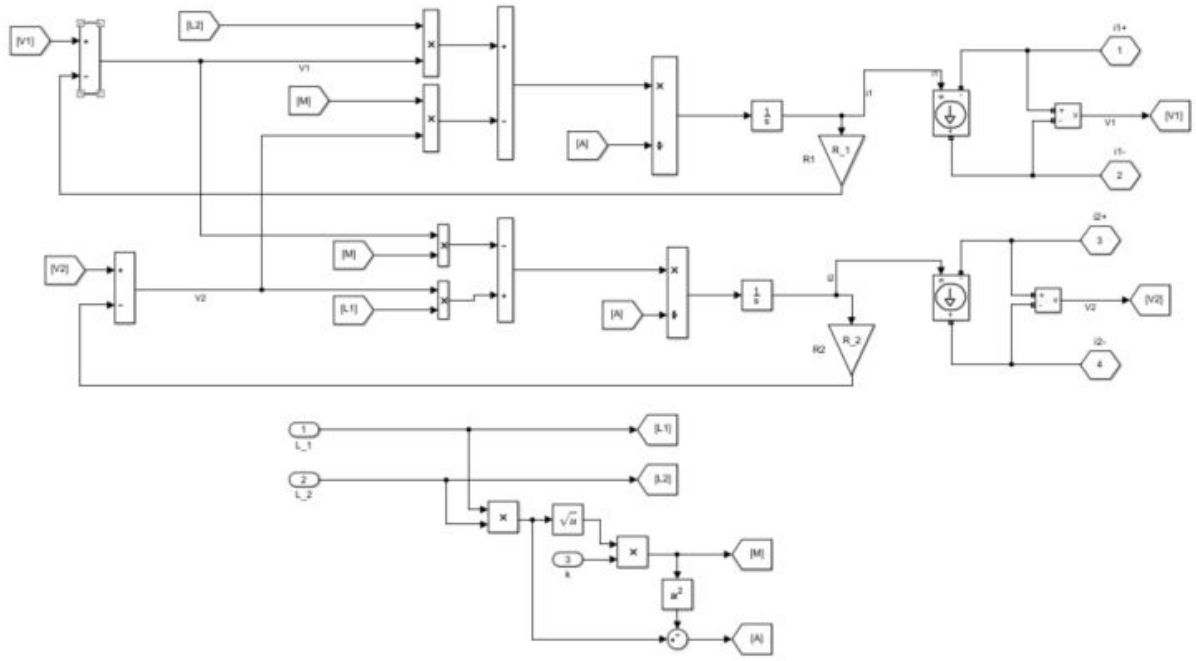

Figure 4.11: Block diagram of the mutual inductance link between the two coils.

It is additionally chosen to have the resistances (R_1) and (R_2) in the signal-part of Simulink for brevity.

4.5.1 Requirements to the system

First of all, the requirements for the system needs to be formulated. As discussed in subsection 2.1.1, a plausible design of an AUV is that the nominal battery-voltage is 300V, and that its maximum power consumption is 10 kW. It is also found that an operating frequency of 20 kHz is a suitable frequency for such an application (sec. 3.4). In addition, the purpose of this thesis is to exploit the phenomena of bifurcation. With regards to control of the system, a reference case is chosen to be the following:

At a minimum coupling coefficient k_{min}, the system should operate at the bifurcation limit. The system should also be perfectly balanced, meaning that the design needs to obey the following design-rule [60].

$$\frac{L_1}{L_2} = \left(\frac{V_{dc,1}}{V_{dc,2}}\right)^2 . \tag{4.53}$$

It is worth noting that in a practical design, the value of L_2 would need to deviate with approx. 15-25 % from this design-rule in order to avoid bifurcation [60]. This is especially

important if the system is regulated to ensure zero angle of the total impedance. This will however not be further discussed since the focus will be on maintaining a nominal output-power without phase-tracking. For this reference-case, there has not been introduced any constraints by the means of coil-size and/or size of supply-voltage. For simplicity, it is therefore chosen that $L_1 = L_2$ with corresponding cancelling capacitors $C_1 = C_2$ and $V_{dc,1} = V_{dc,2}$. Since $V_{dc,2}$ will depend on the battery's SOC as discussed in subsection 2.1.1, it will affect the systems characteristics if it is not ensured that the voltages are the same on both sides of the circuit when $L_1 = L_2$ and the system is meant to be perfectly balanced. This will introduce some additional problems related to the amount of power transferred, so for simplicity, it is assumed that the voltage over the battery will remain constant throughout the charge.

Table 4.1 provides an overview of which parameters the inductive power transfer are to be designed with respect to.

Table 4.1: Design-parameters.

Parameter	Value
Nominal Power out (P_0)	10 kW
Voltage over battery	300 V (V_0), 340 - 201 V (SOC)
Nominal frequency (f_0)	20 kHz
Minimal coupling (k_{min})	0.2

4.5.2 Design - Constant resistance load

The load-resistance that are to represent the battery in the case of a constant resistance load is simply found by Equation 4.19. From this, the value of R_L will be

$$R_{L,dc} = \frac{V_0^2}{P_0} = \frac{300^2 V^2}{10kW} = 9\Omega. \tag{4.54}$$

Moving the resistance to the left side of the rectifier using Equation 4.7 gives

$$R_{L,CRL} = \frac{8}{\pi^2} R_{L,dc} = 7.2951\Omega. \tag{4.55}$$

The system should be designed so that it operates at the bifurcation-limit under a minimum coupling coefficiency condition (k_{min}). As discussed in subsection 3.3.1, it is found that the requirement for a SS-topology to avoid bifurcation is that the quality-factor of the coils should follow the following relationship (eq. 3.30):

$$Q_1 > \frac{4Q_2^3}{4Q_2^2 - 1}.$$

All the values except for the inductance of the coils is now determined in order to calculate a system that operates at the bifurcation limit k_{min}.

There is multiple ways that the inductance of the coils could be determined. As stated earlier, a typical design-choice is to choose $Q_2 = 5$. Inserting this to Equation 3.31 provides a suitable value for the secondary coil. However, the design-rules created by Bosshard et al. [60] will instead be utilized to determine the inductance of the coils, and then compare the proposed values to the typical design-choice. The size of the coils can be decided by the equation for the power out represented by the relationship between the primary and the secondary voltage given as (eq. 4.28),

$$P_2 = \frac{8}{\pi^2}\frac{V_{dc,1}V_{dc,2}}{\omega_0 M_{min}}.$$

A perfectly balanced system is wanted as a reference-case. Rewriting Equation 4.28 for the inductances and inserting the conditions for a balanced system for the reference-case gives

$$L_1 = L_2 = \frac{8}{\pi^2}\frac{V_{dc,2}^2}{\omega_0 k_{min} P_2}. \tag{4.56}$$

Inserting the values for the respective parameters provides the optimal values for the coils,

$$L_1 = L_2 = 290.26\mu H \approx 290\mu H.$$

The design-rule for maximum transmission efficiency of a SS-compensation is actually just a rewrite of Equation 4.28 when the system is perfectly balanced. The design-rule is presented as:

$$L_2 = \frac{R_L}{\omega_0 k_{min}}. \tag{4.57}$$

Which off course gives the same inductance for the receiving coil

$$L_2 = 290.26\mu H \approx 290\mu H.$$

Following this design-rule ensures an optimal matching of the receiver coil to the equivalent load resistance R_L, in other words, a system that is operating at the bifurcation-limit [1]. These design-rules are discussed in detail and experimentally verified in [60]. The resulting quality-factor of the secondary coil can now be calculated as

$$Q_2 = \frac{\omega_0 L_2}{R_L} = 4.9955 \approx 5.$$

Which shows that the design-rule coincides with typical design-choices.

It would be possible to use the same approach to calculate the coil's inductances when the system is not ideal. However, it is as easy to design the system to operate at the bifurcation-limit at the ideal case, and then in case of loss, an unbalancing-factor x_u can be used in order to tune the phase angle of the total impedance in the circuit to be zero. This will be discussed further in subsection 4.5.3. What remains to calculate is the values of the corresponding capacitors that are to cancel out the reactive part created by the coils. They are simply calculated as

$$\begin{aligned} C_n &= \frac{1}{\omega_0^2 L_n}, \quad n = 1, 2, \\ C_n &\approx 218nF \quad n = 1, 2. \end{aligned} \tag{4.58}$$

If the system was to be implemented as a real system, it would be easiest to implement it with a 220 nF as they are to be found as standardized capacitors which are very cheap and accessible.

To summarize, the designed system that should be able to deliver 10 kW at 300 V nominal voltage has the following parameters:

Table 4.2: Parameters for which a design is to be built.

Parameter	Value
Nominal Power out (P_0)	10 kW
Nominal Voltage over battery (V_0)	300 V
Nominal frequency (f_0)	20 kHz
Minimal coupling (k_{min})	0.2
Calculated:	
Load resistance (R_L)	7.2951 Ω
Coils (L_1=L_2)	290 μH
Capacitors (C_1=C_2)	218 nF

In a practical implementation of the system, all coils will have some internal resistance which is defined by its quality factor as previously discussed. However, a typical mass-produced coil has a value of $Q = 100$ [72] and the Q-factors can be as high as above 1000 with careful design [73]. Since the coils are the most important part of a system used for inductive power transfer, it is of great interest to have coils with higher quality-factors than the ones that are mass-produced, hence $Q = 300$ is a reasonable reference-case which will be further used when resistance is included in the modelling. The resulting calculated frequency-response with and without loss is shown in Figure 4.12.

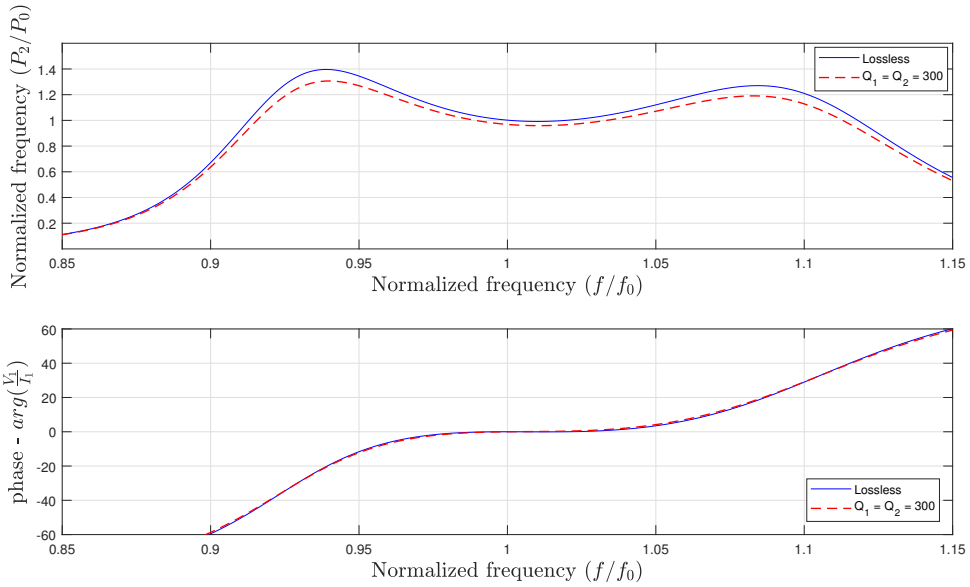

Figure 4.12: Normalized output power and phase-angle of the sending impedance for the designed system for a CR load.

From this figure, it can be seen that the power transferred to the battery drops ~ 1,5 % near the resonance frequency, while it drops ~ 6 % at the peak-value ($f/f_0 \approx= 0.94$) compared to the lossless case. The phase-angle however is not much affected, but with losses, the characteristics becomes slightly less bifurcated. This is because the left hand side of Equation 3.30 is more affected than the right side when the resistances in both coils are increased similarly. For a completely lossless system, the efficiency will be equal to one over the entire range of operation, while for Q=300, the maximum efficiency is given by Equation 4.43 and calculated to be $\eta_{max} = 0.967$. It will however be shown in section 4.8 that this does not yield over the entire range of operation.

Appendix B.1.1 shows the Simulink-diagram for simulation of inductive power transfer in the case of a constant resistance load. Since analysis of the inverter falls out of the scope of this thesis, it is instead chosen to use a square-wave generator at the input to the system. This makes it easy to adjust the frequency of the AC input wave. To verify the model, a script is made that utilizes a for-loop that simulates the model for each frequency over the wanted range. The power is measured using the *continuous power measurement*-block in the Simulink-library. This block utilizes Fourier analysis to calculate the active and reactive power. The phase angle is simply obtained by utilizing the relationship between the active, reactive and apparent power (fig. 3.2) outputted by the block. The script picks out the latest data-point of the simulation, before a new simulation is started. These values are then plotted on top of the calculated curve (Figure 4.12). It is important that each simulation runs long enough for the values to reach steady state before the data is extracted to *MATLABs* workspace. The model is verified for two cases, i.e., lossless and with $Q_1 = Q_2 = 300$. The characteristics of the calculated curves for the two cases are quite similar as shown. For brevity, it is therefore decided to only include the verification of the model when $Q = 300$ (Figure 4.13).

As seen from the figure, the simulated values (blue and red dots) are quite close to the calculated ones over the entire range. The reason for the deviation is the rectifier in the Simulink-diagram. The rectifier can simply be made ideal by setting the preferences related to the diodes in the *powergui* to

- Disable snubbers in switching devices
- Disable Ron resistances in switching devices
- Disable forward voltages in switching devices

When checking all these boxes, the simulation would not run because the interface between Simulink-signals and the powerlib becomes short-circuited. By trial and error, it is found that by disabling Ron resistances and decreasing the forward voltages and making the snubbers as ideal as possible, the rectifiers effect on the circuit becomes minimal. The more ideal the bridge is made, the slower the simulations runs, this trade-off will therefore need to be considered with respect to how important the accuracy is. However, it is observed that the phase-angle

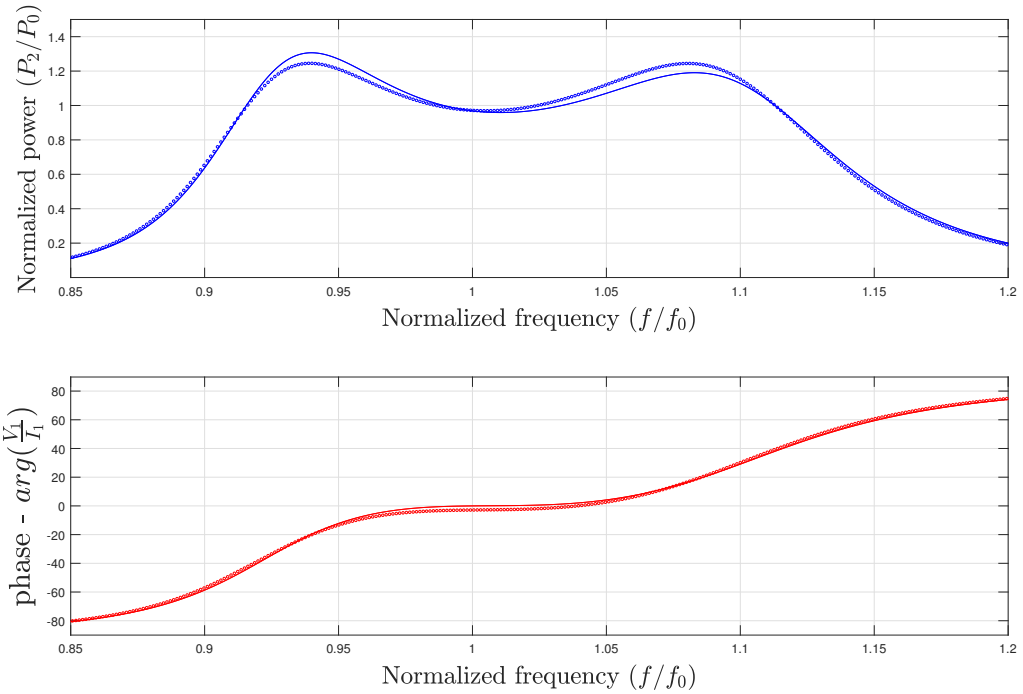

Figure 4.13: Verification of Simulink model with a CRL for coils with $Q_1 = Q_2 = 300$. k = 0.2. Each dot represents a simulation.

becomes slightly capacitive at the bifurcation-limit. Instead of having a rectifier in the model, the derived relationship for the resistance over the rectifier (Equation 4.7) can be used, and set the equivalent resistance in series with the coil. However, to verify the calculations, it is best to avoid making the same simplifications in the simulation-model, therefore it is decided to include the rectifier in the model.

4.5.3 Design - Constant voltage load

As previously stated, the simplification of having a constant resistance load to replace the battery is a good approximation close to the point where nominal power is achieved. However, when the point of operation is moving away from this, the effects of such a simplification becomes visible in the form of an error. In this section, a Simulink model will be created and verified with calculations, similarly to the CRL-case. The parameters of the system will be as listed in Table 4.2. But instead of having an equivalent load resistance R_L, a constant voltage DC-battery that outputs a constant nominal voltage will be placed on the DC-side of the rectifier. The response of the system when it is designed with a CVL, can be seen in Figure 4.14 where the black dashed lines represents the two limits of operation as given by Equation 4.22.

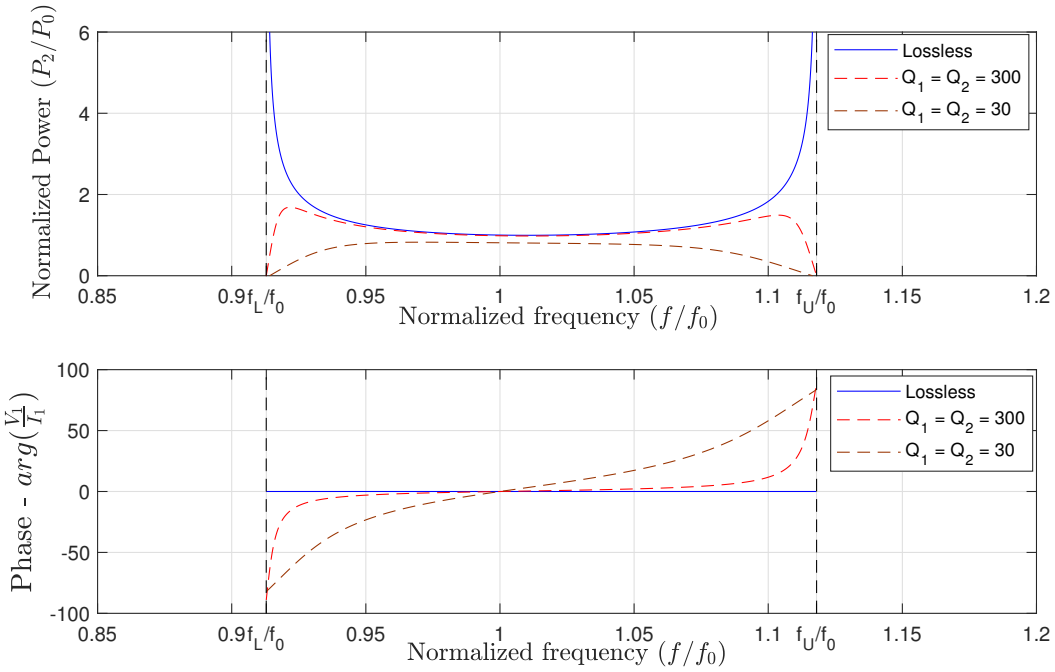

Figure 4.14: Normalized output power and phase-angle of the sending impedance for the designed system with a CV load.

The characteristics of both the output power and the phase of the total impedance (Z_t) are quite unique in case of a lossless system. It can be seen that the power ideally approaches infinity at both ends of the operation-range, while the phase of the total impedance remains zero over the whole range of operation. When loss is introduced however, the peaks closes in on values that are similar to the ones in case of a CRL, and the phase is also close to zero in a big part of the range of operation. The extreme case of $Q = 30$ highlights the fact that when increasing the resistance in both coils equally it will result in a less bifurcated system. This coincides with the inequality-condition related to bifurcation (Equation 3.30).

The reason for the big deviations is a result of the characteristics of the load-resistance in the two cases. Figure 4.15 shows the normalized value of the resistance in both cases over the range of operation. The value that the resistance is normalized with respect to is given by Equation 4.55.

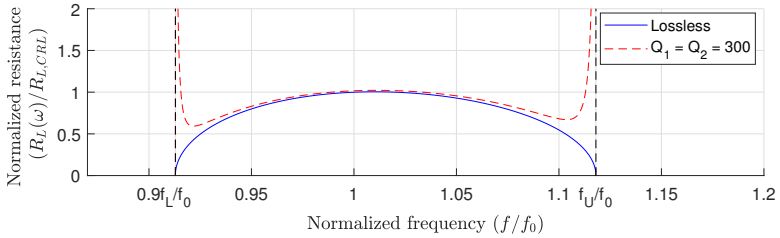

Figure 4.15: The values of the normalized load resistance $R_L(\omega)/R_{L,CRL}$ both for a lossless case and when $Q_1 = Q_2 = 300$. k=0.2.

As the figure shows, it is close to the limits of operation (ω_L and ω_U) that the differences becomes quite apparent. For the lossless case, the resistance approaches zero, resulting in the powerflow approaching infinity. The opposite is the case when including the losses in the coils. Another interesting observation from Figure 4.15 is that the resistance at the resonance-frequency is equal to the equivalent load resistance. This is a reason for why a CRL equivalent is a good approximation at and near the resonance-frequency for the minimal coupling k_{min}. Since the characteristics of the response is quite different between a system that is lossless and not, it is decided that the verification for both cases should be included in this thesis. The Simulink-model is quite similar to the one made for the CRL-case, and can be found in Appendix B.2.1. Figure 4.16 shows the verification of the Simulink-model for a lossless system, and Figure 4.17 shows the verification of the Simulink-model when $Q_1 = Q_2 = 300$.

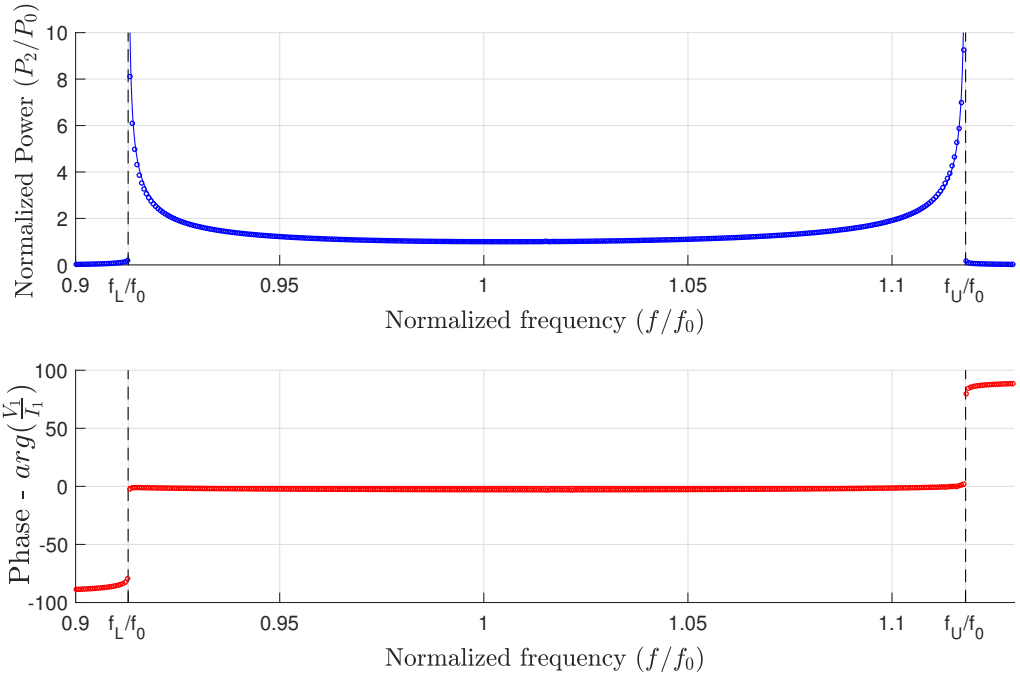

Figure 4.16: Verification of Simulink model for a CVL with lossless coils. k = 0.2. Each dot represents a simulation.

These figures shows that when having a lossless system, the system will in fact have power-peaks of up to eight times the nominal power out. This is in big contrast to the case with losses - having the maximum power output at approx. 1.6 times the nominal output power. It is also evident from the graphs that the Simulink-model coincides with the calculations. Again, because the rectifier is not 100% ideal, it causes the phase-angle of the total impedance to have a slightly capacitive characteristic over the range of operation. A way of tuning such characteristics is by introducing two tuning factors, namely the unbalancing factor x_u and the detuning-factor x_c. How these factors can affect the response of the system will be shown in the following sections.

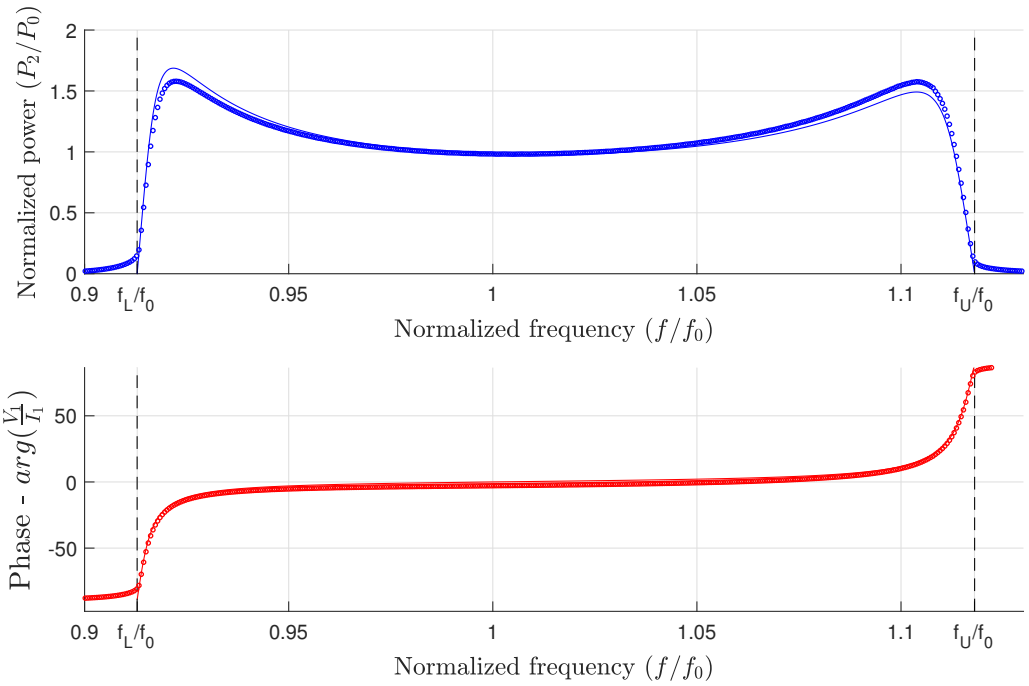

Figure 4.17: Verification of Simulink model for a CVL with coils with $Q_1 = Q_2 = 300$. k = 0.2. Each dot represents a simulation.

4.6 Introducing the unbalancing factor - x_u

This unbalancing-factor is an indication of how far away the system is deviating from the design-rule to obtain a balanced system (Equation 4.53). The unbalancing-factor is given as

$$x_u^2 = \frac{L_1}{L_2}\left(\frac{V_2}{V_1}\right)^2. \tag{4.59}$$

The equation for the equivalent constant voltage load resistance as a function of x_u is found in [1] and will in this thesis be recreated, as it is of great advantage to understand how the response of the circuit can be tuned in order to remain a balanced system under different resistances.

Maple was again of great help to do the initial simplification of the expression. The result can be found in Appendix A.2, but the last part is done by hand and recreated here to show the elegance of the simplification. In Maple, expressing the resistance in terms of the interesting properties k and ω_0 is performed. This gives the expression for the resistance in terms of a lossless system as,

$$R_L = \frac{V_2\sqrt{L_1}\left|(k^2-1)\omega^4 + 2\omega^2\omega_0^2 - \omega_0^4\right| L_2}{\sqrt{-V_2^2(\omega-\omega_0)^2(\omega+\omega_0)^2 L_1 + L_2 V_1^2 k^2\omega^4\omega}}. \tag{4.60}$$

By simply dividing Equation 4.60 by V_2 and $\sqrt{L_1}$ the expression simplifies to

$$R_L = \frac{\left|(k^2-1)\omega^4 + 2\omega^2\omega_0^2 - \omega_0^4\right| L_2}{\sqrt{-(\omega-\omega_0)^2(\omega+\omega_0)^2 + \frac{L_2 V_1}{L_1 V_2^2}^2 k^2\omega^4\omega}}. \tag{4.61}$$

From this, it can be seen that the expression for the unbalancing-factor appears in the expression. Even though this is a design rule the system is to be designed upon, V_1 is a parameter that it is possible to adjust in an implemented system under the assumption that the voltage-supply has a higher possible capacity than what is used in the design. L_2,L_1 and V_2 will on the other hand remain constants in a real life system based on our assumptions. The factorized expression in the denominator that contains information about the operating frequency and the resonance frequency can be rewritten as

$$-(\omega-\omega_0)^2(\omega+\omega_0)^2 = -\omega_0^4 + 2\omega^2\omega_0^2 - \omega^4.$$

The absolute-sign in the nominator can also be removed because it will always be positive and real as a result of our assumptions. Inserting the expanded expression and x_u into Equation 4.61 gives the following equation:

$$R_L = \frac{L_2(\omega^4(k^2-1) + 2\omega^2\omega_0^2 - \omega_0^4)}{\sqrt{-\omega_0^4 + 2\omega^2\omega_0^2 - \omega^4 + \frac{k^2}{x_u^2}\omega^4\omega}}.$$

Finally, to get rid of the high degree of the polynomials, this whole equation is to be divided with ω^2. Resulting in an equation at the exact same form as the one obtained in [1] given as,

$$R_L(\omega, x_u) = \frac{L_2(\omega^2(k^2-1) + 2\omega_0^2 - \frac{\omega_0^4}{\omega^2})}{\sqrt{\omega^2\left(\frac{k^2}{x_u^2} - 1\right) + 2\omega_0^2 - \frac{\omega_0^4}{\omega^2}}}. \tag{4.62}$$

Inserting the conditions for a perfectly balanced system that operates at the resonance-frequency, yields [1]

$$R_L\big|_{\omega=\omega_0, x_u=1} = \omega_0 \cdot k \cdot L_2, \tag{4.63}$$

which coincides with the optimal load-matching for a perfectly balanced load-resistance for CR-loaded systems with no loss as given by Equation 4.46.

The range of operation in case of a CVL is again decided by the inequality given by the condition that the term under the square-root in the denominator needs to be greater than zero for the equivalent resistance to be a real value. Solving this inequality in a similar matter as was done for Equation 4.22 gives a tidier expression for the range of operations. But in order to show the connection between the expression found for the range of operation as given by Equation 4.22, it is chosen to show how this expression can be rewritten in terms of x_u and k. Doing this will also show why the common rewrites as discussed earlier often is used in literature in order to write some parameters in terms of others. ω_L was earlier found as

$$\omega_L = \sqrt{\frac{V_2}{C_1(L_1V_2 + MV_1)}}. \tag{4.64}$$

Since it is wanted to express ω_L in terms of k and x_u, M and C_1 needs to be rewritten. To do this, two of the most common rewrites can be utilized (eq. 4.10 and eq. 4.11) as previously discussed, and thereby obtain

$$\begin{aligned}
\omega_L &= \sqrt{\frac{V_2}{\frac{1}{L_1\omega_0^2}(L_1V_2 + k\sqrt{L_1L_2}V_1}}, \\
&= \sqrt{\frac{V_2\omega_0^2}{V_2 + \frac{k}{L_1}\sqrt{L_1L_2}V_1}}, \\
&= \sqrt{\frac{\omega_0^2}{1 + k\sqrt{\frac{L_2}{L_1}}\frac{V_1}{V_2}}},
\end{aligned}$$

Finally, by inserting the expression for x_u, ω_L expressed as x_u and k is obtained as,

$$\omega_L = \omega_0 \cdot \sqrt{\frac{1}{1 + k/x_u}}. \tag{4.65}$$

The same procedure yields for ω_U and thereby, the operation range can now be written as

$$\begin{aligned} \omega_0 \cdot \sqrt{\frac{1}{1 + k/x_u}} \leq &\omega \leq \omega_0 \cdot \sqrt{\frac{1}{1 - k/x_u}}, \\ \omega_L \leq &\omega \leq \omega_U. \end{aligned} \tag{4.66}$$

Which is the same as the one obtained in [1] where they solved the resulting inequality in the denominator of Equation 4.62 based on the criterion to the resistance. How x_u affects the operating-range is fairly easy to see from Equation 4.66. When $x_u < 1$, k/x_u increases, as a result ω_L will be smaller and ω_U will be larger and thus, the range of operation increases. The opposite is the case when $x_u > 1$. Figure 4.18 shows the response for different unbalancing-factors on the system with losses. Since introducing resistance to the system yield a less bifurcated characteristic for a SS-compensated circuit, an unbalancing-factor of $x_u = 0.95$ puts the system back to the bifurcation limit. In addition, it is observed that the reasoning behind how the operation-range is affected by changing x_u is consistent with the results that Figure 4.18 shows.

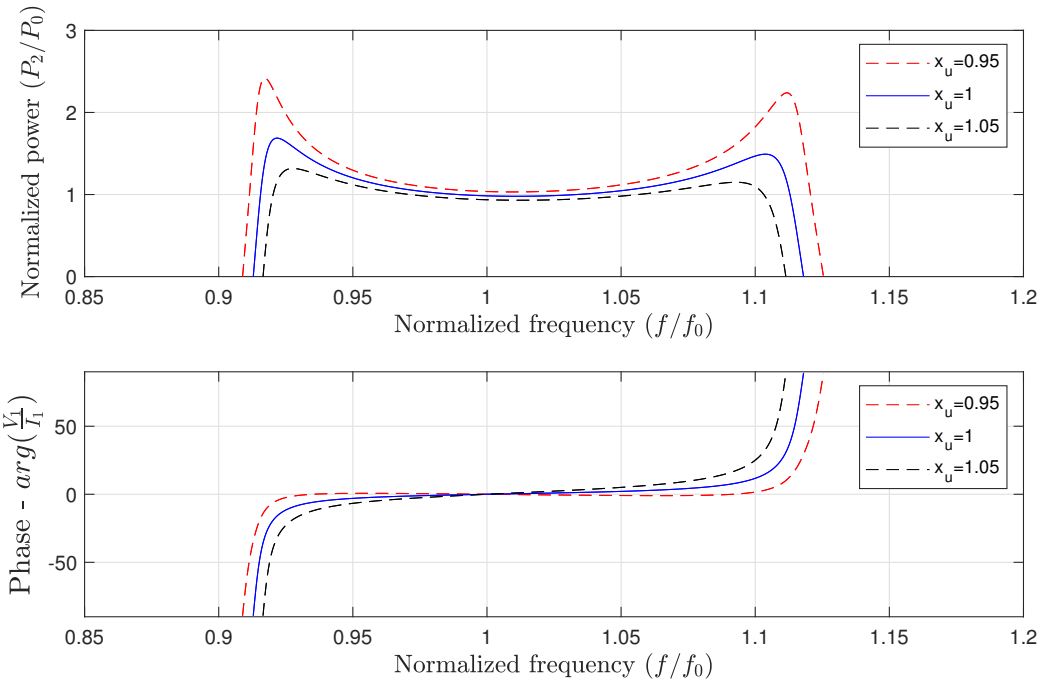

Figure 4.18: The effects of different unbalancing-values (x_u) when $k = k_{min} = 0.2$ and $Q_1 = Q_2 = 300$.

Looking back at the extreme-case where the coils quality is one tenth (Q=30) of what is chosen for our reference case, it is found that an unbalancing of $x_u \approx 0.7$ would be needed in order to have the system to operate at the bifurcation-limit. However, it is recommended to keep the unbalance within 10-20 % in order to avoid a drop in efficiency [1]. Additionally, if the voltage-source V_1 is the variable that is affected by the unbalancing, its value would increase with an inverse variation to x_u as given by Equation 4.59, resulting in too much power delivered to the battery as a result of Equation 4.28. For this reason, it would instead be recommended to redesign the system, instead of forcing it back to the bifurcation-limit by using the unbalancing-factor.

4.7 Introducing the detuning-factor - x_c

Another factor that can be used to tune the response is the detuning-factor x_c. As discussed in subsection 3.2.2, it is possible to design a system to have different resonance-frequencies in the primary and the secondary circuit. This is often done to meet system requirements and it can also lead to a higher system efficiency [55] because of reduced loss over the inverter. The value of the capacitive detuning factor gives an indication of how detuned the capacitors in the system are, and is given by,

$$x_c = \frac{C_1}{C_2} \cdot \frac{L_1}{L_2}. \tag{4.67}$$

When $x_c = 1$, the system is designed to eliminate all reactance in both the primary and the secondary circuit at the resonance frequency. The major part of the literature on resonant inductive power transfer designs their systems to this value. If $x_c \neq 1$, the size of the capacitors is not matched with the inductors. This results in the capacitors not being able to cancel out, or cancelling out more than the reactance of the coil. Thereby, the system is deliberately tuned away from a unity power factor (pf). Equation 4.67 can be rewritten as a tuning-factor related to the value of the primary compensating capacitor (C_1) as

$$C_1 = x_c \cdot C_2 \frac{L_2}{L_1}. \tag{4.68}$$

Recalling that the equation from which the resonance-frequency is defined

$$j\omega_0 L - \frac{j}{\omega_0 C} = 0.$$

It can be seen that if $x_c < 1$ it will result in a smaller C_1, and thereby the cancelling capacitance of the capacitor is bigger than the inductance of the coil. This will result in a slightly capacitive characteristic of the circuits total impedance, Z_t, over the total range of operation. An inductive characteristic is the case when $x_c > 1$. Figure 4.19 shows the effects of the detuning-factor x_c for the reference-case when $Q_1 = Q_2 = 300$.

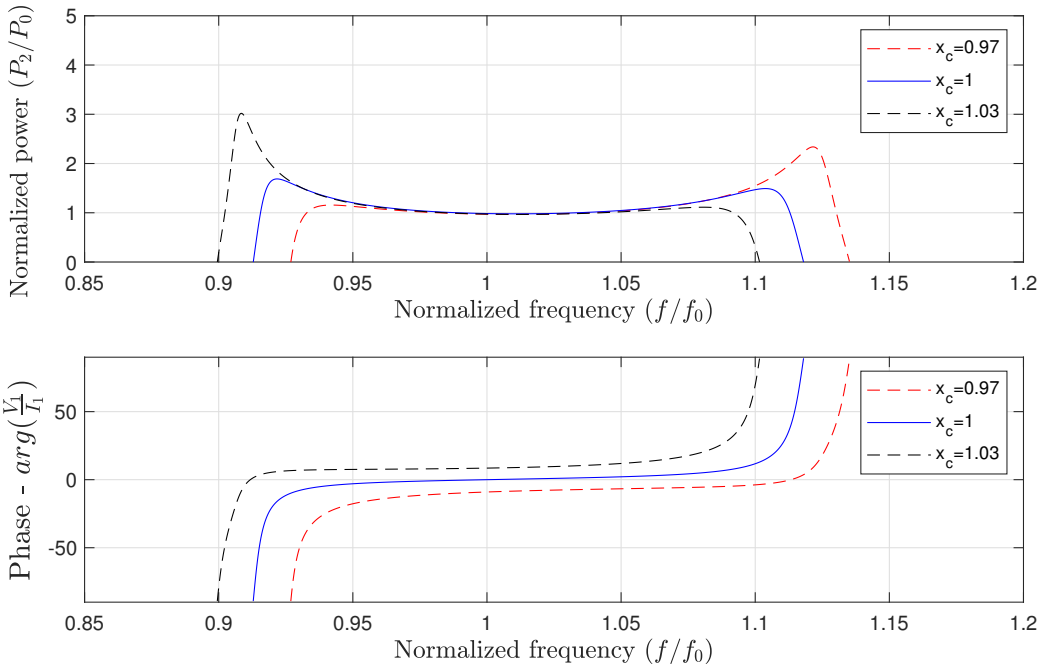

Figure 4.19: The effects of different detuning-factors (x_c) when $k = k_{min} = 0.2$ and $Q_1 = Q_2 = 300$.

From the figure it can be seen that the reasoning behind the detuning-factors effect on the total impedances phase angle coincides with the plots. In addition, $x_c > 1$ increases the range of operation in the subresonant region $\omega_L < \omega < \omega_0$, while creating a power-peak near the lower limit frequency. The same yields for x_c in the superresonant operation $\omega_0 < \omega < \omega_U$. This property enables frequency-control of output power over a bigger range of coupling-coefficients, as will be discussed in chapter 5. In addition, according to [1], designing the circuit with $x_c > 1$ is wanted, as it leads to ZVS with minimum turn-off current for all H-bridge switches during square-wave operation, which in turn results in very low switching losses over the whole range of operation.

To summarize, it has been shown that the unbalance-factor x_u can be used in order to tune a systems bifurcation-properties, while the detuning factor, x_c, can be used to control the phase-angle of the total impedance - and to create power-peaks near the limits of operation. This knowledge can be used in order to tune the reference-case CVL-system when the coils quality-factors are $Q_1 = Q_2 = 300$. First of all, it was shown from Figure 4.18 that an unbalancing-factor

of $x_u = 0.95$ will put the system back to the bifurcation-limit. In addition, taking into account the recommendation regarding the benefit of having a slightly inductive characteristic over the entire range of operation [1], $x_c = 1.03$ is suitable. The resulting response of the tuned system can be seen in Figure 4.20.

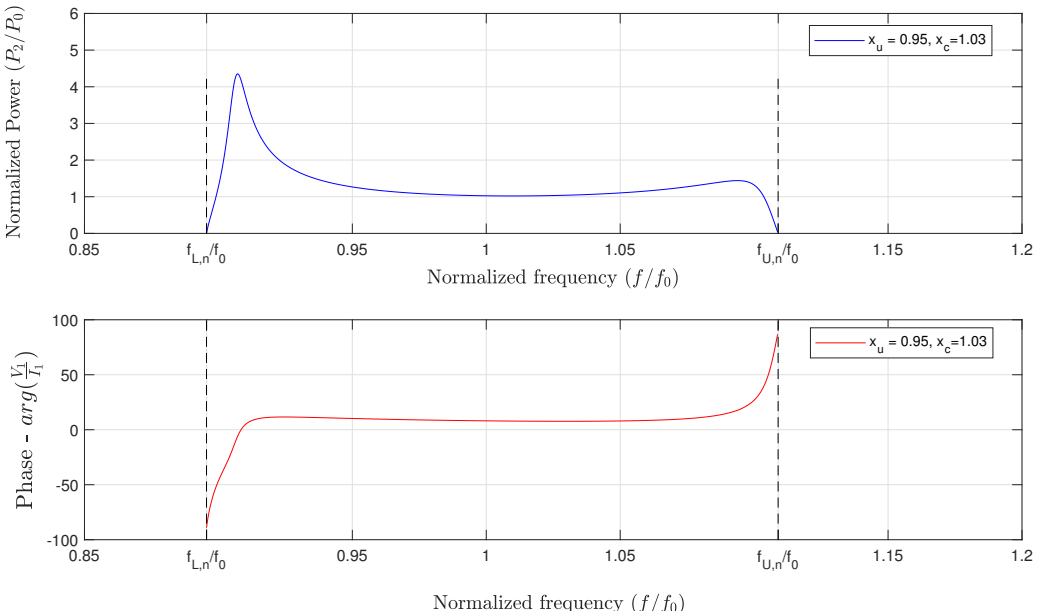

Figure 4.20: The resulting IPT-response after tuning of the reference-case by setting $x_c = 1.03$ and $x_u = 0.95$.

With these values to the tuning-parameters, the system is actually a little bit past the limit of bifurcation. The resulting power-output is however of such a characteristic that it enables control of the output power over a wider range of magnetic coupling coefficients. Since the control that is to be implemented later only concerns about remaining the output-power without relying on some kind of phase-tracking to remain a constant phase-angle, operating a bit past the limit of bifurcation will be accepted. However, Figure 4.20, shows that the unbalancing of $x_u = 0.95$ results in the powerflow becoming $P_2 > P_0$, $\forall \omega$ when $k = k_{min}$. This means that the system cannot obtain the nominal power output by adjusting the frequency of operation. This happens because the perfectly tuned system is designed to have exactly P_0 as output-power at the resonance-frequency for k_{min}. When unbalancing is introduced, V_1 increases as a result, hence the power out also increases. To cope with this problem, it is decided to increase the inductance of the coils (eq. 4.28). The new parameters and variables of the tuned system that is to be controlled is finally summarized in Table 4.3.

Table 4.3: Parameters for the tuned system that is to be controlled.

Parameter	Value
Nominal Power out (P_0)	10 kW
Nominal Voltage over battery (V_0)	300 V
Nominal frequency (f_0)	20 kHz
Minimal coupling (k_{min})	0.2
Calculated:	
Unbalance factor (x_u)	0.95
Detuning factor (x_c)	1.03
Voltage in (V_dc, 1)	315.79 V
Coils (L_1=L_2)	310 μH
Primary cancelling capacitor (C_1)	210.4 nF
Secondary cancelling capacitor (C_2)	204.28 nF

The only difference in the response when increasing the values of both coils is that the resulting power-flow will be a little lower over the entire range of operation. The bifurcation-characteristics is not affected. This can be seen from Figure 4.21.

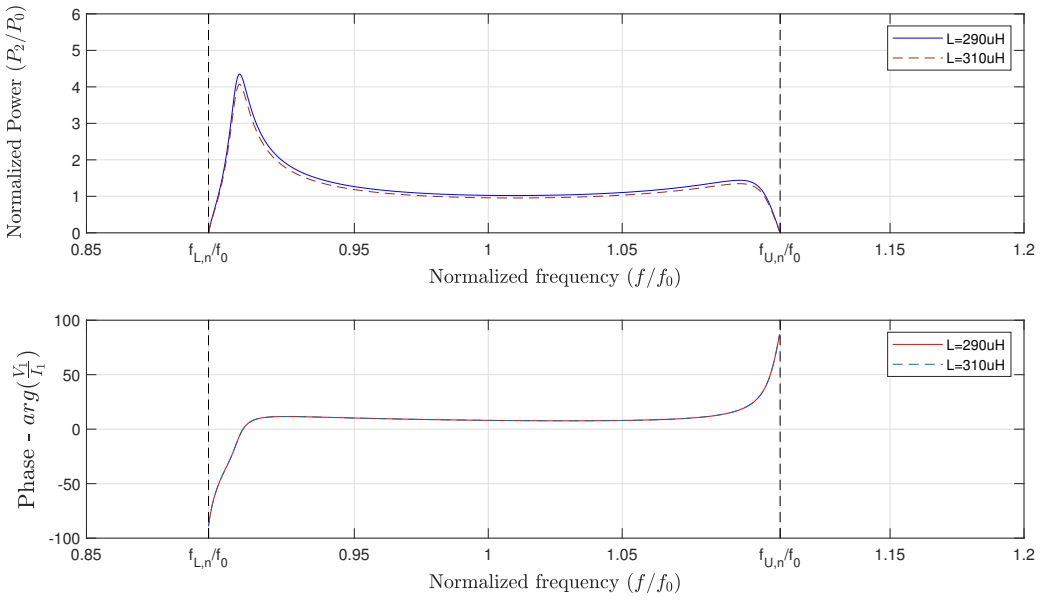

Figure 4.21: Comparison of the response with two different inductors after tuning the reference-case by setting $x_c = 1.03$ and $x_u = 0.95$.

In the next section, it will be shown why it is important to model the system with a CVL in order to control the power output by regulating the frequency of operation.

4.8 Comparing the two different ways of analyzing the circuit

The differences in the two ways of analyzing the circuit is best shown by comparing the unbalanced reference case as given by Table 4.2 for both cases with and without loss. Figure 4.22 shows the resulting response in these cases.

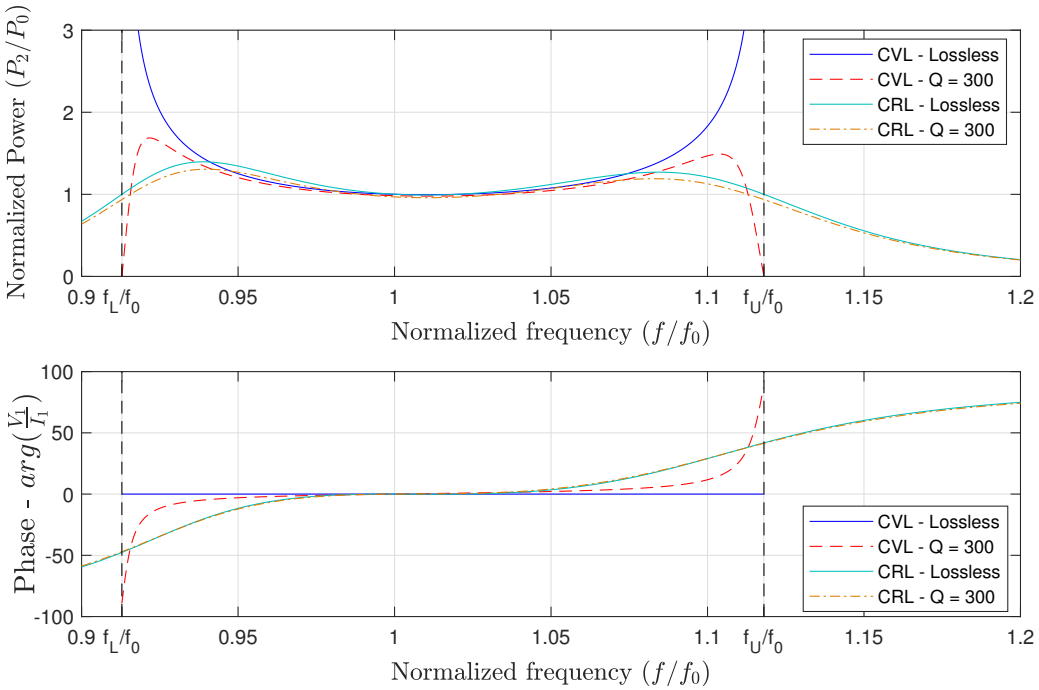

Figure 4.22: Response-comparison between a CRL and a CVL that are designed for the reference-case ($k = 0.2, x_u = x_c = 1$).

As expected, the CR-equivalent is an accurate approximation of the steady-state characteristics at and near the resonance-frequency for the nominal coupling, independent of losses. For this reason, a CR-load equivalent is valid for many cases. However, the differences in frequency characteristics becomes quite apparent when considering off-resonant operation. Firstly, it has to be pointed out that the biggest difference is observed between a CVL and a CRL in case of lossless coils, where the power-flow is bounded for all frequencies for a CRL, while moving towards infinity when approaching the limits of operation for a CVL as given by Equation 4.66. In addition, the CR equivalent does not give an indication of the fact that operation outside the range of operation will result in zero power flow. The reason for this is the linear relationship

between the current and the voltage when the load is a CR. This means that a reduced current gives a reduced voltage. It will therefore always be a difference in voltage-potential, resulting in powerflow. Since the voltage over the battery is constant for a CVL, a frequency too far away from the resonance frequency will result in a discontinuous conduction mode when the induced voltage becomes lower than the CVL. This will in turn result in zero power flow. Moreover, the phase-angle of the total impedance is not near the characteristics of unity power factor for a CRL as it is for a CVL. It is however clear that the characteristics of the system with a CVL is severely affected when loss is introduced to the system. The system will however have a bigger range of operation with unity power factor than for a CRL. In terms of control, the most important difference is the two power-peaks near the limits of operation, especially the peak in the subresonant region, based on the recommendation of keeping $x_c > 1$. As shown in subsection 4.3.3, the power out will decrease when the magnetic coupling increases. The peak in the subresonant region can be used to remain the wanted power output for a higher coupling by reducing the frequency of operation. The higher the quality of the coils, the larger the range of coupling coefficients where power can be controlled by changing the frequency. The range of coupling-coefficients for which it is wanted to control the output power needs to be set. The system is designed to deliver 10 kW at $k_{min} = 0.2$. The better the coupling, the harder it is to maintain the wanted power out, because the frequency will then approach the limit of operation. For this reason, a maximum coupling coefficient is set to $k_{max} = 0.8 = 4 \cdot k_{min}$ which is a very high magnetic coupling for materials with a low permeance. A variable including all the coupling coefficients $k_{range} \in [k_{min}, k_{max}]$ can then be defined. A describing way of showing why it is important to model the system as a constant voltage load is by creating a 3D plot that shows the IPT-characteristics over the range of coupling coefficients (k_{range}) for both systems. The system-parameters is given by the values in Table 4.3. Figure 4.23 shows the response for a CRL and Figure 4.24 shows the response for a CVL.

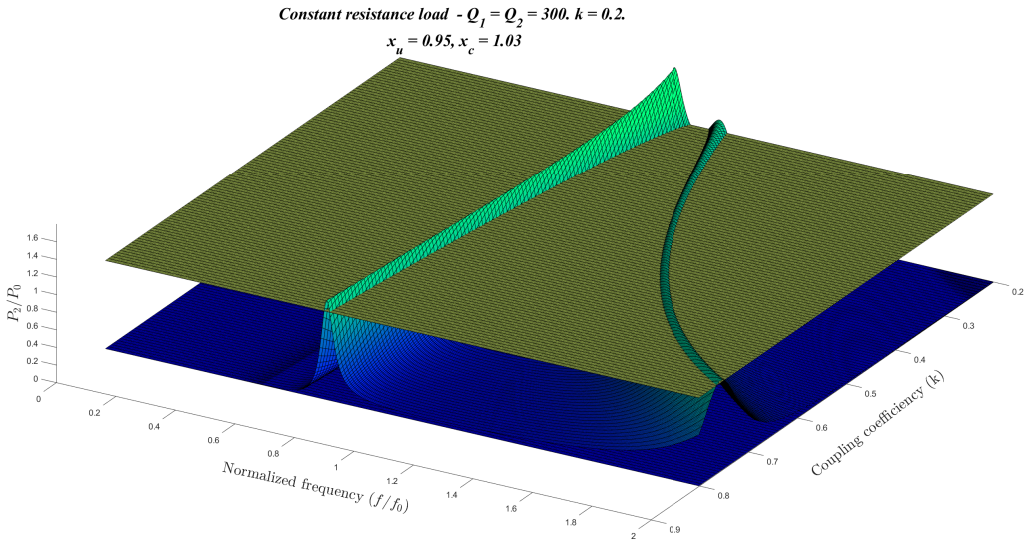

Figure 4.23: The normalized output power for the tuned reference case as a function of both frequency and coupling coefficiency with a CRL. The bottom horizontal plane represents $P_2/P_0 = 0$, and the top horizontal plane shows $P_2/P_0 = 1$.

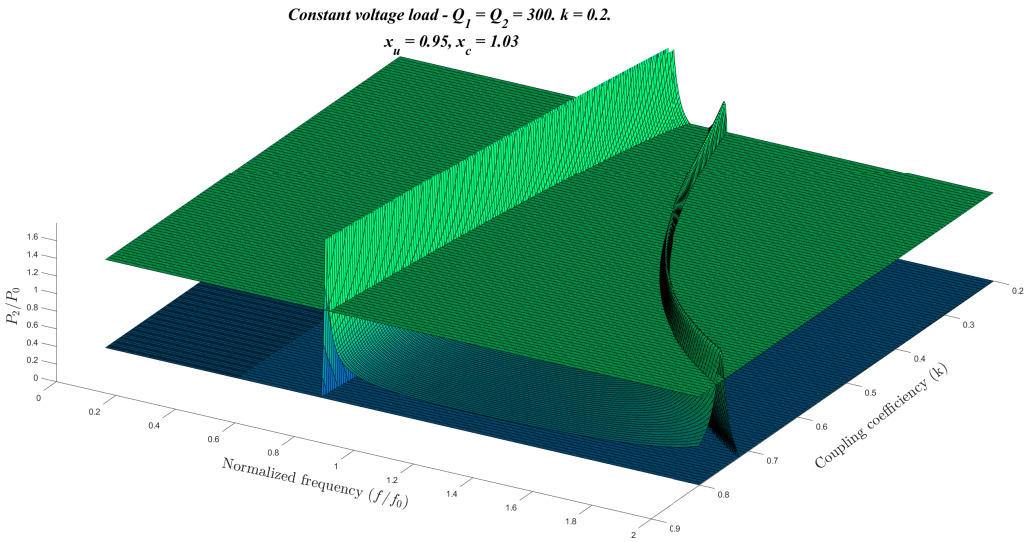

Figure 4.24: The normalized output power for the tuned reference case as a function of both frequency and coupling coefficiency with a CVL. The bottom horizontal plane represents $P_2/P_0 = 0$, and the top horizontal plane shows $P_2/P_0 = 1$.

As seen from the figures, it should in theory be possible to control the output power for both systems over the entire range of coupling coefficients. However, the peak in the subresonant part is $P_2/P_0 > 2$ over the entire range for a CVL, while the highest peak at minimum coupling is $P_2/P_0 \approx 1.61$ for the CRL. A controller that is too aggressive with a reference $P_2 = P_0$ is then more likely to overshoot in case of a CRL, resulting in the operating frequency moving past the limit of operation which results in zero power flow. In case of a CVL, a small change in

frequency near the lower limit of operation ω_L will result in a big change in the power out. It is therefore more likely that the controller will be able to stop decreasing the frequency before exceeding the limit of operation. Another major difference between the two ways of analyzing the circuit is the characteristics of the phase-angle of the total impedance. This matter has been discussed earlier and the comparison is shown in Figure 4.22 for the reference-case. However, it is of great interest to see an indication of how the phase-angle is affected for other coupling coefficients in the range. The differences starts to emerge for small changes in the coupling. Therefore it is decided to plot the frequency characteristics for k=0.2 and k=0.5.

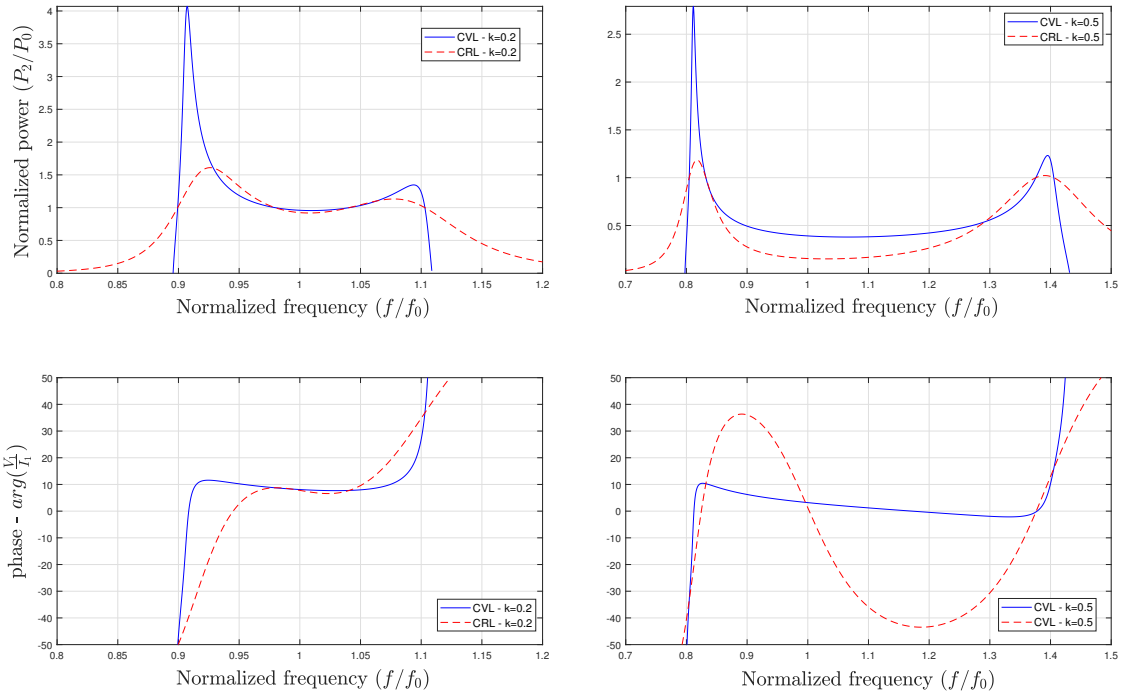

Figure 4.25: Comparison of the phase-angle of the total impedance for a CVL and a CRL at k=0.2 and k=0.5.

Even though the phase-angle at the wanted point of operation, i.e., $P_2 = P_0$, coincides at different coupling coefficients for both types of load, it is clear that the phase-angle for the CR-equivalent is not a valid representation for a CVL over the entire range of operation. In addition it can be seen that the amount of power transferred is the same for both types of loads at the resonance-frequency for a nominal magnetic coupling k_0. This was also shown in Figure 4.22. When the coupling increases however, the power out is reportedly lower for a CRL-equivalent. This comes from the linear relationship that is between the voltage and the current in case of a CRL which will be further discussed in section 5.4. This property would have consequences if the system was to be controlled by adjusting V_1 instead of ω to ensure a nominal power output at the resonance frequency for all couplings. Since the output is to be regulated with

respect to frequency, it is also interesting to see the efficiency-characteristics over the range of operation. The efficiency of a perfectly balanced system with the same resonant frequency on both sides of the circuit has a maximum at the resonance-frequency, and is decided by the size of the $FOM = k \cdot Q$ (eq. 4.43). As a result, the major part of literature on this subject assumes operation at the resonance-frequency before deriving the expressions. Others find that the optimal inductive part of the circuit is zero by differentiating the expression for efficiency with respect to the reactance (X) of the total impedance (eq. 4.13), and some simply evaluates only the real parts of the circuit [4, 67–69, 74]. Obtaining an expression for the efficiency without making these assumptions will not yield a tidy result that is of interest to include in this thesis. However, it is fairly easy to plot the efficiency by inserting the values for the system as given by Table 4.3 into the definition of the efficiency of a system into *MATLAB* and plotting it over the range of interest. The resulting plots is again verified with the Simulink-models simply by dividing the output power with the input power. The result can be seen in Figure 4.26

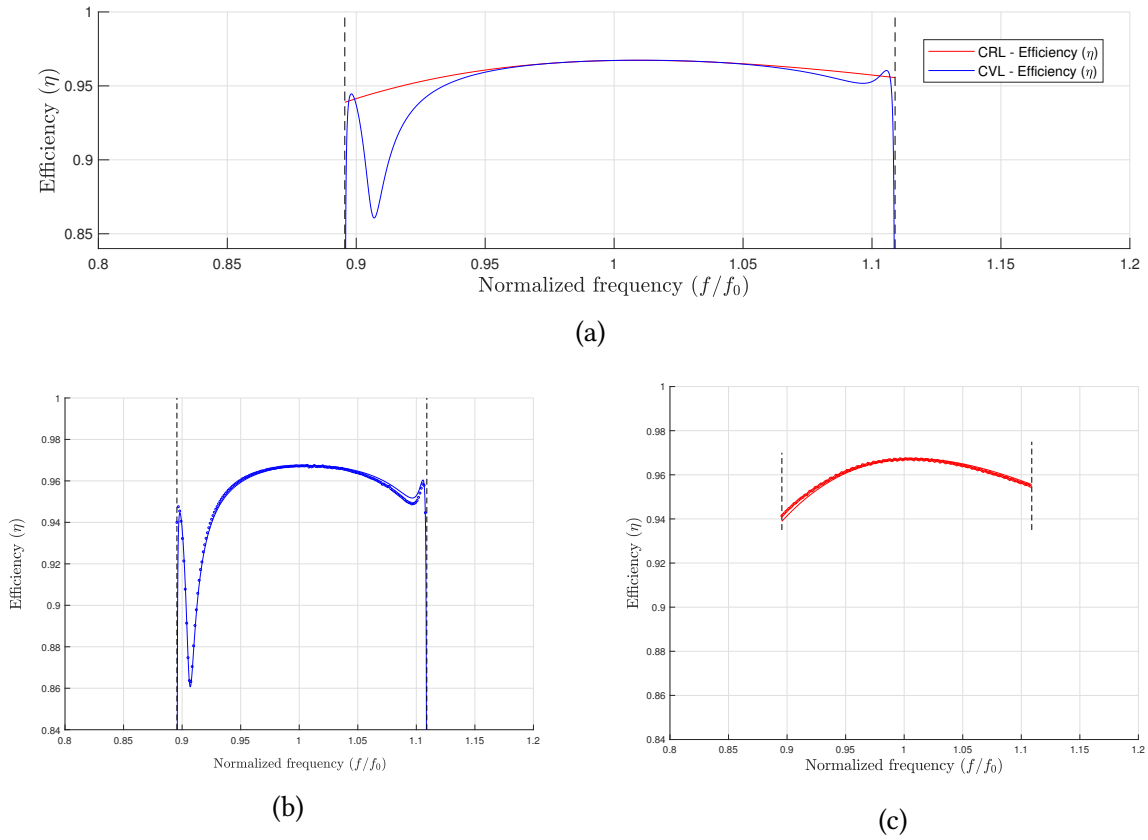

Figure 4.26: Comparison between the efficiency of a CVL and a CRL over the range of operation. (b) Verification of CVL using the Simulink-model. (c) Verification of CRL using the Simulink-model.

This figure shows that there is not a difference between a CRL and a CVL in terms of efficiency for frequencies near the resonance frequency (ω_0) when $k = k_0$. It is when the operating frequency closes in on the limits of operations the differences becomes apparent. It is

found that the dip in the efficiency correlates with the point of maximum power transfer. Since the system is designed with a detuning-factor that ensures a power-peak near the lower limit of operation (ω_L), it will similarly result in a dip in the efficiency at the same frequency. The dip in the efficiency is not significant at the upper limit of operation (ω_U) as a result of the design. However, an unbalancing-factor $x_c < 1$ will result in a power-peak in the superresonant-region, and thereby, the efficiency will instead have a dip near the upper limit of operation (ω_U). It is also found that the magnitude of the peak in power correlates with the corresponding drop in magnitude of the efficiency. However, as can be seen from Figure 4.24, the power out will be equal to the nominal output power before reaching the point of maximum power transfer for all coupling coefficients within k_{range}. Therefore, the drop in efficiency are not of concern for the power-control of the system. Figure 4.27 provides an overview of the total impedances phase angle and the efficiency at the resulting points of operation where $P_2 = P_0$ for four coupling coefficients that together spans the range of coupling coefficients (k_{range}).

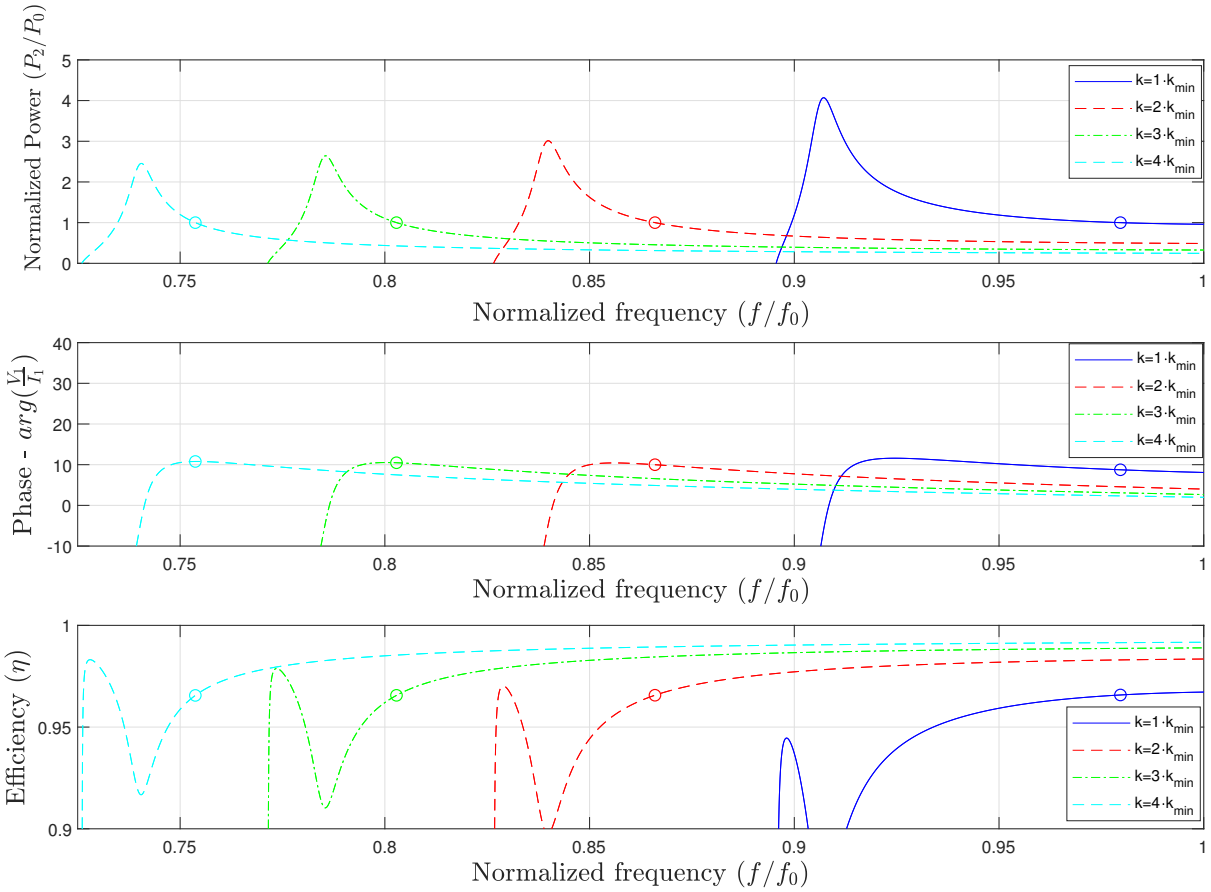

Figure 4.27: The value of the normalized power, the phase and the efficiency at the point of operation (marked by a dot) for all four coupling coefficients that together spans the range k_{range}.

The maximum efficiency for the minimum coupling is given by Equation 4.43 and can

be calculated as $\eta_{max} = 0.967$. An interesting observation is that the efficiency for the other coupling coefficients in the range k_{range}, also has an efficiency of $\approx \eta_{max,k_{min}} = 0.967$ at the point where $P_2 = P_0$. This property will be utilized later to achieve control without feedback. In addition, the phase-angle is also slightly inductive at the shown points of operations, as recommended in order to reduce switching-losses in the converter in [1].

Chapter 5

Frequency control of the inductive charger

This chapter aims to show how controlling the output power of an inductive charger can fairly easily be obtained by using a simple controller. In this entire section, the tuned system with the values given in Table 4.3 will be used. The reason why it is highly relevant to control the output power with respect to coupling coefficients is because of the rough dynamics that the AUV can face during charging. This is in contrast to, e.g., a static inductive charging of an EV with a fixed length between the floor and the underside of the car where the coupling coefficient will remain the same throughout the charging. There is mainly three different types of disturbances that the AUV is likely to face as discussed in section 3.4, these are:

1. Step response - A sudden change in the position - Due to collisions
2. Ramp response - A steady change in position - Due to current
3. Sinusoidal disturbance - Constantly changing - Due to waves (Very shallow charging)

To understand what range of physical distance the coupling coefficients represents, the extensive work done in literature on this matter will be utilized. Since the difference in permeability is small between air and seawater, and it is shown in [50] that there is a non-significant difference in mutual inductance between seawater and air for relatively small frequencies (f<100kHz), the work done in [75] and [76] can be utilized. Planar coils are very often used for IPT-applications. These planar coils find different shapes, e.g. hexagonal, rectangular, octagonal and circular. Details of which shapes that suits what purpose will not be presented, but for this example, a circular coil will be chosen as it is the most common shape of planar coils. Defining the physical size of a circular planar coil with a value of $310\mu H$ can be done by using [75],

$$L = \frac{n^2 \mu d_{avg} c_1}{2}(ln(c_2/\rho) + c_3\rho + c_1\rho^2), \tag{5.1}$$

the constants c_1, c_2, c_3 and c_4 are geometry-related constants, while ρ represents how hollow the inductor is. A small ρ represent a hollow inductor, i.e., the outer diameter is almost equal to the inner diameter ($d_{out} \approx d_{in}$). If ρ is big, it represents a full inductor, i.e., $d_{out} >> d_{in}$ as given

by,

$$\rho = \frac{d_{out} - d_{in}}{d_{out} + d_{in}}. \tag{5.2}$$

The average diameter, d_{avg}, is given by,

$$d_{avg} = \frac{1}{2} \cdot (d_{out} + d_{in}). \tag{5.3}$$

For this equation to be accurate, the relationship regarding the space between each wire and the thickness of the wires (s/w) should ideally be kept low. Typical spiral inductors are built with s ≤ w. The reason is that a smaller spacing improves the magnetic coupling and reduces the area of the spiral. A large spacing is only wanted in order to reduce the interwinding capacitance. In practice, this is however not a concern [75]. Choosing a coil with inner diameter $d_{in} = 20mm$ and an outer diameter of $d_{out} = 24cm$ with n=56 turns, gives a spiral coil with an inductance of $L = 310\mu H$ according to Equation 5.1. By using a wire gauge of 18 which corresponds to a width w=1.024 mm, the relationship $s/w \approx 1$. The relationship between the coils dimensions and the coupling coefficient between them can be found as [76],

$$k = \frac{1}{\left[1 + 2^{2/3}(d/\sqrt{r_1 r_2})^2\right]^{3/2}}. \tag{5.4}$$

For distances that approach the radius of the coils. The expected normalized coupling (k/k_0) with respect to a distance (d), can then be plotted as

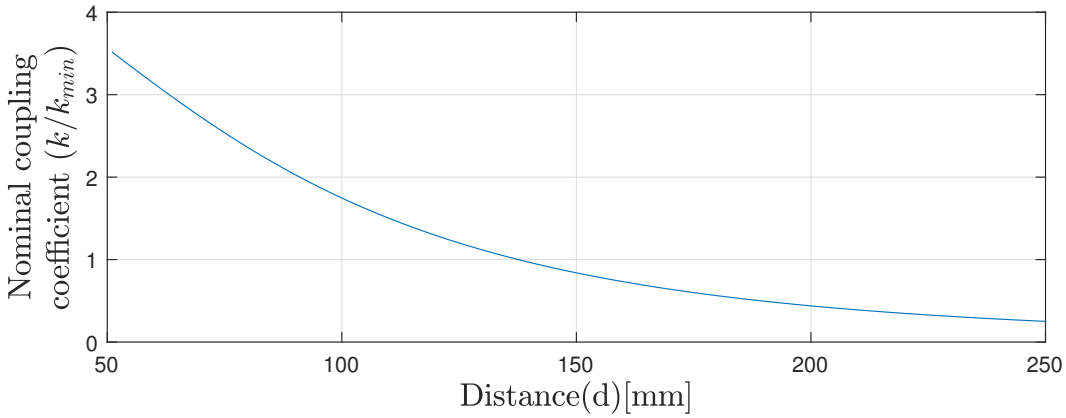

Figure 5.1: Expected relationship between magnetic coupling and distance between two identical planar coils with inductance L = 310 μH. $k_{min} = 0.2$.

Because of the simplifications done in [75] and [76], it is not expected that this graph is

an exact representation of a real life response. However, it gives a clue of which range of distances that are relevant. For an implemented system, it would be easy to verify this graph by measuring the mutual inductance between the coils at a range of distances, and using the formula that denotes the relationship between k and M (eq. 3.18). But is is recommended to first perform a FEM-analysis of the coupling.

The dynamic response of a controller that is able to remain the nominal power output for a change in position that corresponds to the scenarios listed in the start of this chapter will be presented later. But first, the logic behind the controller needs to be shown. Up until now, the system has been designed to have a power-peak in the subresonant region. Figure 4.9 shows how the output-power decreases when the coupling increases. Figure 4.27 gives an idea of how the power increases when decreasing the frequency. By setting a reference-value $P_{ref} = P_0$, the following relationship can be denoted:

$$
\begin{aligned}
&e_P = P_{ref} - P_2, \\
&e_P > 0 \ \text{ if } \ P_{ref} > P_2, \\
&e_P < 0 \ \text{ if } \ P_{ref} < P_2, \\
&e_p = 0 \ \text{ if } \ P_{ref} = P_2.
\end{aligned}
$$

From this, it is clear that if $e_p > 0$, the frequency needs to be decreased, while if $e_p < 0$, the frequency needs to be increased. This simple relationship enables the use of a PI-controller to regulate the frequency over the range k_{range} to output the wanted power P_0. The resulting controller is shown in Figure 5.2

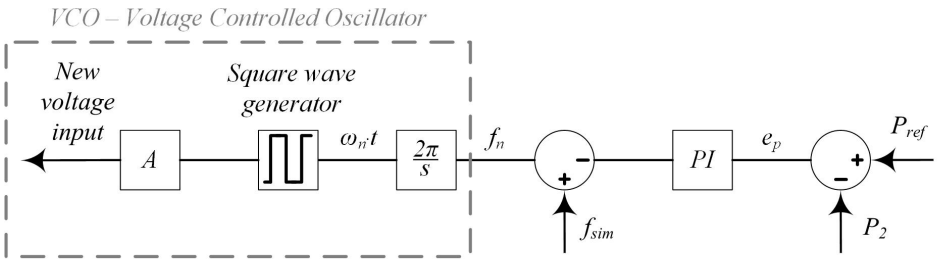

Figure 5.2: Simulink control scheme of IPT frequency control.

Since the voltage over the battery is constant $V_{dc,2}$, it is easy to assume that feedbacking the current is sufficient. This works near the resonance frequency, however, as the point of operation moves towards the limits (because of a high k), a lot of harmonics is introduced to the current. An example is shown in Figure 5.3 when k=0.7 and thereby f=0.77 $\cdot f_0$.

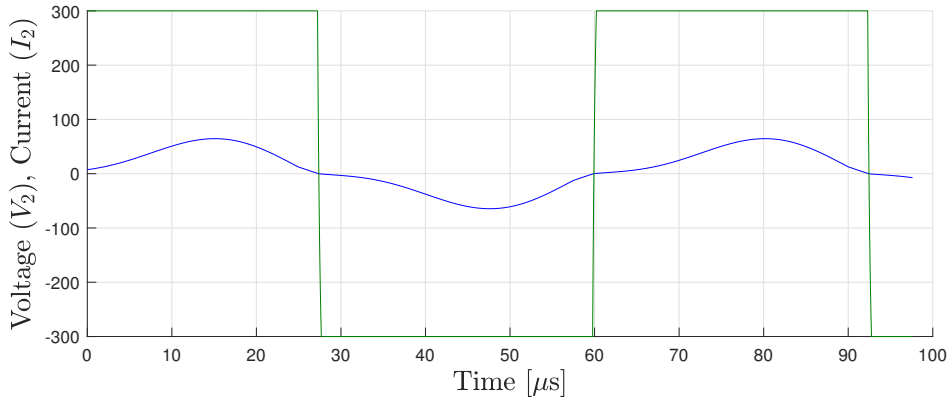

Figure 5.3: The Voltage out (V_2) (green) and the current out (I_2) (blue) when k=0.7 and $f = 0.77 \cdot f_0$.

This figure shows the harmonics that has been introduced to the current, and thereby normal rules for rms calculation of the current does not longer apply. The current is also at the limit of switching polarity multiple times at the point where the square wave switches polarity. This limit is exceeded when the coupling increases further to $k_{max} = 0.8$. This can be seen in Figure 5.4.

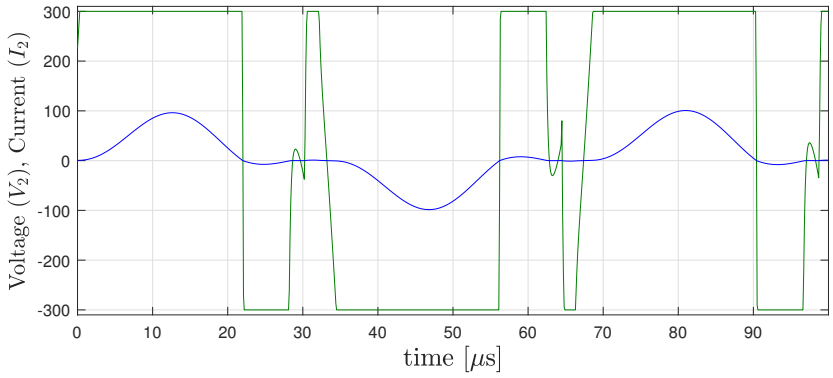

Figure 5.4: The Voltage out (V_2) (green) and the current out (I_2) (blue) when k=0.8 and $f = 0.73 \cdot f_0$.

This figure shows how bad the harmonics in the currents can become, ultimately affecting the voltage when moving too far away from the resonance-frequency. In fact, the assumptions done for the modelling, i.e., a sinusoidal and continuous current with a fundamental/first harmonic component will be less valid as the operating frequency moves away from the resonance frequency. When the characteristics gets as bad as in Figure 5.4, it can be seen that the frequency of the system will also in fact change because of the polarity-switching of the current. This makes it hard to control the power of the system by adjusting the frequency. It is chosen to feedback the power because it is then easier to compare the response when controlling the two different types of systems, i.e., CVL and CRL (sec. 5.4). The Simulink-

diagrams for both systems with the controller implemented can be found in Appendix B.1.2 and B.2.2. Note that a modification has been done to the block that measures the power. Since the power is measured using Fourier analysis, the block needs to know what the operating frequency is. Since this frequency will vary because of the controller, a modification had to be made to the power measurement block where the frequency that the controller outputs is sent as an input to the measurement-block.

The control of the system when exposed for the different disturbances will however just be presented for the CVL. First, control with feedback from the secondary to the primary side will be looked upon. The practical limitations related to such a solution being used subsea will be addressed in section 5.5.

Based on the waveforms presented in Figure 5.4 and the fact that the system is designed to a $k_{min} = 0.2$, the limits of the magnetic couplings where the controller works will be k=0.2 and k=0.7. This is a major assumption, and the magnetic coupling is expected to fall below the minimum coupling in a practical implementation. Therefore, the PI-controller that is suggested needs to be combined with additional controllers that handles when the coupling falls outside the range. An example is a voltage-controller that regulates the voltage V_1 when the coupling falls below k_{min}. However, the proposed PI-controller works for a respectable range of coupling coefficients, and should work in a practical application as long as the magnetic coupling is kept within the given range.

5.1 Controlling output when exposed to a step response

The most likely reason for why an AUV would be exposed for a sudden change in position is for example if bigger fishes or other AUVs crashes into it during charging. However, it is not realistic to model such a change in position as a step response because the mass will resist a change in position. However, step-responses is commonly used to test control of systems, and if the power can be controlled when exposed for a step response in distance, it could certainly also be controlled for a more realistic movement.

A plausible case is a change where the coupling coefficient goes from k=0.2 to k=0.7, which corresponds to a displacement of 8.8 cm, from 13.8cm (k=0.2) to 5cm (k=0.7). The resulting powerflow in such a scenario is depicted in Figure 5.5.

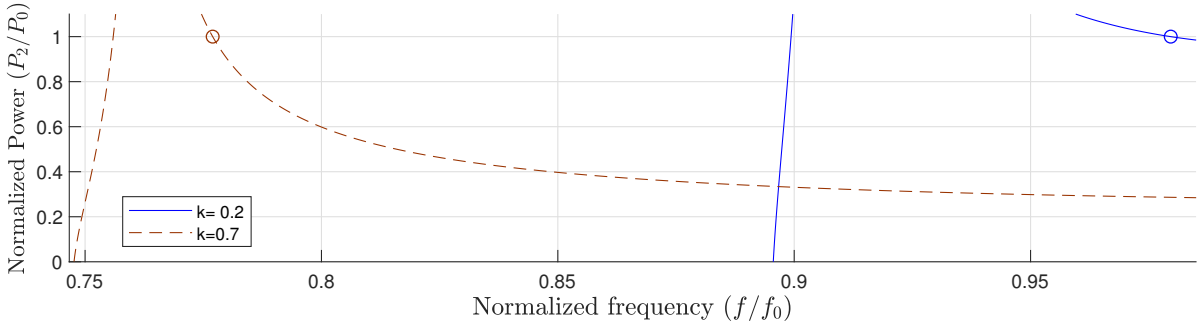

Figure 5.5: Frequency characteristics of the power output for k=0.2 and k = 0.7 showing their respective points of operation.

From this figure, it is possible to show the chain of events in case of such a change in position. The point of operation where there is nominal power flow for k=0.2 is $\omega \approx 0.98 \cdot \omega_0$. When the coupling increases to k=0.7, a sudden drop in power to a value of $P_2 \approx 0.29 \cdot P_0$ will appear, thus creating a huge error between the reference and the measurement. The derivative of the power with respect to the frequency is small in the beginning, but gradually increases as the operating-frequency homes in on the point of operation where $P_2 = P_0$ for k=0.7. This means that an aggressive controller is in danger of overshooting at this point. In the worst case, it will not stop decreasing the frequency before it has gone past the frequency where the system has its maximum power output. The difference in the response between a controlled system and an uncontrolled system is shown in Figure 5.6. The controller has a proportional gain of k_p=0.1 and an integral gain of k_I=100. The simulations are performed in Simulink.

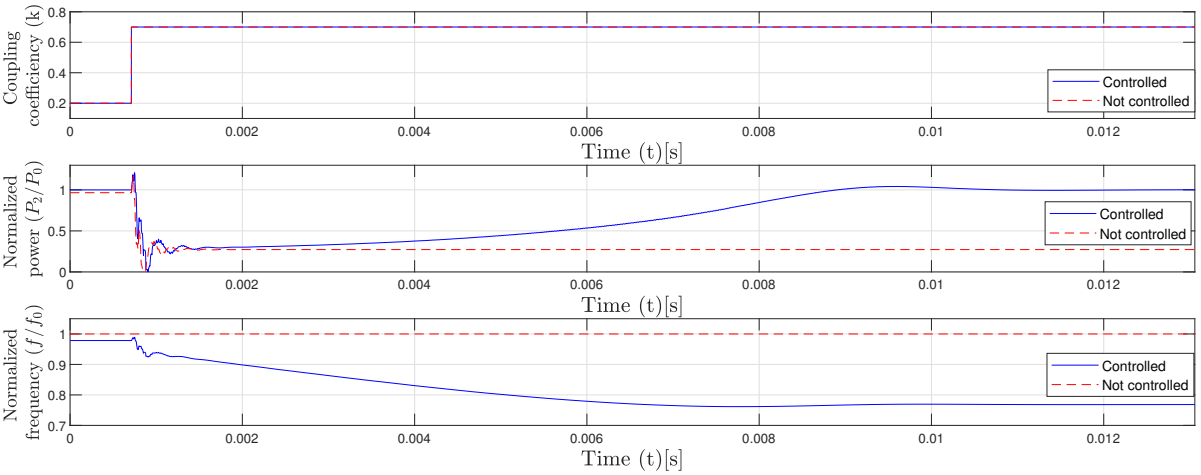

Figure 5.6: Comparison between a controlled system and a non-controlled system when k is increased from 0.2 to 0.7 as a step response.

As can be seen from the figure, the controller ensures that the frequency is decreased to retain the wanted output power, and it takes approx. 10 ms for this to happen. Moreover, it is

observed that there is a small overshoot before the system settles at the reference again. This overshoot is however small, so the gains in the controller are appropriate for this scenario. It is however hard to choose a gain that is appropriate for all changes in coupling coefficiency. For this reason, controlling a step response is a challenging scenario. Ideally, the gain in the controller is adjusted to suit the derivative $dP/d\omega$. Figure 5.7 shows how the distance in frequency between the operation point for each coupling decreases with an increasing k. $dP/d\omega$ will as a result increase with an increasing coupling coefficient.

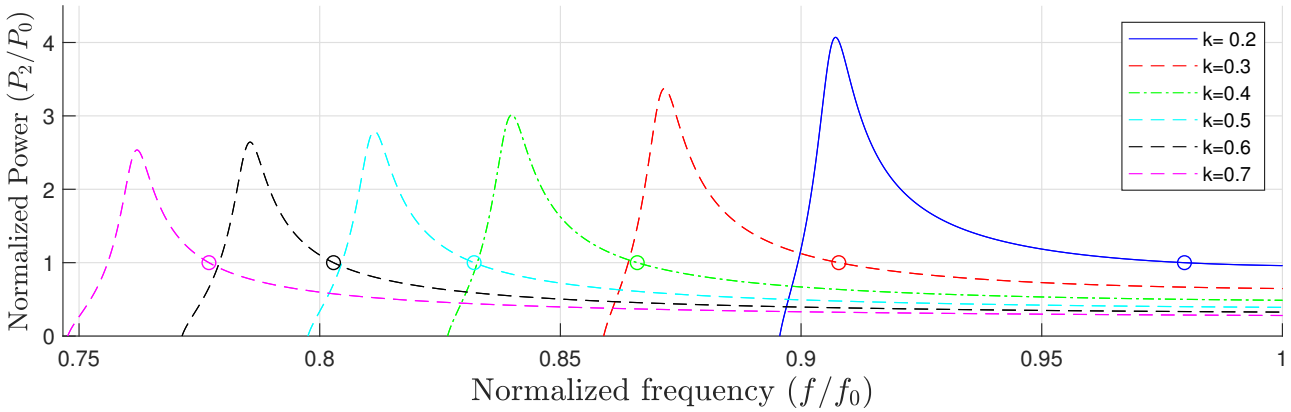

Figure 5.7: The power flow for $k = 0.2 \rightarrow k = 0.7$. The distance in frequency between the points of operations decreases as k increases.

A sophisticated controller should adjust the gain in order to ensure that the control of the the power flow for a step response from k=0.2 to k=0.3 takes the same amount of time as when stepping from k=0.3 to k=0.4 and so forth. Doing this will result in a higher gain for a small magnetic coupling (for faster response) and a smaller gain for a large magnetic coupling (to avoid overshoot).

To illustrate this, the difference in response when using a gain-adjusted controller compared to a controller with a constant gain is presented. The system will be stepped from k=0.2 to k=0.7 with an increasing interval of 0.1, i.e. five iterations. For simplicity, it is only the integral-gain that will be changed. The difference in the response can be seen in Figure 5.8

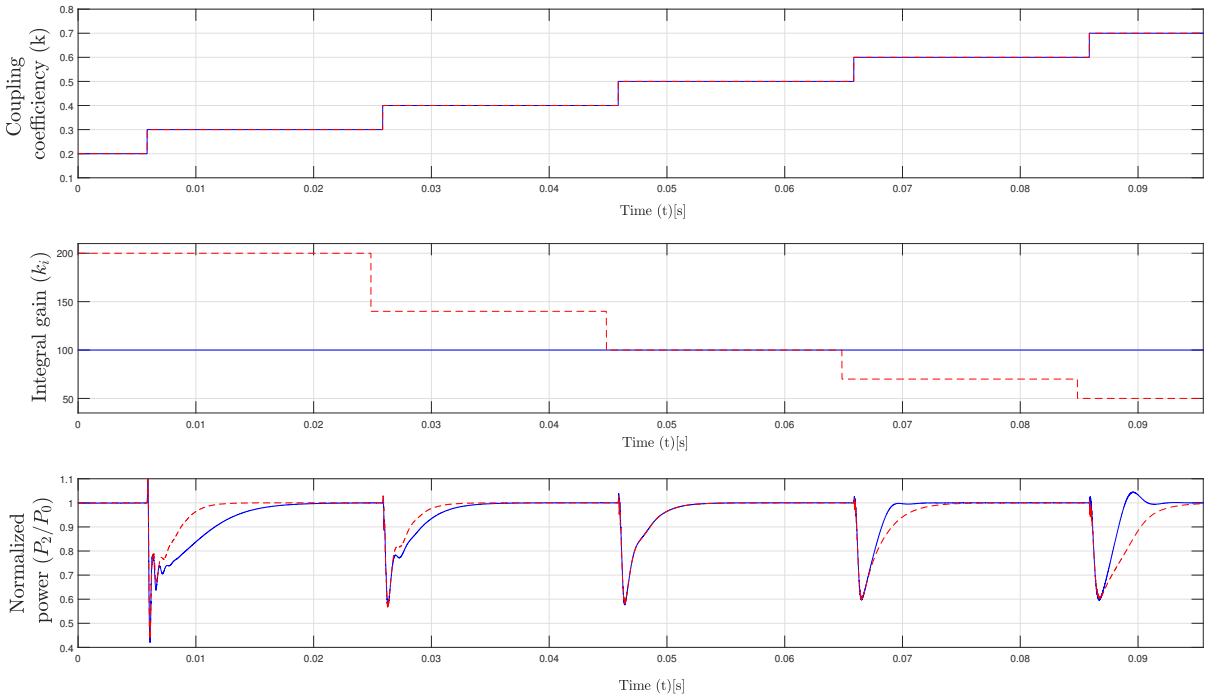

Figure 5.8: Comparison between two types of controller with respectively constant and varying gain.

It is clear that by adjusting the gain, the control-response becomes quite consistent between each change of coupling coefficient. It ensures a fast response for low coupling coefficients while it prevents an overshoot for large coupling coefficients. The gain is in this case done manually in order to prove the feasibility of such a control. It would be possible to implement a controller that adjusts itself based on the mathematical expression for $dP/d\omega$. The derivative can be measured in Simulink by the definition of the derivative

$$\frac{dP}{d\omega} = \frac{P_n - P_{n-1}}{\omega_n - \omega_{n-1}}. \tag{5.5}$$

Where n represents one sampling among the total amount of samplings as given by,

$$n_{tot} = \text{Sampling frequency } (f_s) \cdot \text{Simulation time}(t_s). \tag{5.6}$$

By calculating the derivative for each sampling, it is possible to adjust the gain thereafter. To do this, it would be necessary to create rules for recommended controller gains with respect to the derivative $dP/d\omega$. This could be done by creating two equations for k_I and k_p as a function of the derivative's value respectively. While this approach would be more general and

work for different designed system, an alternative approach designed for the specific system could be proposed in the following way: Since the gain needs to be decreased as the frequency decreases, a simple look-up table with the current frequency as input could be used. In case of a discrete control, the frequency of the previous step could be used:

$$k_{p,n} = k_p(\omega_{n-1}) \quad \text{and} \quad k_{i,n} = k_i(\omega_{n-1}). \tag{5.7}$$

Thereby, appropriate gains would be extracted from the look-up table. This is a quite simple approach, but yields a relatively sophisticated controller. An even more sophisticated controller would be to implement some sort of adaptive control. Since the system is nonlinear, this is a recommended approach. Maximum seeking control has slightly been investigated as a potential controller. Such a controller would need an objective-function that relates the input ω to an objective. It is thinkable that the error between the input and the output could be used. By integrating the relationship for the error, a cost-function that outputs the wanted nominal power at the maximum of the objective-function is obtained as shown in Figure 5.9.

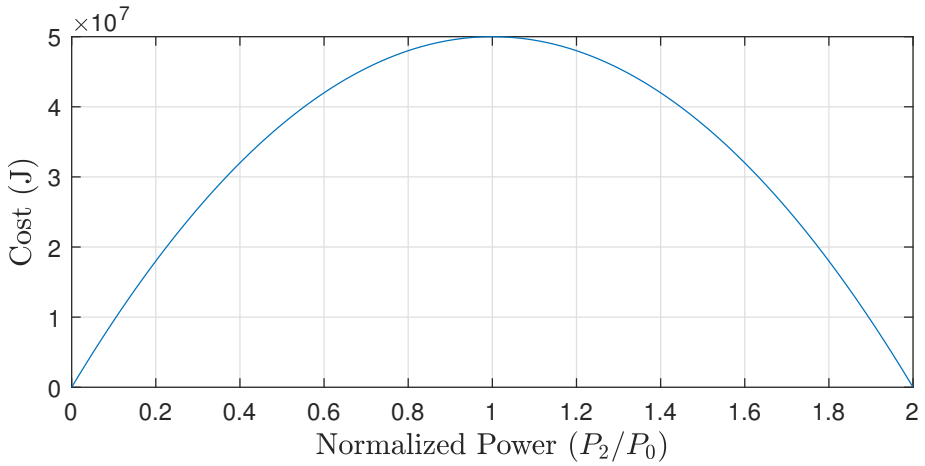

Figure 5.9: Cost-function that outputs the wanted nominal power at its maximum value.

The relationship between the corresponding ω that outputs the nominal power then needs to be found. This is however quite complicated, since it varies with the magnetic coupling. Adaptive control could unfortunately not be further look into due to time-limitations, so this is recommended for further work.

5.2 Controlling output when exposed to a ramp response

Without going into details about hydrodynamics it is well known that the phenomena of currents exists in the sea. The strength of the currents varies, both on water-depth and time. It

is likely that an AUV is exposed for such a current during charging. Since these currents are fairly constant, a case where the position of the AUV moves steadily from k=0.2 to k=0.7 in one second will be looked upon. Having an integral-gain of $k_I = 100$ was not enough to reduce the constantly increasing gap in error to acceptable values. Therefore, the gain was increased to 250. The response compared to a non-controlled system can be seen in Figure 5.10.

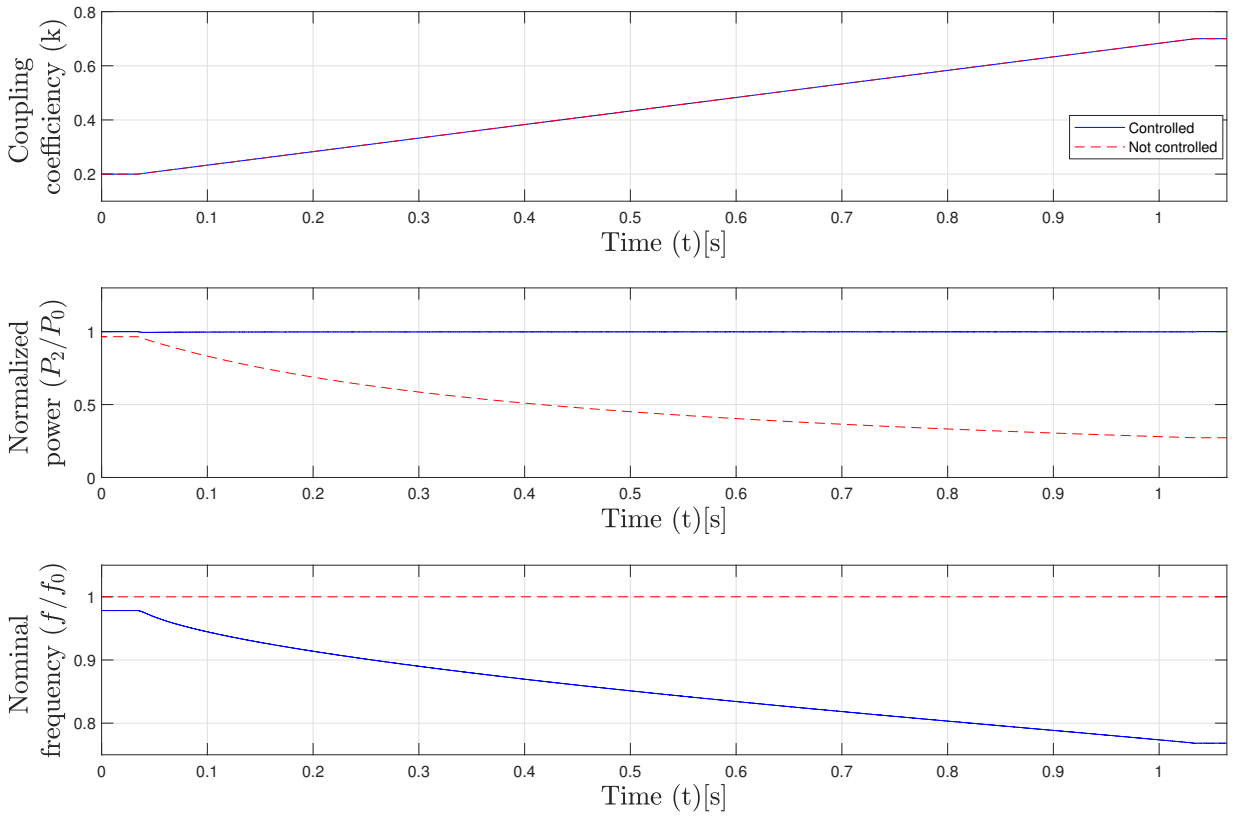

Figure 5.10: Comparison of the difference in response between a controlled and uncontrolled system exposed for a ramp response.

This figure shows that the proposed controller is quite robust against ramp responses within the range $k = 0.2 \rightarrow k = 0.7$.

5.3 Controlling output when exposed to a sinusoidal disturbance

The last case that will be looked upon is when the system is exposed for waves. A good approximation for waves is hard to create, but they are definitely never perfectly sinusoidal. It is important to emphasize that this exposure will only concern charging only a few mbsl. This

is because the effects of the waves will gradually disappear in correlation to the depth of the water. To try and reproduce a wave-disturbance in Simulink, a sine-wave with a frequency of 1 Hz that represent how the waves affects the coupling coefficient is applied. A white noise disturbance with a sampling time of 0.05 seconds is then added to this signal. The combination of the noise and the sine-wave is not expected to be an exact representation of a wave, but the disturbance is irregular and will therefore give a decent indication of the controllers robustness. The irregularities related to such a change in the coupling coefficient makes it hard to choose an appropriate gain. The gain should however ensure that the time where the powerflow is not nominal is minimal, while not making the system unstable for big changes in k. Suitable gains is found to be $k_p = 0.1$ and $k_I = 200$. Figure 5.11 shows a comparison of the response for a controlled and an uncontrolled system exposed for such a disturbance in k.

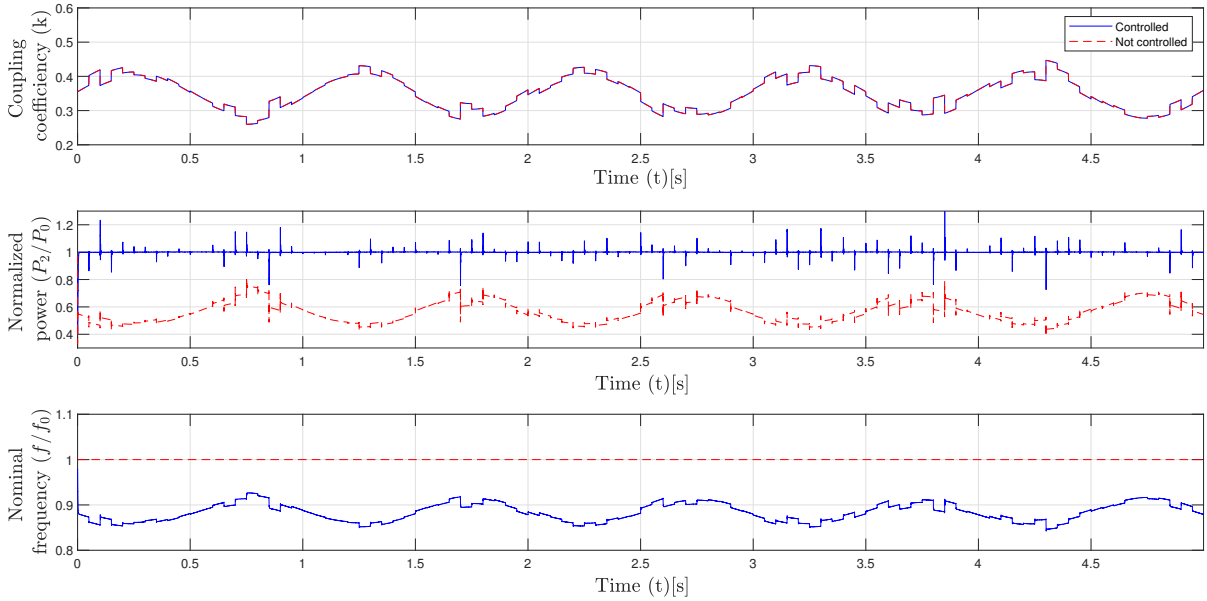

Figure 5.11: Comparison of the difference in response between a controlled and uncontrolled system exposed for a sinusoidal disturbance with white noise.

Looking at the frequency-output, the relationship between how the frequency changes with respect to the coupling coefficient becomes quite clear. The frequency will change in an opposite manner of the coupling coefficient. This makes sense since an increased coupling means a decrease in frequency, and opposite for a decrease in coupling. It is also clear that the controller can handle a oscillatory movement, but the results from this case is not enough to conclude that the controller is robust against waves.

5.4 Difference in control for a CRL and a CVL

Even though the frequency-characteristics of the two types of loads are quite different as shown in section 4.8, it is interesting to see if the response when it comes to control is different for the two systems. Therefore, an identical controller as depicted in Figure 5.2 is implemented in the Simulink model for the CRL.

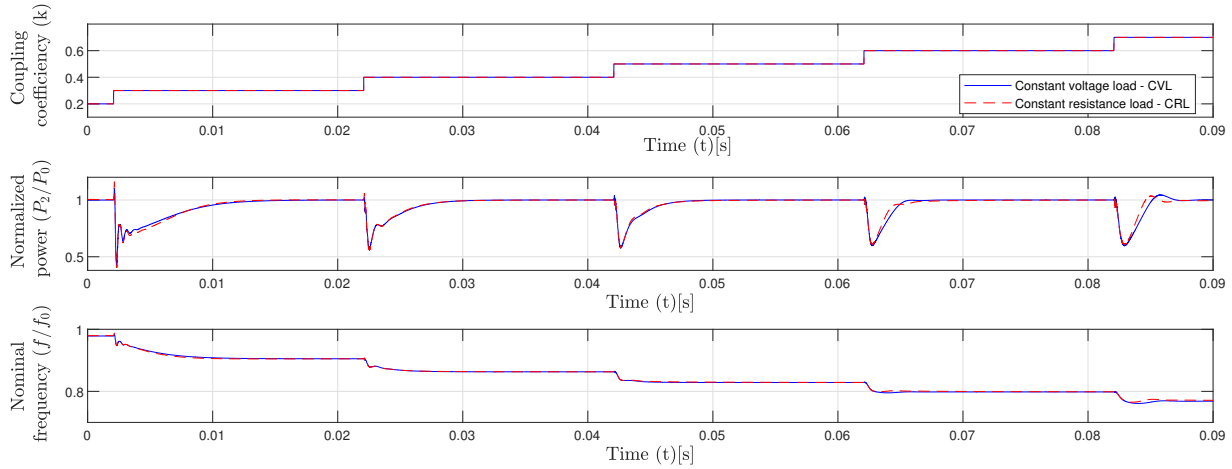

Figure 5.12: A comparison of the dynamic response when the output power is frequency-controlled both for a CVL and a CRL.

The figure shows that there is in fact almost no difference for the two models in terms of controlling the output power by adjusting the frequency. The similarities was in fact quite surprising when keeping in mind how different the frequency characteristics are. However, it makes sense when looking into what the controller actually does. First of all, it has been shown in Figure 4.25 that at the point where the output-power is nominal, the frequency of the two representations coincide. Realizing that the voltage will be $V_2 = V_0 = 300V$ at the nominal power output, the two models are identical at that point. Since the controller will try to keep the output at the nominal value for both P_2 and V_2, the difference in the two models are always minimal, and the response will therefore be quite similar. This is shown in Figure 5.13 for the first step, i.e., k=0.2 to k=0.3. It can be seen that the controller adjusts the frequency so that the voltage are approaching the nominal voltage for the CRL, and thereby the differences in the two models are minimal when the next step is performed.

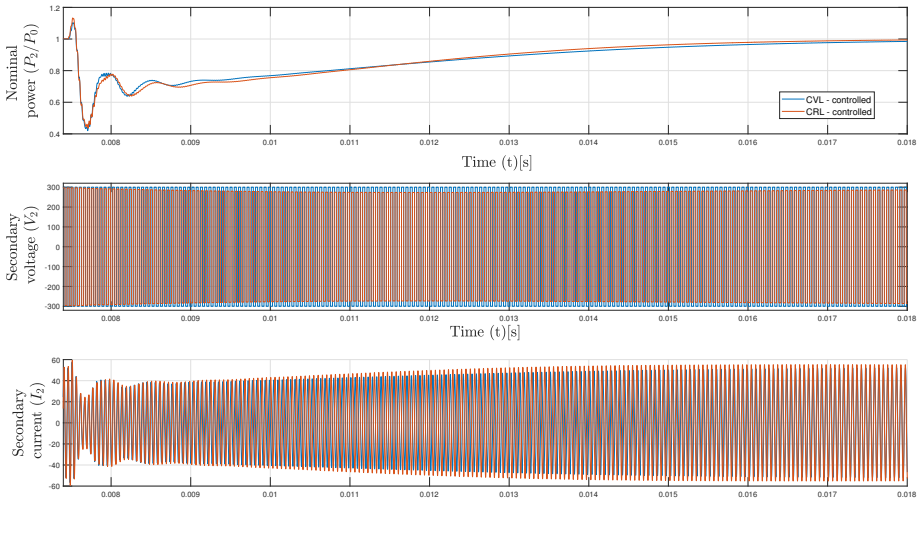

Figure 5.13: Comparison of the waveforms of the voltages and the currents when both controlled systems (varying frequency) are exposed for a step in the magnetic coupling from k=0.2 to k=0.3.

The effects of the differences in the two ways of modelling the systems becomes quite clear when a step response from k=0.2 to k=0.3 is applied to the uncontrolled systems as shown in Figure 5.14. Since the system is uncontrolled, it will operate at the resonance frequency.

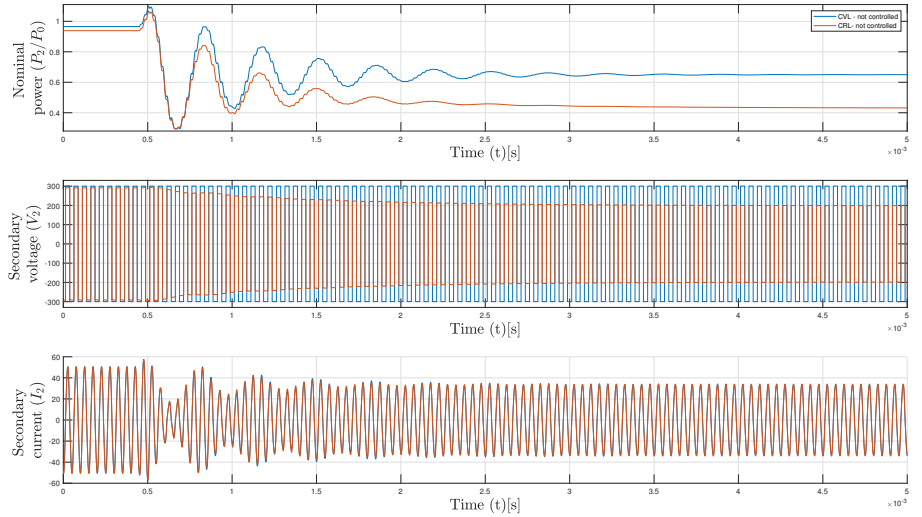

Figure 5.14: Comparison of the waveforms of the voltages and the currents when both uncontrolled systems (fixed frequency) are exposed for a step in the magnetic coupling from k=0.2 to k=0.3.

As seen from the figure, the error is minimal in the start, because the voltage over the resistance is approximately 300 V. The reason for why the voltage is not exactly 300 V is partly

because of the voltage-loss over the resistances in the system, but it is also a result of the increased inductance of the coils to $L_1 = L_2 = 310$ that was performed in section 4.6 in order to be able to control the output power over the entire range of coupling coefficients when unbalancing was introduced. Figure 5.14 shows how the voltage is linearly dependant on the current for a CRL. In case of a CVL, the current will change, while the voltage over the battery remains the same, resulting in a non-linear characteristic for the entire circuit. Since the current is the same for both types of loads, an error between the power-measurements is observed.

5.5 Controlling output without feedback

For a subsea application, having feedback from the secondary circuit is not very practical. This is related to physical restrictions regarding wireless transmission of data in seawater. This has to do with the fact that signal will attenuate faster in water than in air, thereby constraining the possible distance of transfer. Also, the speed of transfer is slower in water, creating a delay in the feedback. Therefore, it is wanted to control the power-output based on the value of the sending side variables. In order to do this, the relationship between the power input and the power output would need to be found. This relationship has previously been discussed as the efficiency of the system. In Figure 4.27 it was found that the point of operation where $P_2 = P_0$, the efficiency is $\eta \approx \eta_{max,k_{min}} = 0.967$ for all coupling coefficients. By measuring the efficiency throughout a simulation where k is steadily increased from k=0.2 to k=0.7 as in section 5.2, it is possible to extract the value of the efficiency at the nominal point of operation for all the coupling coefficients within the range. The result is shown in Figure 5.15.

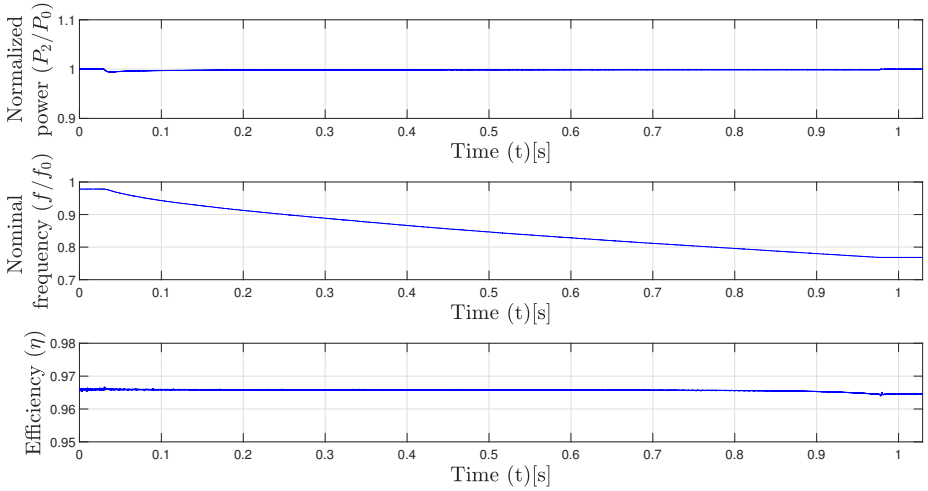

Figure 5.15: The efficiency is $\eta \approx \eta_{max,k_{min}} = 0.967$ when the system is exposed for a ramp-response from k=0.2 to k=0.7 in one second.

This figure shows that the efficiency will in fact be $\eta \approx \eta_{max,k_{min}} = 0.967$ for all the coupling

coefficients in the range $k \in [0.2, 0.7]$. It is however important to state that this model only accounts for the losses due to the coils quality factors. This result would be different if one where to include all the losses in a real life implementation of the system as discussed earlier. The fact that the efficiency is constant over the range is also a result of the design. Recalling that the loss in the system is,

$$P_{loss} = R_1 I_1^2 + R_2 I_2^2.$$

Since the power remains the same, the current will also remain the same because of the constant voltages V_1 and V_2. The resistances will also remain the same, hence, the efficiency will be constant at the nominal point of operation for all couplings within the range. Therefore, this design will limit the necessary ratings of the components in the system. If the system were to be designed so that the system is always operating at the resonance-frequency, the nominal coupling would need to be chosen such that $k_0 = k_{max}$, and as the coupling decreases, V_1 would need to be decreased as given by Equation 4.28, which in turn will result in a higher current to remain the same amount of power [20–22]. Therefore, utilizing the phenomena of bifurcation to control the output power by adjusting the frequency away from the resonance frequency is a highly recommended approach, even though the majority of the literature recommends operation at the resonance frequency.

The information about the efficiency of the system at the different couplings can be used in order to control the output power by using a reference on the primary side that accounts for the expected losses. The reference will then be

$$P_{1,ref} = \frac{P_0}{\eta_{max,k_{min}}} = 10.34kW. \tag{5.8}$$

A problem that is encountered when feedbacking from the primary circuit, is that the simulation enters an algebraic loop because the output P_1 is directly fed through to be compared to P_1 at the same time step. This is solved by introducing a transfer function with a very small time-constant in the feedback. For this case, $1/(1^{-10}s + 1)$ is used. Such a small time-constant will affect the system minimally, while breaking the algebraic loop. To compare the response, the difference between the two types of feedbacks when exposed for the same change in coupling coefficients as in Figure 5.8 with the constant gains $k_p = 0.1$ and $k_I = 100$ is presented.

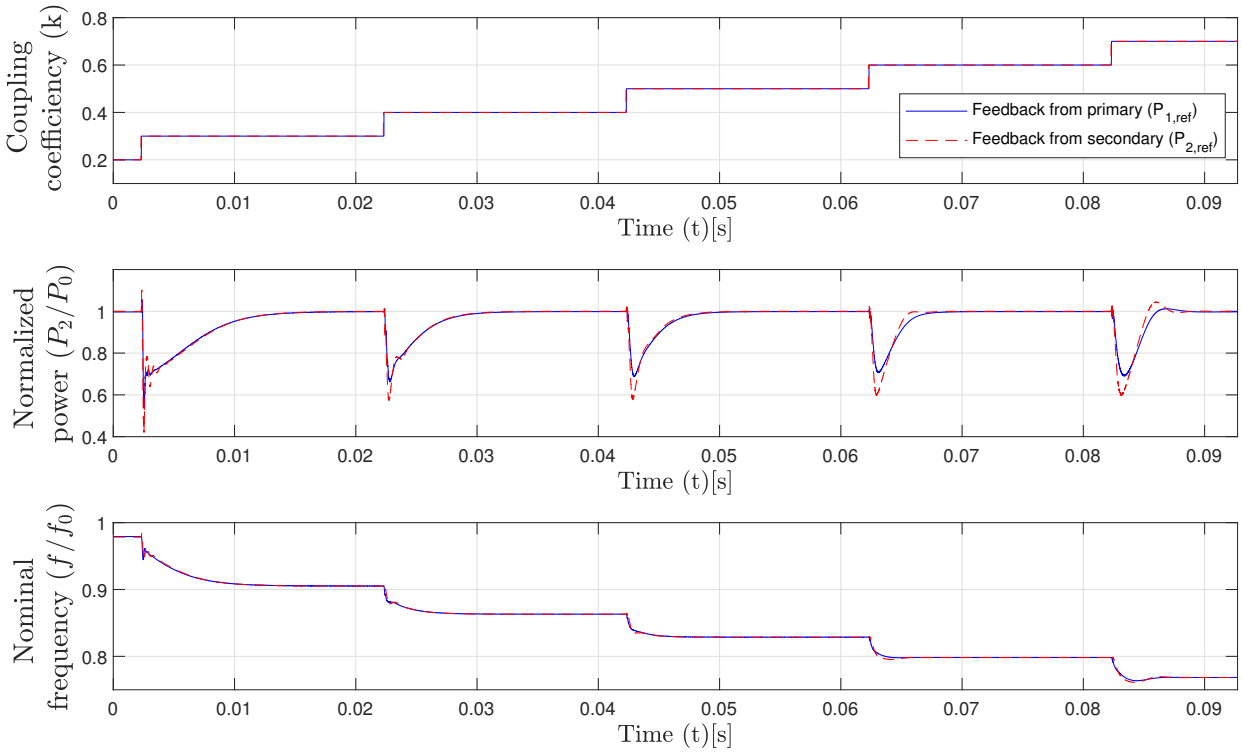

Figure 5.16: Comparison of the difference in response between a feedback from the primary, and a feedback from the seconday.

The figure shows that the response seems to be a bit better when using a reference from the primary circuit compared to a reference from the secondary circuit. It is hard to conclude exactly why this is the case, but it might have to do with the fact that the feedback from the secondary side contains dynamics of the entire resonant system, while the feedback from the primary side will provide a more consistent signal, resulting in less oscillations. Even though it has been shown that the efficiency is similar over the entire range for our model, the efficiency would not be that constant in a real life implementation. First of all, the efficiency would be affected by the ratings of the inverter and the rectifier. Additionally, it is well known that resistances in wires etc. vary with temperature. It is therefore likely that the primary side reference would need to be adjusted regularly. Since the changes that affects the efficiency in operation has slow dynamics, it would be possible to have a wireless feedback from the secondary side to the primary side that indicates if the primary side reference would need to be adjusted. The total system would then control the frequency based on a primary feedback, while the reference would be adjusted based on a wireless communication with the secondary side. Thus, a possible solution for the challenges related to wireless feedback in seawater has been presented.

Chapter 6

Conclusion and further work

6.1 Conclusion

For AUVs to be completely tetherless, the power needs to be delivered from a battery. The constraints regarding the battery-life of AUVs has for a long time been a limiting factor, making them dependent on surface-vessels for charging on site. The AUVs are becoming more advanced, and it is likely that AUVs will increasingly be used as working tools. Such AUVs will have a higher rate of power consumption due to their intended use. The past years, an increased focus on fast charging of EVs is observed, and fast charging demands high power-rates. Based on this it is found that transferring 10 kW to a 300V battery are suitable rates for charging a working class AUV. Further, because of the challenges related to eddy-current loss in seawater, a resonance-frequency of 20 kHz is decided based upon recommendations from literature. In order to design a system that remains the output power by adjusting the frequency of operation, the system is designed so that it operates at the bifurcation-limit for a minimum magnetic coupling. The maximum coupling is then decided by the magnitude of the power-peaks near the limit of operation for the system. The intention of this design is to be able to maintain the power transfer with variations in the magnetic coupling without exceeding the VA ratings of the components. The range of different magnetic couplings where the power output can be controlled is theoretically bigger for a CVL than what a CRL-equivalent indicates, because the peaks are higher. The magnitude of these peaks can be adjusted by unbalancing the ratio between the supply-voltage and the output-voltage, and detuning the resonant part of the sending side, thereby having different resonance-frequencies on both sides of the circuit. It is also found that when the power output is nominal, the differences between the two models are minimal. However, because of the linear relationship between current and voltage for a CRL-equivalent, the output power will be lower for a CRL than for a CVL when the system is not outputting the nominal power.

It is shown that a PI-controller works well to remain the wanted power output for the possible disturbances in position that an AUV might face during charging. There is no problems with stability or degraded performance when the coupling changes. However, since $dP/d\omega$ varies with the coupling coefficient, it is not possible to find a constant gain that gives a

consistent response for all changes in magnetic coupling. The simplest solution to this is to modify the PI-controller to vary its gain. A more sophisticated approach is however to implement an adaptive controller or some other nonlinear regulation to ensure a similar dynamic response for all changes in coupling. This is recommended for further work.

As a result of the design, the efficiency of the proposed system has a constant efficiency of approximately 96,7 % for magnetic couplings ranging from k=0.2 to k=0.7. A higher coupling will most likely not be realistic. To remain the wanted power output for lower couplings, other parameters like the amplitude of the voltage-supply would need to be adjusted. Looking into an integration of such control to the system presented in this thesis is also recommended for further work. Even though the losses in an implemented system would be larger due to eddy-current losses, thermal constants and non-ideal components, it is still expected that the efficiency will have small or slow changes when the coupling changes. This property can be utilized to control the variables on the receiving side based on the variables on the sending side, thus eliminating the need for a feedback that requires fast communication from the receiving side. However, based on the assumption that the efficiency will change slowly, a wireless feedback from the secondary side that adjusts the primary side reference will ensure that the power output remains nominal for a varying efficiency.

6.2 Recommendations for further work

For a better understanding of the seawater's effect on the magnetic coupling, it is recommended to do more research on suitable coil-geometries and model them in a tool that can perform FEM-analyses. This will give a better indication of the losses due to eddy-currents and the coupling coefficients relation to the distance between the coils in case of seawater as the separating medium. The FEM-analyses can also be used as a basis to determine which geometry that is suited for charging of an AUV. A controller that handles a lower coupling than the minimum coupling (k_{min}) that is decided by design, needs to be integrated with the proposed controller to ensure a nominal output over the entire range of expected couplings. This can be achieved by allowing the voltage of the sending side to be controlled, as conventional control-methods suggests [20–22]. This will however lead to some additional problems, especially regarding control of the output-power based on the sending side variables, since the currents in the system will change, thereby affecting the efficiency more than the controlled suggested in this thesis.

In addition, since the system is nonlinear, it is recommended to implement some sort of nonlinear control that ensures a consistent response for different variations in magnetic coupling. Such control should be possible to integrate in to the Simulink model that is made for this thesis. Maximum seeking-control has slightly been looked upon as a possible solution, and should be a feasible approach. The cost-function is then recommended to be created based

on the error between the output and the reference.

When this is done, it is recommended to make a prototype of the system. To reduce costs, the design should be scaled down from kW-range to W-range, while ensuring that the system-characteristics remains the same.

References

[1] G. Guidi and J. A. Suul, "Minimizing Converter Requirements of Inductive Power Transfer Systems With Constant Voltage Load and Variable Coupling Conditions," *IEEE Transactions on Industrial Electronics*, vol. 63, no. 11, pp. 6835–6844, Nov. 2016.

[2] "Governing Documents | Wireless Power Consortium." [Online]. Available: https://www.wirelesspowerconsortium.com/about/governing-documents

[3] G. A. Covic and J. T. Boys, "Modern Trends in Inductive Power Transfer for Transportation Applications," *IEEE Journal of Emerging and Selected Topics in Power Electronics*, vol. 1, no. 1, pp. 28–41, Mar. 2013.

[4] S. Li and C. C. Mi, "Wireless Power Transfer for Electric Vehicle Applications," *IEEE Journal of Emerging and Selected Topics in Power Electronics*, vol. 3, no. 1, pp. 4–17, Mar. 2015.

[5] G. A. Covic and J. T. Boys, "Inductive Power Transfer," *Proceedings of the IEEE*, vol. 101, no. 6, pp. 1276–1289, Jun. 2013.

[6] G. Guidi, J. A. Suul, F. Jenset, and I. Sorfonn, "Wireless Charging for Ships: High-Power Inductive Charging for Battery Electric and Plug-In Hybrid Vessels," *IEEE Electrification Magazine*, vol. 5, no. 3, pp. 22–32, Sep. 2017.

[7] Markets and markets, "Wireless Power Transmission Market Size Growth Analysis and Forecast to 2022." [Online]. Available: https://www.marketsandmarkets.com/Market-Reports/wireless-power-market-168050212.html

[8] D.-j. Li, Y.-h. Chen, J.-g. Shi, and C.-j. Yang, "Autonomous underwater vehicle docking system for cabled ocean observatory network," *Ocean Engineering*, vol. 109, pp. 127–134, Nov. 2015. [Online]. Available: http://www.sciencedirect.com/science/article/pii/S0029801815004278

[9] M. Lin, D. Li, and C. Yang, "Design of an ICPT system for battery charging applied to underwater docking systems," *Ocean Engineering*, vol. 145, pp. 373–381, Nov. 2017. [Online]. Available: http://www.sciencedirect.com/science/article/pii/S0029801817304559

[10] J.-g. Shi, D.-j. Li, and C.-j. Yang, "Design and analysis of an underwater inductive coupling power transfer system for autonomous underwater vehicle docking applications," *Journal of Zhejiang University SCIENCE C*, vol. 15, no. 1, pp. 51–62, Jan. 2014. [Online]. Available: https://doi.org/10.1631/jzus.C1300171

[11] J. Zhou, D.-j. Li, and Y. Chen, "Frequency selection of an inductive contactless power transmission system for ocean observing," *Ocean Engineering*, vol. 60, pp. 175–185, Mar. 2013. [Online]. Available: https://linkinghub.elsevier.com/retrieve/pii/S0029801813000085

[12] "NTNUs dypeste laboratorium åpnes i Trondheimsfjorden." [Online]. Available: https://gemini.no/kortnytt/ntnus-dypeste-laboratorium-apnes-i-trondheimsfjorden/

[13] D. A. Fleisch, *A student's guide to Maxwell's equations*. Cambridge, UK ; New York: Cambridge University Press, 2008, oCLC: ocn173182616.

[14] X. Lu, P. Wang, D. Niyato, D. I. Kim, and Z. Han, "Wireless Charging Technologies: Fundamentals, Standards, and Network Applications," *IEEE Communications Surveys Tutorials*, vol. 18, no. 2, pp. 1413–1452, 2016.

[15] Z. Popovic, "Near- and far-field wireless power transfer," *IEEE Communications Surveys & Tutorials*, pp. 3–6, Oct. 2017.

[16] A. Kurs, A. Karalis, R. Moffatt, J. D. Joannopoulos, P. Fisher, and M. Soljačić, "Wireless Power Transfer via Strongly Coupled Magnetic Resonances," *Science*, vol. 317, no. 5834, pp. 83–86, Jul. 2007. [Online]. Available: https://science.sciencemag.org/content/317/5834/83

[17] C.-S. Wang, O. H. Stielau, and G. A. Covic, "Design considerations for a contactless electric vehicle battery charger," *IEEE Transactions on Industrial Electronics*, vol. 52, no. 5, pp. 1308–1314, Oct. 2005.

[18] R. Bosshard, J. W. Kolar, and B. Wunsch, "Control method for Inductive Power Transfer with high partial-load efficiency and resonance tracking," in *2014 International Power Electronics Conference (IPEC-Hiroshima 2014 - ECCE ASIA)*, May 2014, pp. 2167–2174.

[19] E. Gati, G. Kampitsis, and S. Manias, "Variable Frequency Controller for Inductive Power Transfer in Dynamic Conditions," *IEEE Transactions on Power Electronics*, vol. 32, no. 2, pp. 1684–1696, Feb. 2017.

[20] T. Diekhans and R. W. D. Doncker, "A Dual-Side Controlled Inductive Power Transfer System Optimized for Large Coupling Factor Variations and Partial Load," *IEEE Transactions on Power Electronics*, vol. 30, no. 11, pp. 6320–6328, Nov. 2015.

[21] D. J. Thrimawithana and U. K. Madawala, "A primary side controller for inductive power transfer systems," in *2010 IEEE International Conference on Industrial Technology*, Mar. 2010, pp. 661–666.

[22] U. K. Madawala and D. J. Thrimawithana, "New technique for inductive power transfer using a single controller," *IET Power Electronics*, vol. 5, no. 2, pp. 248–256, Feb. 2012.

[23] Y. Zhang, K. Chen, F. He, Z. Zhao, T. Lu, and L. Yuan, "Closed-Form Oriented Modeling and Analysis of Wireless Power Transfer System With Constant-Voltage Source and Load," *IEEE Transactions on Power Electronics*, vol. 31, no. 5, pp. 3472–3481, May 2016.

[24] Z. Zhang, J. Xu, H. Huang, and H. Guo, "Analytic solution for transfer efficiency of magnetically-coupled inductive wireless power transfer system with constant power load," in *2017 20th International Conference on Electrical Machines and Systems (ICEMS)*, Aug. 2017, pp. 1–5.

[25] Z. Cheng, Y. Lei, K. Song, and C. Zhu, "Design and Loss Analysis of Loosely Coupled Transformer for an Underwater High-Power Inductive Power Transfer System," *IEEE Transactions on Magnetics*, vol. 51, no. 7, pp. 1–10, Jul. 2015.

[26] W. Niu, W. Gu, and J. Chu, "Analysis and experimental results of frequency splitting of underwater wireless power transfer," *The Journal of Engineering*, vol. 2017, no. 7, pp. 385–390, Jul. 2017. [Online]. Available: https://digital-library.theiet.org/content/journals/10.1049/joe.2017.0194

[27] A. F. Molland, "Chapter 10 - Underwater vehicles," in *The Maritime Engineering Reference Book*. Oxford: Butterworth-Heinemann, Jan. 2008, pp. 728–783. [Online]. Available: http://www.sciencedirect.com/science/article/pii/B978075068987800010X

[28] Anders Kjellevoll, "Wireless power transfer for subsea applications. Prelimenary project." Dec. 2018.

[29] N. O. a. A. A. US Department of Commerce, "How much of the ocean have we explored?" [Online]. Available: https://oceanservice.noaa.gov/facts/exploration.html

[30] Kongsberg, "Technical Datasheet - Hugin Superior." [Online]. Available: https://www.km.kongsberg.com/ks/web/nokbg0397.nsf/AllWeb/5FA9C25E1EDE3482C1258359004B6669/$file/Hugin-Superior-Technicalsheet.pdf?OpenElement

[31] DOF Subsea, "Glider AUV - DOF Subsea." [Online]. Available: http://www.dofsubsea.com/rov/glider-auv/

[32] Richard Thomson and William Emery, *Data Analysis Methods in Physical Oceanography*, 3rd ed. Elsevier, 2014. [Online]. Available: https://linkinghub.elsevier.com/retrieve/pii/C20100663620

[33] "Figure 4: Hugin in the stinger, while being deployed." [Online]. Available: https://www.researchgate.net/figure/Hugin-in-the-stinger-while-being-deployed_fig4_314177507

[34] NFEA, "Eelume.jpg (2100×1182)." [Online]. Available: https://nfea.no/wp-content/uploads/2018/10/Eelume.jpg

[35] "WiSub." [Online]. Available: http://www.wisub.com/

[36] S. mobilus, "Wireless Power Transfer for Light-Duty Plug-In/Electric Vehicles and Alignment Methodology (J2954 Ground Vehicle Standard) - SAE Mobilus," Nov. 2017. [Online]. Available: https://saemobilus.sae.org/content/J2954_201711

[37] Kongsberg, "Technical Datasheet - Hugin 1000." [Online]. Available: https://deepoceangroup.com/wp-content/uploads/2015/11/550058f07a910.pdf

[38] ——, "Eelume: A Flexible and Subsea Resident IMR vehicle - Kongsberg Maritime." [Online]. Available: https://www.km.kongsberg.com/ks/web/nokbg0238.nsf/AllWeb/9198BD62EF177FE1C125811E002AC5E6?OpenDocument

[39] Steve Hanley, "EV Charging Is Getting Faster — Slowly," Dec. 2018. [Online]. Available: https://cleantechnica.com/2018/12/16/ev-charging-is-getting-faster-slowly/

[40] Albert Bradley, M.D. Feezor, and Hanumant Singh, "(PDF) Power systems for autonomous underwater vehicles," 2001. [Online]. Available: https://www.researchgate.net/publication/3231230_Power_systems_for_autonomous_underwater_vehicles

[41] Gianfranco Pistoia, *Lithium-Ion Batteries*, 1st ed. Elsevier, 2014. [Online]. Available: https://linkinghub.elsevier.com/retrieve/pii/C20110096588

[42] K. Young, C. Wang, L. Wang, and K. Strunz, "Electric Vehicle Battery Technologies," *Electric Vehicle Integration into Modern Power Networks*, pp. 15–56, Jan. 2013.

[43] Y. Gibbs, "Past Project - Beamed Power Research," May 2017. [Online]. Available: http://www.nasa.gov/centers/dryden/history/pastprojects/Beam/index.html

[44] L. Xie, Y. Shi, Y. T. Hou, and A. Lou, "Wireless power transfer and applications to sensor networks," *IEEE Wireless Communications*, vol. 20, no. 4, pp. 140–145, Aug. 2013.

[45] James W. Nilsson and Susan A. Riedel, *Electric circuits*, 9th ed. Pearson, 2011.

[46] Engineering toolbox, "Permeability." [Online]. Available: https://www.engineeringtoolbox.com/permeability-d_1923.html

[47] F. W. Grover, *Inductance Calculations: Working Formulas and Tables*. Courier Corporation, Jan. 2004, google-Books-ID: K3KHi9lIltsC.

[48] S. Babic, F. Sirois, C. Akyel, and C. Girardi, "Mutual Inductance Calculation Between Circular Filaments Arbitrarily Positioned in Space: Alternative to Grover's Formula," *IEEE Transactions on Magnetics*, vol. 46, no. 9, pp. 3591–3600, Sep. 2010.

[49] D. Ongayo and M. Hanif, "An overview of single-sided and double-sided winding inductive coupling transformers for wireless Electric Vehicle charging," in *2015 IEEE 2nd International Future Energy Electronics Conference (IFEEC)*, Nov. 2015, pp. 1–6.

[50] Viktor Bana, Greg Anderson, Lu Xu, Doeg Rodriguez, Alex Phipps, and John D. Rockway, "Characterization of Coupled Coil in Seawater for Wireless Power Transfer," *SSC Pacific San Diego, CA 92152-5001*, Sep. 2013. [Online]. Available: http://www.dtic.mil/dtic/tr/fulltext/u2/a590746.pdf

[51] C. L. W. Sonntag, E. A. Lomonova, and J. L. Duarte, "Implementation of the Neumann formula for calculating the mutual inductance between planar PCB inductors," in *2008 18th International Conference on Electrical Machines*, Sep. 2008, pp. 1–6.

[52] R. Duarte and G. Klaric, "Analysis of the Coupling Coefficient in Inductive Energy Transfer Systems," *Active and Passive Electronic Components*, vol. 2014, Jun. 2014.

[53] Jens G. Balchen, Trond Andersen, and Bjarne A. Foss, *Reguleringsteknikk*, 6th ed. NTNU, 2016.

[54] C. Jiang, K. Chau, L. Chunhua, and C. H. T. Lee, "An Overview of Resonant Circuits for Wireless Power Transfer," *Energies*, vol. 10, p. 894, Jun. 2017.

[55] Z. U. Zahid, C. Zheng, R. Chen, W. E. Faraci, J. J. Lai, M. Senesky, and D. Anderson, "Design and control of a single-stage large air-gapped transformer isolated battery charger for wide-range output voltage for EV applications," in *2013 IEEE Energy Conversion Congress and Exposition*, Sep. 2013, pp. 5481–5487.

[56] C.-S. Wang, G. A. Covic, and O. H. Stielau, "Power transfer capability and bifurcation phenomena of loosely coupled inductive power transfer systems," *IEEE Transactions on Industrial Electronics*, vol. 51, no. 1, pp. 148–157, Feb. 2004.

[57] J. L. Villa, J. Sallan, J. F. S. Osorio, and A. Llombart, "High-Misalignment Tolerant Compensation Topology For ICPT Systems," *IEEE Transactions on Industrial Electronics*, vol. 59, no. 2, pp. 945–951, Feb. 2012.

[58] W. Zhang and C. C. Mi, "Compensation Topologies of High-Power Wireless Power Transfer Systems," *IEEE Transactions on Vehicular Technology*, vol. 65, no. 6, pp. 4768–4778, Jun. 2016.

[59] N. Jamal, S. Saat, Y. Yusop, T. Zaid, M. S. Mohamad Isa, and A. Isa, "Investigations on Capacitor Compensation Topologies Effects of Different Inductive Coupling Links Configurations," *International Journal of Power Electronics and Drive Systems*, vol. 6, pp. 274–281, Jun. 2015.

[60] R. Bosshard, J. W. Kolar, J. Muhlethaler, I. Stevanovic, B. Wunsch, and F. Canales, "Modeling and η - α -Pareto Optimization of Inductive Power Transfer Coils for Electric Vehicles," *IEEE Journal of Emerging and Selected Topics in Power Electronics*, vol. 3, no. 1, pp. 50–64, Mar. 2015. [Online]. Available: http://ieeexplore.ieee.org/document/6762832/

[61] "Micro Circular Connector series - wet mate connectivity solution for underwater technology applications." [Online]. Available: https://www.macartney.com/what-we-offer/systems-and-products/connectors/subconn/subconn-micro-circular-series/

[62] SINTEF, "Power electronics for subsea applications." [Online]. Available: http://www.sintef.no/en/power-electronics-for-subsea-applications/

[63] G. Guidi and J. Suul, "Modelling techniques for designing high-performance on-road dynamic charging systems for electric vehicles," *EVS 31 & EVTeC 2018*, Sep. 2018.

[64] R. L. Steigerwald, "A comparison of half-bridge resonant converter topologies," *IEEE Transactions on Power Electronics*, vol. 3, no. 2, pp. 174–182, Apr. 1988.

[65] MATLAB, "Model two coupled inductors for circuit envelope analysis - MATLAB - MathWorks Nordic." [Online]. Available: https://se.mathworks.com/help/simrf/ref/mutualinductor.html

[66] R. Bosshard, U. Badstubner, J. W. Kolar, and I. Stevanovic, "Comparative evaluation of control methods for Inductive Power Transfer," in *2012 International Conference on Renewable Energy Research and Applications (ICRERA)*. Nagasaki, Japan: IEEE, Nov. 2012, pp. 1–6. [Online]. Available: http://ieeexplore.ieee.org/document/6477400/

[67] K. Aditya and s. willimason, "A Review of Optimal Conditions for Achieving Maximum Power Output and Maximum Efficiency for a Series-Series Resonant Inductive Link," *IEEE Transactions on Transportation Electrification*, vol. 3, Jun. 2016.

[68] W. X. Zhong and S. Y. R. Hui, "Maximum Energy Efficiency Tracking for Wireless Power Transfer Systems," *IEEE Transactions on Power Electronics*, vol. 30, no. 7, pp. 4025–4034, Jul. 2015.

[69] M. Fu, H. Yin, X. Zhu, and C. Ma, "Analysis and Tracking of Optimal Load in Wireless Power Transfer Systems," *IEEE Transactions on Power Electronics*, vol. 30, no. 7, pp. 3952–3963, Jul. 2015.

[70] G. Guidi and J. A. Suul, "Transient Control of Dynamic Inductive EV Charging and Impact on Energy Efficiency when Passing a Roadside Coil Section," *2018 IEEE PELS Workshop on Emerging Technologies: Wireless Power Transfer (Wow)*, pp. 1–7, Jun. 2018.

[71] S. Y. R. Hui, W. Zhong, and C. K. Lee, "A Critical Review of Recent Progress in Mid-Range Wireless Power Transfer," *IEEE Transactions on Power Electronics*, vol. 29, no. 9, pp. 4500–4511, Sep. 2014.

[72] Electricalbaba.com, "Q Factor / Quality Factor of a Coil," May 2016. [Online]. Available: https://electricalbaba.com/q-factor-quality-factor-of-a-coil/

[73] L. Jinliang, D. Qijun, H. Wenshan, and Z. Hong, "Research on quality factor of the coils in wireless power transfer system based on magnetic coupling resonance," in *2017 IEEE PELS Workshop on Emerging Technologies: Wireless Power Transfer (WoW)*, May 2017, pp. 123–127.

[74] W. Zhang, S. Wong, C. K. Tse, and Q. Chen, "Design for Efficiency Optimization and Voltage Controllability of Series–Series Compensated Inductive Power Transfer Systems," *IEEE Transactions on Power Electronics*, vol. 29, no. 1, pp. 191–200, Jan. 2014.

[75] S. S. Mohan, M. d. M. Hershenson, S. P. Boyd, and T. H. Lee, "Simple accurate expressions for planar spiral inductances," *IEEE Journal of Solid-State Circuits*, vol. 34, no. 10, pp. 1419–1424, Oct. 1999.

[76] J. O. Mur-Miranda, G. Fanti, Y. Feng, K. Omanakuttan, R. Ongie, A. Setjoadi, and N. Sharpe, "Wireless power transfer using weakly coupled magnetostatic resonators," in *2010 IEEE Energy Conversion Congress and Exposition*, Sep. 2010, pp. 4179–4186.

Appendix A

Maple scripts

A.1 Finding the equivalent CVL resistance and the phase angle of the total impedance

Script for calculating the equivalent resistance representing a battery and its phase-angle (sending impedance). Section 4.3.2 Constant voltage load.

First: Recalling the system equations and giving maple assumptions on the variables.

```
restart;
assume(R_1 ≥ 0, R_2 ≥ 0, w > 0, M > 0, V_1 > 0, L_1 > 0, L_2 > 0, C_1 > 0, C_2 > 0, V_2 > 0, R_eq > 0, w0 > 0)
```

System-equations

```
V_1_eq := Z_1·i_1 + M·s·i_2 :
V_2_eq := Z_2·i_2 + M·s·i_1 :
i_1_eq := (Z_2·V_1)/(Z_1·Z_2 − M^2·s^2) :
i_2_eq := −(M·s·V_1)/(Z_1·Z_2 − M^2·s^2) :
s_eq := I·w :

i_2_eq := subs(s = s_eq, i_2_eq);
i_1_eq := subs(s = s_eq, i_1_eq);
```

$$i\_2\_eq := \frac{-I\,M\sim w\sim V\_1\sim}{M\sim^2 w\sim^2 + Z\_1\,Z\_2}$$

$$i\_1\_eq := \frac{Z\_2\,V\_1\sim}{M\sim^2 w\sim^2 + Z\_1\,Z\_2} \qquad \textbf{(1)}$$

```
Z_1_eq := R_1 + s·L_1 + 1/(s·C_1) :
Z_2_eq := R_2 + s·L_2 + 1/(s·C_2) + R_eq :
Z_1_eq := subs(s = s_eq, Z_1_eq);
Z_2_eq := subs(s = s_eq, Z_2_eq);
```

$$Z\_1\_eq := R\_1\sim + I\,w\sim L\_1\sim - \frac{I}{w\sim C\_1\sim}$$

$$Z\_2\_eq := R\_2\sim + I\,w\sim L\_2\sim - \frac{I}{w\sim C\_2\sim} + R\_eq\sim \qquad \textbf{(2)}$$

Z_1 and Z_2 into i_2.

```
i_2_eq := expand(subs(Z_2 = Z_2_eq, Z_1 = Z_1_eq, i_2_eq));
```

$$i\_2\_eq := \left(-I\,M\sim w\sim V\_1\sim\right) \Big/ \left(M\sim^2 w\sim^2 + R\_1\sim R\_2\sim + I\,R\_1\sim w\sim L\_2\sim - \frac{I\,R\_1\sim}{w\sim C\_2\sim} + R\_1\sim R\_eq\sim + I\,w\sim L\_1\sim R\_2\sim - w\sim^2 L\_1\sim L\_2\sim + \frac{L\_1\sim}{C\_2\sim} + I\,w\sim L\_1\sim R\_eq\sim - \frac{I\,R\_2\sim}{w\sim C\_1\sim} + \frac{L\_2\sim}{C\_1\sim} - \frac{1}{w\sim^2 C\_1\sim C\_2\sim} - \frac{I\,R\_eq\sim}{w\sim C\_1\sim}\right) \qquad \textbf{(3)}$$

V_2 is in phase with i_2 - This is true when abs(I_2)*R_eq=V_2. Need to find absoulte value of i_2.

```
i_2_abs := abs(i_2_eq)
```

$$i\_2\_abs := \left(M\sim w\sim V\_1\sim\right) \Big/ \left(\left(w\sim^2 L\_1\sim L\_2\sim - M\sim^2 w\sim^2 - R\_1\sim R\_2\sim - R\_1\sim R\_eq\sim - \frac{L\_1\sim}{C\_2\sim} - \frac{L\_2\sim}{C\_1\sim} + \frac{1}{w\sim^2 C\_1\sim C\_2\sim}\right)^2 + \left(-R\_1\sim w\sim L\_2\sim + \frac{R\_1\sim}{w\sim C\_2\sim} - w\sim L\_1\sim R\_2\sim - w\sim L\_1\sim R\_eq\sim + \frac{R\_2\sim}{w\sim C\_1\sim} + \frac{R\_eq\sim}{w\sim C\_1\sim}\right)^2\right)^{1/2} \qquad \textbf{(4)}$$

Solving the equation for R_eq.

```
R_eq_eq := solve(i_2_abs·R_eq = V_2, R_eq) :
```

Since R_eq is of second degree in the equation for i_2, we get two solutions for R_eq. The positive (and hence right) solution is number 2.

```
R_eq_eq_loss := simplify(R_eq_eq[2]);
```

$$R\_eq\_eq\_loss := \left(\left(\left(-V\_2\sim^2 w\sim^8 C\_1\sim^4 (L\_2\sim w\sim^2 C\_2\sim - 1)^2 L\_1\sim^4 + 2\,V\_2\sim^2 C\_1\sim^3 w\sim^6 (L\_2\sim w\sim^2 C\_2\sim - 1)(M\sim^2 w\sim^4 C\_1\sim C\_2\sim + 2\,L\_2\sim w\sim^2 C\_2\sim - 2)\,L\_1\sim^3 - w\sim^4 C\_1\sim^2 \left(C\_1\sim^2 C\_2\sim^2 M\sim^4 w\sim^8 V\_2\sim^2 + 6\left(-\frac{w\sim^4 C\_1\sim C\_2\sim^2 L\_2\sim^2 V\_1\sim^2}{6} + w\sim^2 C\_2\sim \left(C\_2\sim V\_2\sim^2 + \frac{C\_1\sim V\_1\sim^2}{3}\right) L\_2\sim - C\_2\sim V\_2\sim^2 - \frac{C\_1\sim V\_1\sim^2 (C\_2\sim^2 R\_2\sim^2 w\sim^2 + 1)}{6}\right) w\sim^4 C\_1\sim M\sim^2 + 2\,V\_2\sim^2 (L\_2\sim w\sim^2 C\_2\sim - 1)^2 (C\_1\sim^2 R\_1\sim^2 w\sim^2 + 3)\right) L\_1\sim^2 \qquad \textbf{(5)}$$

$$+2\,(w\sim^{8}\,C\_1\sim^{2}\,C\_2\sim\,(-w\sim^{2}\,C\_1\sim\,C\_2\sim\,L\_2\sim\,V\_1\sim^{2}+C\_1\sim\,V\_1\sim^{2}+C\_2\sim\,V\_2\sim^{2})\,M\sim^{4}+(-w\sim^{4}\,C\_1\sim\,C\_2\sim^{2}\,L\_2\sim^{2}\,V\_1\sim^{2}$$

$$+(C\_2\sim\,(C\_1\sim^{2}\,R\_1\sim^{2}\,w\sim^{2}+3)\,V\_2\sim^{2}+2\,C\_1\sim\,V\_1\sim^{2})\,C\_2\sim\,w\sim^{2}\,L\_2\sim+(-C\_1\sim^{2}\,R\_1\sim^{2}\,w\sim^{2}-3)\,C\_2\sim\,V\_2\sim^{2}$$

$$-C\_1\sim\,V\_1\sim^{2}\,(C\_2\sim^{2}\,R\_2\sim^{2}\,w\sim^{2}+1))\,w\sim^{4}\,C\_1\sim\,M\sim^{2}+2\,V\_2\sim^{2}\,(L\_2\sim\,w\sim^{2}\,C\_2\sim-1)^{2}\,(C\_1\sim^{2}\,R\_1\sim^{2}\,w\sim^{2}+1))\,w\sim^{2}\,C\_1\sim\,L\_1\sim$$

$$+C\_1\sim^{4}\,C\_2\sim^{2}\,M\sim^{6}\,V\_1\sim^{2}\,w\sim^{12}-C\_2\sim\,w\sim^{8}\,C\_1\sim^{2}\,(-2\,w\sim^{2}\,C\_1\sim\,C\_2\sim\,L\_2\sim\,V\_1\sim^{2}+C\_2\sim\,V\_2\sim^{2}$$

$$-2\,C\_1\sim\,V\_1\sim^{2}\,(R\_1\sim\,R\_2\sim\,w\sim^{2}\,C\_1\sim\,C\_2\sim-1))\,M\sim^{4}-2\left(-\frac{w\sim^{4}\,C\_1\sim\,C\_2\sim^{2}\,L\_2\sim^{2}\,V\_1\sim^{2}}{2}+w\sim^{2}\,C\_2\sim\,(C\_1\sim\,V\_1\sim^{2}\right.$$

$$\left.+C\_2\sim\,V\_2\sim^{2})\,L\_2\sim-C\_2\sim\,V\_2\sim^{2}-\frac{C\_1\sim\,V\_1\sim^{2}\,(C\_2\sim^{2}\,R\_2\sim^{2}\,w\sim^{2}+1)}{2}\right)w\sim^{4}\,(C\_1\sim^{2}\,R\_1\sim^{2}\,w\sim^{2}+1)\,C\_1\sim\,M\sim^{2}$$

$$\left.-V\_2\sim^{2}\,(L\_2\sim\,w\sim^{2}\,C\_2\sim-1)^{2}\,(C\_1\sim^{2}\,R\_1\sim^{2}\,w\sim^{2}+1)^{2}\right)^{1/2}+C\_2\sim\,w\sim\,(C\_1\sim^{2}\,(L\_1\sim^{2}\,R\_2\sim+M\sim^{2}\,R\_1\sim)\,w\sim^{4}$$

$$\left.+C\_1\sim\,R\_2\sim\,(C\_1\sim\,R\_1\sim^{2}-2\,L\_1\sim)\,w\sim^{2}+R\_2\sim)\,V\_2\sim\right)V\_2\sim\Big)\Big/\Big(((-1-C\_1\sim^{2}\,L\_1\sim^{2}\,w\sim^{4}+(-C\_1\sim^{2}\,R\_1\sim^{2}$$

$$+2\,C\_1\sim\,L\_1\sim)\,w\sim^{2})\,V\_2\sim^{2}+C\_1\sim^{2}\,M\sim^{2}\,V\_1\sim^{2}\,w\sim^{4})\,C\_2\sim\,w\sim\Big)$$

Finally, we find the expression in the ideal case of lossless coils.

$R\_eq\_eq\_no\_loss := simplify(subs(R\_1=0, R\_2=0, R\_eq\_eq\_loss));$

$$R\_eq\_eq\_no\_loss := \frac{V\_2\sim\,|-w\sim^{2}\,(w\sim^{2}\,(-L\_1\sim\,L\_2\sim+M\sim^{2})\,C\_2\sim+L\_1\sim)\,C\_1\sim-L\_2\sim\,w\sim^{2}\,C\_2\sim+1|}{\sqrt{-(L\_1\sim\,w\sim^{2}\,C\_1\sim-1)^{2}\,V\_2\sim^{2}+C\_1\sim^{2}\,M\sim^{2}\,V\_1\sim^{2}\,w\sim^{4}}\,C\_2\sim\,w\sim} \tag{6}$$

The two equivalent resitances for both coils with loss and lossless coils is found. We can now easily obtain an expression for the phase angle of the circuit using normal circuit theory.

The total impedance in the circuit is denoted Z_t. Its phase-angle provides information about the matching of the impedances in the circuit.

$Z\_t\_eq := \frac{V\_1}{i\_1};$

$i\_1\_eq := \frac{Z\_2\cdot V\_1}{Z\_1\cdot Z\_2-M^{2}\cdot s^{2}}:$

$$Z\_t\_eq := \frac{V\_1\sim}{i\_1} \tag{7}$$

$Z\_1\_eq := R\_1+s\cdot L\_1+\frac{1}{s\cdot C\_1}:$

$Z\_2\_eq := R\_2+s\cdot L\_2+\frac{1}{s\cdot C\_2}+R\_eq:P$

$Z\_1\_eq := subs(s=s\_eq, Z\_1\_eq):$

Lossy case

$Z\_2\_eq\_loss := subs(s=s\_eq, R\_eq=R\_eq\_eq\_loss, Z\_2\_eq):$

$i\_1\_eq\_loss := simplify(subs(Z\_1=Z\_1\_eq, Z\_2=Z\_2\_eq\_loss, s=s\_eq, i\_1\_eq)):$

$Z\_t\_eq\_loss := simplify(subs(i\_1=i\_1\_eq\_loss, s=s\_eq, Z\_t\_eq));$

$$Z\_t\_eq\_loss := \left((1L\_1\sim\,w\sim^{2}\,C\_1\sim+R\_1\sim\,w\sim\,C\_1\sim\right. \tag{8}$$

$$\left.-I\right)$$

$$V\_2\sim\left(-V\_2\sim^{2}\,w\sim^{8}\,C\_1\sim^{4}\,(L\_2\sim\,w\sim^{2}\,C\_2\sim-1)^{2}\,L\_1\sim^{4}+2\,V\_2\sim^{2}\,C\_1\sim^{3}\,w\sim^{6}\,(L\_2\sim\,w\sim^{2}\,C\_2\sim-1)\,(M\sim^{2}\,w\sim^{4}\,C\_1\sim\,C\_2\sim+2\,L\_2\sim\,w\sim^{2}\,C\_2\sim-2)\,L\_1\sim^{3}\right.$$

$$-w\sim^{4}\,C\_1\sim^{2}\left(C\_1\sim^{2}\,C\_2\sim^{2}\,M\sim^{4}\,w\sim^{8}\,V\_2\sim^{2}+6\left(-\frac{w\sim^{4}\,C\_1\sim\,C\_2\sim^{2}\,L\_2\sim^{2}\,V\_1\sim^{2}}{6}+w\sim^{2}\,C\_2\sim\left(C\_2\sim\,V\_2\sim^{2}+\frac{C\_1\sim\,V\_1\sim^{2}}{3}\right)L\_2\sim\right.\right.$$

$$\left.\left.-C\_2\sim\,V\_2\sim^{2}-\frac{C\_1\sim\,V\_1\sim^{2}\,(C\_2\sim^{2}\,R\_2\sim^{2}\,w\sim^{2}+1)}{6}\right)w\sim^{4}\,C\_1\sim\,M\sim^{2}+2\,V\_2\sim^{2}\,(L\_2\sim\,w\sim^{2}\,C\_2\sim-1)^{2}\,(C\_1\sim^{2}\,R\_1\sim^{2}\,w\sim^{2}+3)\right)$$

$$L\_1\sim^{2}+2\,(w\sim^{8}\,C\_1\sim^{2}\,C\_2\sim\,(-w\sim^{2}\,C\_1\sim\,C\_2\sim\,L\_2\sim\,V\_1\sim^{2}+C\_1\sim\,V\_1\sim^{2}+C\_2\sim\,V\_2\sim^{2})\,M\sim^{4}+(-w\sim^{4}\,C\_1\sim\,C\_2\sim^{2}\,L\_2\sim^{2}\,V\_1\sim^{2}$$

$$+(C\_2\sim\,(C\_1\sim^{2}\,R\_1\sim^{2}\,w\sim^{2}+3)\,V\_2\sim^{2}+2\,C\_1\sim\,V\_1\sim^{2})\,C\_2\sim\,w\sim^{2}\,L\_2\sim+(-C\_1\sim^{2}\,R\_1\sim^{2}\,w\sim^{2}-3)\,C\_2\sim\,V\_2\sim^{2}$$

$$-C\_1\sim\,V\_1\sim^{2}\,(C\_2\sim^{2}\,R\_2\sim^{2}\,w\sim^{2}+1))\,w\sim^{4}\,C\_1\sim\,M\sim^{2}+2\,V\_2\sim^{2}\,(L\_2\sim\,w\sim^{2}\,C\_2\sim-1)^{2}\,(C\_1\sim^{2}\,R\_1\sim^{2}\,w\sim^{2}+1))\,w\sim^{2}\,C\_1\sim\,L\_1\sim$$

$$+C\_1\sim^4\,C\_2\sim^2\,M\sim^6\,V\_1\sim^2\,w\sim^{12}-C\_2\sim\,w\sim^8\,C\_1\sim^2\,(-2\,w\sim^2\,C\_1\sim\,C\_2\sim\,L\_2\sim\,V\_1\sim^2+C\_2\sim\,V\_2\sim^2$$

$$-2\,C\_1\sim\,V\_1\sim^2\,(R\_1\sim\,R\_2\sim\,w\sim^2\,C\_1\sim\,C\_2\sim-1))\,M\sim^4-2\left(-\frac{w\sim^4\,C\_1\sim\,C\_2\sim^2\,L\_2\sim^2\,V\_1\sim^2}{2}+w\sim^2\,C\_2\sim\,(C\_1\sim\,V\_1\sim^2\right.$$

$$\left.+C\_2\sim\,V\_2\sim^2)\,L\_2\sim-C\_2\sim\,V\_2\sim^2-\frac{C\_1\sim\,V\_1\sim^2\,(C\_2\sim^2\,R\_2\sim^2\,w\sim^2+1)}{2}\right)w\sim^4\,(C\_1\sim^2\,R\_1\sim^2\,w\sim^2+1)\,C\_1\sim\,M\sim^2$$

$$\left.-V\_2\sim^2\,(L\_2\sim\,w\sim^2\,C\_2\sim-1)^2\,(C\_1\sim^2\,R\_1\sim^2\,w\sim^2+1)^2\right)^{1/2}+C\_1\sim^3\,C\_2\sim\,(-L\_1\sim\,V\_2\sim+M\sim\,V\_1\sim)\,(L\_1\sim\,V\_2\sim+M\sim\,V\_1\sim)\,($$

$$-L\_1\sim\,L\_2\sim+M\sim^2)\,w\sim^8+\mathrm{I}\,(L\_1\sim\,R\_1\sim\,(-L\_1\sim\,L\_2\sim+M\sim^2)\,V\_2\sim^2+M\sim^2\,V\_1\sim^2\,(L\_1\sim\,R\_2\sim+L\_2\sim\,R\_1\sim))\,C\_2\sim\,C\_1\sim^3\,w\sim^7$$

$$+2\,C\_1\sim^2\left(\left(\frac{L\_1\sim\,(C\_2\sim\,L\_2\sim\,R\_1\sim^2-L\_1\sim^2)\,V\_2\sim^2}{2}+\frac{M\sim^2\,V\_1\sim^2\,(C\_2\sim\,R\_1\sim\,R\_2\sim+L\_1\sim)}{2}\right)C\_1\sim+\left(\left(L\_1\sim\,M\sim^2\right.\right.\right.$$

$$\left.\left.\left.-\frac{3}{2}\,L\_1\sim^2\,L\_2\sim\right)\,V\_2\sim^2+\frac{M\sim^2\,L\_2\sim\,V\_1\sim^2}{2}\right)\,C\_2\sim\right)w\sim^6-\mathrm{I}\,C\_1\sim^2\,(R\_1\sim\,((C\_2\sim\,L\_2\sim\,R\_1\sim^2-L\_1\sim^2)\,V\_2\sim^2$$

$$+M\sim^2\,V\_1\sim^2)\,C\_1\sim+C\_2\sim\,(R\_1\sim\,(-2\,L\_1\sim\,L\_2\sim+M\sim^2)\,V\_2\sim^2+M\sim^2\,R\_2\sim\,V\_1\sim^2))\,w\sim^5-C\_1\sim\,(V\_2\sim^2\,L\_1\sim\,R\_1\sim^2\,C\_1\sim^2$$

$$+((C\_2\sim\,L\_2\sim\,R\_1\sim^2-3\,L\_1\sim^2)\,V\_2\sim^2+M\sim^2\,V\_1\sim^2)\,C\_1\sim+V\_2\sim^2\,C\_2\sim\,(-3\,L\_1\sim\,L\_2\sim+M\sim^2))\,w\sim^4+\mathrm{I}\,R\_1\sim\,(C\_1\sim^2\,R\_1\sim^2$$

$$-2\,C\_1\sim\,L\_1\sim-C\_2\sim\,L\_2\sim)\,C\_1\sim\,V\_2\sim^2\,w\sim^3+V\_2\sim^2\,(C\_1\sim^2\,R\_1\sim^2-3\,C\_1\sim\,L\_1\sim-C\_2\sim\,L\_2\sim)\,w\sim^2+\mathrm{I}\,C\_1\sim\,R\_1\sim\,V\_2\sim^2\,w\sim$$

$$\left.+V\_2\sim^2)\right/$$

$$\left(w\sim\left(\left(-V\_2\sim^2\,w\sim^8\,C\_1\sim^4\,(L\_2\sim\,w\sim^2\,C\_2\sim-1)^2\,L\_1\sim^4+2\,V\_2\sim^2\,C\_1\sim^3\,w\sim^6\,(L\_2\sim\,w\sim^2\,C\_2\sim\right.\right.\right.$$

$$\left.\left.-1)\,(M\sim^2\,w\sim^4\,C\_1\sim\,C\_2\sim+2\,L\_2\sim\,w\sim^2\,C\_2\sim-2)\,L\_1\sim^3-w\sim^4\,C\_1\sim^2\left(C\_1\sim^2\,C\_2\sim^2\,M\sim^4\,w\sim^8\,V\_2\sim^2+6\left(\right.\right.\right.\right.$$

$$\left.\left.\left.\left.-\frac{w\sim^4\,C\_1\sim\,C\_2\sim^2\,L\_2\sim^2\,V\_1\sim^2}{6}+w\sim^2\,C\_2\sim\left(C\_2\sim\,V\_2\sim^2+\frac{C\_1\sim\,V\_1\sim^2}{3}\right)L\_2\sim-C\_2\sim\,V\_2\sim^2\right.\right.\right.\right.$$

$$\left.\left.\left.\left.-\frac{C\_1\sim\,V\_1\sim^2\,(C\_2\sim^2\,R\_2\sim^2\,w\sim^2+1)}{6}\right)w\sim^4\,C\_1\sim\,M\sim^2+2\,V\_2\sim^2\,(L\_2\sim\,w\sim^2\,C\_2\sim-1)^2\,(C\_1\sim^2\,R\_1\sim^2\,w\sim^2+3)\right)L\_1\sim^2\right.$$

$$+2\,(w\sim^8\,C\_1\sim^2\,C\_2\sim\,(-w\sim^2\,C\_1\sim\,C\_2\sim\,L\_2\sim\,V\_1\sim^2+C\_1\sim\,V\_1\sim^2+C\_2\sim\,V\_2\sim^2)\,M\sim^4+(-w\sim^4\,C\_1\sim\,C\_2\sim^2\,L\_2\sim^2\,V\_1\sim^2$$

$$+(C\_2\sim\,(C\_1\sim^2\,R\_1\sim^2\,w\sim^2+3)\,V\_2\sim^2+2\,C\_1\sim\,V\_1\sim^2)\,C\_2\sim\,w\sim^2\,L\_2\sim+(-C\_1\sim^2\,R\_1\sim^2\,w\sim^2-3)\,C\_2\sim\,V\_2\sim^2$$

$$\left.-C\_1\sim\,V\_1\sim^2\,(C\_2\sim^2\,R\_2\sim^2\,w\sim^2+1))\,w\sim^4\,C\_1\sim\,M\sim^2+2\,V\_2\sim^2\,(L\_2\sim\,w\sim^2\,C\_2\sim-1)^2\,(C\_1\sim^2\,R\_1\sim^2\,w\sim^2+1))\,w\sim^2\,C\_1\sim\,L\_1\sim\right.$$

$$+C\_1\sim^4\,C\_2\sim^2\,M\sim^6\,V\_1\sim^2\,w\sim^{12}-C\_2\sim\,w\sim^8\,C\_1\sim^2\,(-2\,w\sim^2\,C\_1\sim\,C\_2\sim\,L\_2\sim\,V\_1\sim^2+C\_2\sim\,V\_2\sim^2$$

$$-2\,C\_1\sim\,V\_1\sim^2\,(R\_1\sim\,R\_2\sim\,w\sim^2\,C\_1\sim\,C\_2\sim-1))\,M\sim^4-2\left(-\frac{w\sim^4\,C\_1\sim\,C\_2\sim^2\,L\_2\sim^2\,V\_1\sim^2}{2}+w\sim^2\,C\_2\sim\,(C\_1\sim\,V\_1\sim^2\right.$$

$$\left.+C\_2\sim\,V\_2\sim^2)\,L\_2\sim-C\_2\sim\,V\_2\sim^2-\frac{C\_1\sim\,V\_1\sim^2\,(C\_2\sim^2\,R\_2\sim^2\,w\sim^2+1)}{2}\right)w\sim^4\,(C\_1\sim^2\,R\_1\sim^2\,w\sim^2+1)\,C\_1\sim\,M\sim^2$$

$$\left.-V\_2\sim^2\,(L\_2\sim\,w\sim^2\,C\_2\sim-1)^2\,(C\_1\sim^2\,R\_1\sim^2\,w\sim^2+1)^2\right)^{1/2}\,V\_2\sim+(\mathrm{I}\,C\_2\sim\,L\_2\sim\,M\sim^2\,V\_1\sim^2$$

$$-\mathrm{I}\,C\_2\sim\,L\_1\sim^2\,L\_2\sim\,V\_2\sim^2)\,C\_1\sim^2\,w\sim^6+M\sim^2\,C\_1\sim^2\,C\_2\sim\,(R\_1\sim\,V\_2\sim^2+R\_2\sim\,V\_1\sim^2)\,w\sim^5-\mathrm{I}\,(((C\_2\sim\,L\_2\sim\,R\_1\sim^2$$

$$-L\_1\sim^2)\,V\_2\sim^2+M\sim^2\,V\_1\sim^2)\,C\_1\sim-2\,V\_2\sim^2\,C\_2\sim\,L\_1\sim\,L\_2\sim)\,C\_1\sim\,w\sim^4+\mathrm{I}\,(C\_1\sim^2\,R\_1\sim^2-2\,C\_1\sim\,L\_1\sim$$

$$\left.-C\_2\sim\,L\_2\sim)\,V\_2\sim^2\,w\sim^2+\mathrm{I}\,V\_2\sim^2)\,C\_1\sim\right)$$

Lossless case

```
Z_2_eq_lossless := subs(R_1 = 0, R_2 = 0, s = s_eq, R_eq = R_eq_eq_no_loss, Z_2_eq) :
Z_1_eq_lossless := subs(R_1 = 0, R_2 = 0, s = s_eq, Z_1_eq) :
i_1_eq_lossless := simplify(subs(Z_1 = Z_1_eq_lossless, Z_2 = Z_2_eq_lossless, s = s_eq, i_1_eq)) :
Z_t_eq_lossless := simplify(subs(i_1 = i_1_eq_lossless, s = s_eq, Z_t_eq));
```

$$Z\_t\_eq\_lossless := \left(\mathrm{I}\,(L\_1\sim\,w\sim^2\,C\_1\sim-1)\,V\_2\sim\,|-w\sim^2\,(w\sim^2\,(-L\_1\sim\,L\_2\sim+M\sim^2)\,C\_2\sim+L\_1\sim)\,C\_1\sim-L\_2\sim\,w\sim^2\,C\_2\sim+1|+(-1\right. \tag{9}$$

$$+C\_2\sim\,C\_1\sim\,(-L\_1\sim\,L\_2\sim+M\sim^2)\,w\sim^4+(C\_1\sim\,L\_1\sim+C\_2\sim\,L\_2\sim)\,w\sim^2)$$

$$\left.\sqrt{-(L\_1\sim\,w\sim^2\,C\_1\sim-1)^2\,V\_2\sim^2+C\_1\sim^2\,M\sim^2\,V\_1\sim^2\,w\sim^4}\right)\Big/\left(w\sim\left(V\_2\sim\,|-w\sim^2\,(w\sim^2\,(-L\_1\sim\,L\_2\sim+M\sim^2)\,C\_2\sim+L\_1\sim)\,C\_1\sim\right.\right.$$

$$\left.\left.-L\_2\sim\,w\sim^2\,C\_2\sim+1|+\mathrm{I}\,(L\_2\sim\,w\sim^2\,C\_2\sim-1)\,\sqrt{-(L\_1\sim\,w\sim^2\,C\_1\sim-1)^2\,V\_2\sim^2+C\_1\sim^2\,M\sim^2\,V\_1\sim^2\,w\sim^4}\right)C\_1\sim\right)$$

A.2 Simplifying the equivalent CVL resistance

We want to simplify the expression for R_eq_no_loss in terms of an unbalancing factor x_u to better understand response. Section 4.6 - Introducing the unbalancing factor - xu

$$w0\_eq := \frac{1}{\mathrm{sqrt}(L\_1 \cdot C\_1)} :$$

$$w0\_eq\_2 := \frac{1}{\mathrm{sqrt}(L\_2 \cdot C\_2)} :$$

$$M\_eq := k \cdot \mathrm{sqrt}(L\_1 \cdot L\_2) :$$

$$k\_eq := solve(M\_eq = M, k) :$$

$$R\_eq\_no\_loss\_simplify := simplify(subs(k = k\_eq, M = M\_eq, R\_eq\_eq\_no\_loss)) :$$

$$L\_1\_eq := solve(w0 = w0\_eq, L\_1) :$$

$$L\_2\_eq := solve(w0 = w0\_eq\_2, L\_2) :$$

$$C\_1\_eq := solve(w0 = w0\_eq, C\_1) :$$

$$C\_2\_eq := solve(w0 = w0\_eq\_2, C\_2) :$$

$$R\_eq\_no\_loss\_simplify := simplify(subs(L\_1 = L\_1\_eq, L\_2 = L\_2\_eq, C\_1 = C\_1\_eq, C\_2 = C\_2\_eq, R\_eq\_no\_loss\_simplify));$$

$$R\_eq\_no\_loss\_simplify := \frac{\sqrt{L\_1\sim}\, V\_2\sim \left|(k^2-1)\, w\sim^4 + 2\, w\sim^2\, w0\sim^2 - w0\sim^4\right| L\_2\sim}{\sqrt{-V\_2\sim^2\, (w\sim - w0\sim)^2\, (w\sim + w0\sim)^2\, L\_1\sim + L\_2\sim\, V\_1\sim^2\, k^2\, w\sim^4}\; w\sim} \tag{1}$$

Appendix B

Simulink diagrams

B.1 Constant resistance load

B.1.1 Uncontrolled

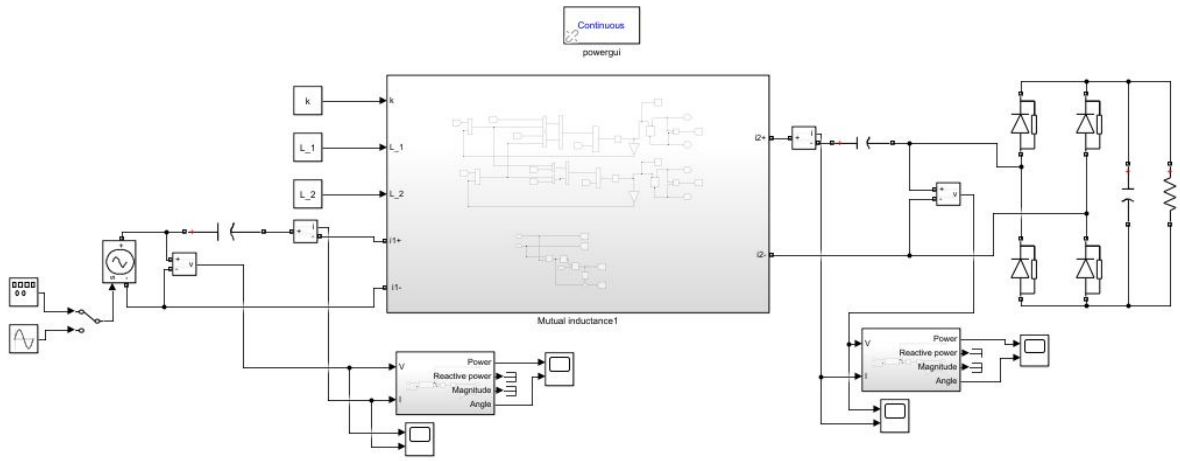

B.1.2 Controlled

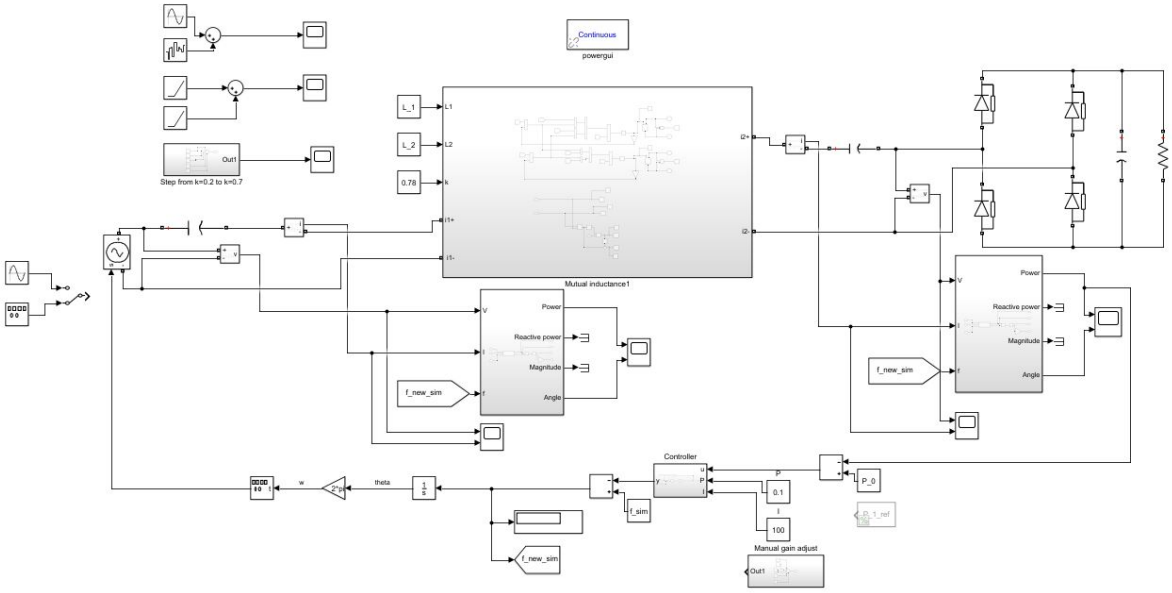

B.2 Constant voltage load

B.2.1 Uncontrolled

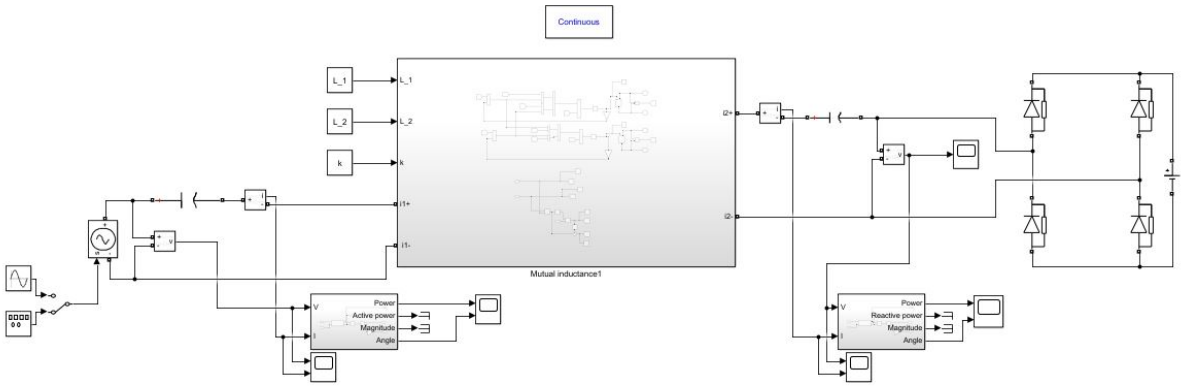

B.2.2 Controlled

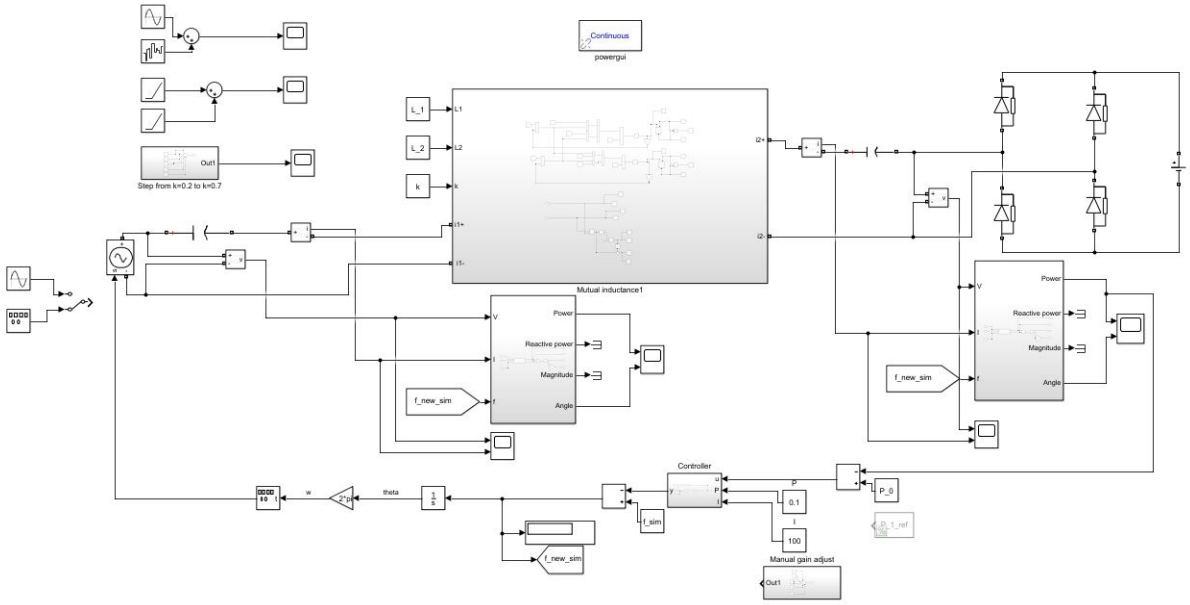

Appendix C

Matlab init script

```
%% Optimal parameters
P_0=10e3;
P_1_ref = 10.34e3;
V_0=300;
f_0=20e3;
w0=f_0*2*pi;
k_0 = 0.2;
%% System
k=0.2;
L_1=310e-6;
L_2=310e-6;
C_1=1/(w0^2*L_1);
C_2=1/(w0^2*L_2);
M=k*sqrt(L_1*L_2);
%% Loss
Q=300;
R_1=(w0*L_1/Q);
R_2=(w0*L_2/Q);
%% Lossless
% R_1=0;
% R_2=0;
%% Voltages
V_2_dc = 300;
V_2 = (4/pi)*V_2_dc;  %Since these are source-values they need to be
    peak-values and not RMS.
V_1=(4/pi)*V_2_dc;
%% Simulation parameters
f_sim= f_0;
w_sim=f_sim*2*pi;
w=w_sim;
%% Balancing
x_u=0.95;
x_c=1.03;
V_1=sqrt(V_2/x_u)^2;
C_1= x_c*C_2*(L_2/L_1);
%% Limits of operation for the CVL
f_u=sqrt(V_2/(C_1*L_1*V_2-C_1*M*V_1))/(2*pi);
f_l=sqrt(V_2/(C_1*L_1*V_2+C_1*M*V_1))/(2*pi);
```